Modeling Jet-plate Interactions Using Large Eddy Simulations

by

Nikhil Tamhhane

A Thesis Presented in Partial Fulfillment
of the Requirements for the Degree
Master of Science

Approved April 2022 by the
Graduate Supervisory Committee:

Jeonglae Kim, Co-Chair
Yulia Peet, Co-Chair
Jinah Jeun

ARIZONA STATE UNIVERSITY

May 2022

ABSTRACT

Modern aircraft propulsion systems such as the ultra high bypass ratio turbofan impose constraints on engine installation below the wing, causing jet–wing interactions. Similar interactions are encountered when a jet-powered aircraft takes off on airport runway or aircraft carrier deck. High-speed jet flow near a solid surface shows markedly different turbulence characteristics compared with free jet, including attached turbulent jet and development of non-equilibrium boundary layer downstream. Wall pressure fluctuations tend to be more unsteady and stronger, leading to increased vibration affecting aircraft cabin noise and modified jet noise radiation. Large-eddy simulation (LES) is useful to characterize turbulent jet flows over a solid surface as well as wall pressure distribution to promote physical understanding and modeling studies. In this study, LES is performed for an installed setup of a Mach 0.7 turbulent jet where the jet–plate distance is fixed at 2D where D is the nozzle-exit diameter. Unstructured-grid LES is used to validate the corresponding experiment (from literature). In addition, a high-fidelity numerical database is built for further analysis and modeling. Turbulence statistics and energy spectra show that agreement with the experimental measurement for the installed case is encouraging, paving a way for future analysis and modeling.

ACKNOWLEDGEMENTS

I would like to express my sincere gratitude to my advisor, Dr. Jeonglae Kim, for giving me the opportunity to work on this research. This would not have been possible without his constant support and guidance. It has been a privilege to work with him, study under his mentorship and learn from his expertise. I would like to express my sincere gratitude to Sijie Huang for his help in setting up the simulations and also for the timeless support that he provided throughout this research. Finally, I would like to thank my committee members, Dr. Yulia Peet and Dr. Jin Ah Jeun, for taking time off from their busy schedules and accepting to join my advisory committee.

TABLE OF CONTENTS

CHAPTER Page

LIST OF TABLES

LIST OF FIGURES

Figure Page

Figure Page

Figure Page

Figure Page

Figure Page

Chapter 1

INTRODUCTION

Jet noise reduction is one of the critical challenges faced by the aviation industry in modern times. The pros provided by the industry in the form of boosting global economy and international peace are being outweighed by the potential cons, in the form of adverse health impact on adults and children. This can be in the form of hypertension in adults (Lyrintzis and Coderoni (2020a)), disturbance in sleep (Muzet (2007)), negative cognitive effects in children (Cohen *et al.* (1980)) and permanent hearing damage (Chen and Chen (1993)). The effects of jet noise are more severely felt by crew members working on board aircraft carriers, who are constantly exposed to high speed jet noise because of take-off, landing and operation of fighter jets on board. This has had a knock on effect of more stringent regulations being imposed by regulatory bodies around the world and a subsequent increase in development costs because of these regulations (to curb jet noise). Thus, finding economical ways of reducing jet noise, while keeping design and manufacturing costs low has become of paramount importance.

1.1 Motivation

High performance military aircraft naturally produce more noise than commercial aircraft, because of the high thrust, low bypass ratio design of engine. This noise reaches hazardous levels during take-off, landing or high thrust applications. When a jet takes off from an aircraft carrier, the interaction of the exhaust flow with the ambient air and the runway below it produces noise exceeding 150 dB (Wall *et al.* (2022)), making it unsafe for crew members to work on board, even with proper Per-

sonal Protective Equipment. Hearing loss and tinitus are one of the leading causes of military disability claims, affecting more than 2.6 million former service members (Doychak (2010)) and the United States Department of Veterans Affairs spends more than a billion dollars per year on hearing loss cases alone (Doychak (2010)). Figure 1.1 shows the year on year trend of net expenditure by the US department of Veteran Affairs in a period between 1968 and 2005 (Doychak (2010)). We can see that the navy spent $\sim$ 7 billion dollars on veterans disability benefits paid for hearing loss as primary disability, which is more than 5 times that spent by the marines.

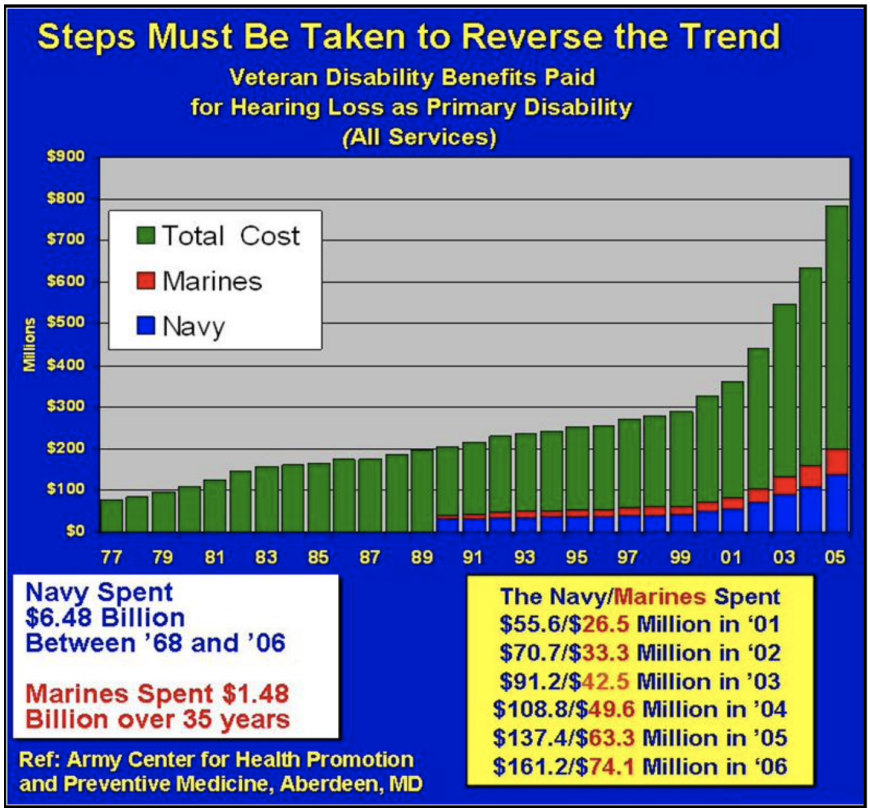

Figure 1.1: Year on Year Cost Incurred by Military and Navy to the US Department of Veteran Affairs (Doychak (2010))

Such high amplitude noise environments have motivated the development of active noise reduction technologies, but human tissue conduction limits the effective attenuation to 40-50 dB. These devices primarily consist of ear muffs and/or earplugs

mounted in a padded helmet. However, these devices are rarely in operational use because of the constraints they place on communication with other staff, hence attenuation typically plateaus at 30 dB (Wall *et al.* (2022)). Thus, there has been an increased focus on finding active/passive Jet Noise Reduction (JNR) technologies among academia and the industry, to make it safer for crew members working on board and also to reduce jet noise as fighter jets fly over civilian areas. The focus of JNR programs has been on finding nozzle designs that disrupt the most energetic flow noise sources while making little, to no impact on thrust performance of the engine.

The main idea behind jet noise reduction is to study the complex interaction phenomenon that occurs when a high speed, high temperature exhaust jet interacts with a tangential surface placed at a certain radial distance below it. The interaction of the jet with a flat surface significantly modifies the flow field of the jet, as opposed to when the jet is allowed expand unhindered in the atmosphere. A combination of the Coanda effect, turbulent mixing with ambient air and development of non-equilibrium boundary layer along the surface modifies the jet flow significantly, and this subsequently has an effect on the noise generation and propagation mechanisms. In addition to the modified jet flow field, this complex interaction induces pressure on surface of the runway, which causes vibrations in the aircraft carrier deck panels, and may lead to an increased stress loading. Thus it is clear from the above discussion that jet noise reduction has to be better understood and properly incorporated in the design of high performance military aircraft, not only to improve the long term health of crew members working on an aircraft carrier, but also to improve the design of the aircraft carrier deck (it is severely affected by the induced vibrations), which can have further benefits itself.

Primarily, there are two approaches to JNR adapted by the research community and industry, namely experimental and computational. Experimental studies are

mostly carried out on scaled down models of the actual engine in controlled laboratory conditions, as performing full scale experiments during development stage can be prohibitively expensive. As experiments provide actual data of the jet flow field, the noise production and radiation sources can be accurately identified and noise mitigation strategies can be effectively developed. However, with the rise of large scale parallel computing and high fidelity computational fluid dynamics simulations (in the form of Large Eddy Simulations, Direct Numerical Simulations), it is possible to develop a computational model of the experimental set up and generate results as accurate as the experiments.

Several studies are available in literature that investigate the effects of a tangential plate on the flow field of a jet using experimental analysis. Mancinelli and Cammussi (Mancinelli and Camussi (2018)), Di Marco *et al.* (Di Marco *et al.* (2015)) investigate the effect of varying the jet-plate distance and jet flow speed on the wall pressure characteristics and development of the Turbulent Boundary Layer. The effect of the jet-plate distance on the mean velocity, turbulence intensity is also investigated, and a spectral analysis of the velocity and wall pressure signals is performed to characterise the noise generating mechanisms in the jet. Meloni *et al.* (Meloni *et al.* (2019)) studied the effect of varying the jet flow velocity, while keeping the jet-plate distance fixed on the wall pressure characteristics, and a spectral analysis of the statistics was also performed in the Fourier space to investigate the noise sources. Through these studies, the authors found that Fourier transforms (in the form of Fast Fourier Transform) cannot isolate the sources of sound in the jet flow.

Jet noise is primary composed of two components - hydrodynamic and acoustic. The hydrodynamic component is caused by large scale flow structures and the acoustic component is caused by the sound waves generated in the flow that propagate at the speed of sound. Furthermore, the hydrodynamic components have a low fre-

quency, move at the order of the flow speed and are intermittent in nature. The acoustic components, on the other hand have a high frequency, are 'continuous' in nature and propagate at the order of the speed of sound (Guitton *et al.* (2007); Kerhervé *et al.* (2008); TINNEY and JORDAN (2008)). In a similar study performed by the same authors (Grizzi and Camussi (2012)), they further state that because of the intermittent, low frequency nature of the hydrodynamic components, they can be potentially lost by the low pass/high pass filtering procedure applied by Fourier transform functions, and hence these cannot be used a comprehensive tool to identify noise sources in the jet flow. Instead, a wavelet decomposition based filtering method is employed to identify and isolate these intermittent events (of hydrodynamic noise component). A continuous wavelet transform is applied to the wall pressure signals and a filtering procedure is employed based on Farge (1992), RUPPERT-FELSOT *et al.* (2009), and further developed by the authors, wherein the hydrodynamic component and acoustic components have different values of wavelet coefficients. They can then be separated by a filtering procedure that separate these components based on a threshold (determined iteratively), and the respective components can then be reconstructed based on classical Fourier transform techniques (Grizzi and Camussi (2012)).

Thus, from these studies, it can be inferred that the wavelet based decomposition technique is much more comprehensive in extracting and identifying the sources of sound in the jet flow field, and it should be used in analyzing the flow data in experimental, or simulation studies.

These are some of the experimental approaches used for studying the flow field of a turbulent jet. Since these studies have been carried out for more than 60 years, a large amount of data is available for perusal and covering these studies is beyond the scope of the current work. However, the common denominator in all experimental

work, which works as a potential drawback is the limitation of spatially resolved data in the flow field of the jet. Since in an experiment, the flow field has to sampled physically using probes, it is not possible to sample data at each and every point in the domain to monitor the complete time resolved flow components. It will require multiple probes, and multiple sampling iterations, which makes the process counter-intuitive, time consuming and potentially expensive. This is where CFD simulations can be advantageous - once the results are established with sufficient confidence, the simulations can provide spatially resolved data, and we can get the flow statistics at any spatial point in the flow domain. However, to obtain results with sufficient accuracy, a high fidelity simulation must be run with a time step small enough to avoid numerical instabilities and prevent excessive dispersion and diffusion errors. This leads to a large simulation time, ranging from a couple of days to months at a time, in the case of Direct Numerical Simulations. Thus, considering the pros and cons of simulations, they can be used to complement experimental studies and aide in improving the design process of Jet Noise Reduction.

However, the development of Large Eddy Simulation technology has boosted research activity significantly, as it allows accurate modelling of high speed compressible flows which are far more computationally cheaper than Direct Numerical Simulations (DNS). Also, with the increase of available computational power, CFD simulations are becoming cheaper and far more common, thus allowing for more accurate LES simulations with faster turn-around times. In the past 25 years, the increase in computer power has been exponential - the world's most powerful supercomputer in 2019 was the Summit-IBM Power System AC922 with 2.4 million cores and a LINPACK benchmark speed of 148.6 petaflops/s, almost a million times faster than the 3600 core Intel XP/S 140 Paragon supercomputer (LINPACK benchmark speed of 143.40 gigaflops/s) used back in 1994 (Lyrintzis and Coderoni (2020b)). This increase in

computer power, coupled with developments in software technologies that utilize the large scale parallel processing capability of these supercomputers has made complex turbulence problems within reach of CFD simulations.

Thus, the above discussion served as a motivation to explore one such Jet Noise Reduction problem using CFD simulations - to find a suitable simulation strategy that can be validated using experimental data obtained from literature, and use the simulation data to complement the experiment results in finding ways to tackle the problem of Jet Noise Reduction.

1.2 Objectives

The main goal of this research is to study the compressible flow through a converging nozzle using Large Eddy simulations and validate the simulation data with corresponding experiments performed by Dr. Roberto Cammussi's research group. The simulation is modelled such that it mimics the experimental set up used by Mancinelli and Cammussi (Mancinelli and Camussi (2018)), which is essentially a simplified version of the jet-plate interaction phenomenon that takes place when the exhaust jet from a fighter plane interacts with an aircraft carrier deck during take-off or landing. The simulation is set up in two configurations as given below -

1) Freejet - the nozzle is placed in a computational domain such that the jet is not bounded by any surfaces in its vicinity, it is 'free' to expand in the ambient medium. A diagrammatic representation of the freejet set up is given in figure 1.2

2) Installed jet - a flat plate is placed tangential to the nozzle exit, at a certain radial distance from the nozzle axis. A diagrammatic representation of the installed jet set up is given in figure 1.3.

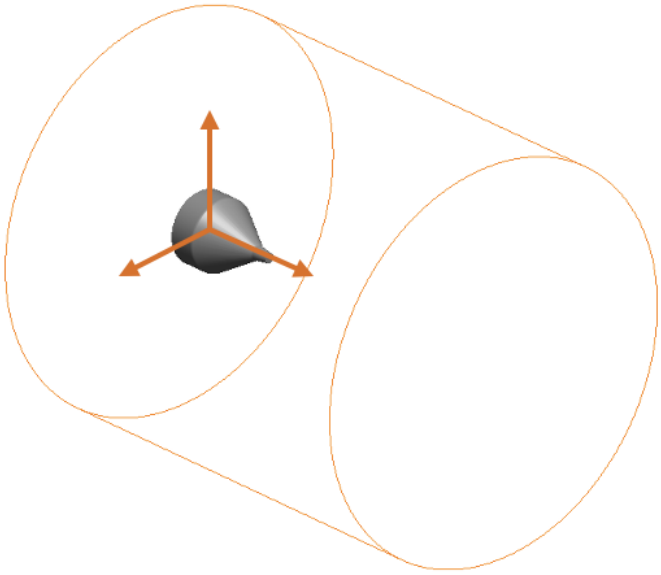

Figure 1.2: Free Jet Simulation Domain

The freejet case is chosen from experiments performed by Mancinelli and Camussi detailed in their paper, "An experimental investigation of the wall pressure field induced by a low and moderate Mach numbers jet on a tangential flat plate" (Mancinelli and Camussi (2018)), and the installed jet case is chosen from experiments performed by Meloni *et al.* detailed in their paper, "Wall-pressure fluctuations induced by a compressible jet flow over a flat plate at different Mach numbers" (Meloni *et al.* (2019)).

Computational grids of the models were created to run extensive LES simulations on the two cases. For each case, a baseline simulation with a coarse grid was run to check the set up of the simulation code, before more grid refined cases were run. The simulation physics were set up to mimic the experimental conditions set up by the authors in Mancinelli and Camussi (2018), and Meloni *et al.* (2019). The simulations were run using the proprietary code CharLESx, developed by Cascade Technologies, on Arizona State University's supercomputer Agave, utilizing the state

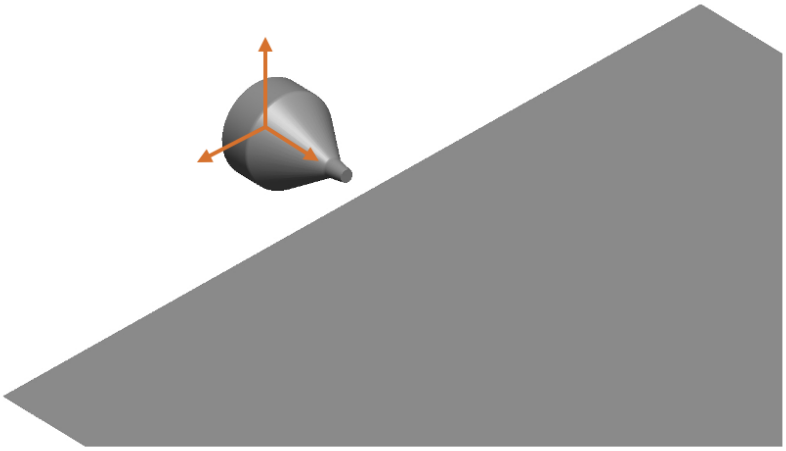

Figure 1.3: Installed Jet Simulation Domain

of the art parallel processing capabilities of CharLESx. A brief overview of the working of CharLESx and the numerical methods employed in this study will be given in Chapter 2.

The flow field of the jet in all cases was analyzed using virtual probes placed in the simulation domain at various locations to analyze the time varying statistics of the flow quantities. For the freejet case, the flow was analyzed for single point statistics (mean velocity, turbulence intensity) to validate the simulation results with the experiment. A spectral analysis using Fourier transforms and cross correlation functions was performed to check whether jet flow predicted by the simulation follows universal jet flow characteristics, and also to validate the spectral features with simulation data. For the installed jet case, the wall pressure data was analyzed to characterize the interaction of the jet with the plate using a statistical and spectral approach, and the results were validated with experiments to check the accuracy of simulations. Also, a wavelet decomposition technique is applied to the wall pressure signals as discussed in (Grizzi and Camussi (2012)) to try and identify the various components of sound in the jet flow, and find ways of isolating these sources.

Chapter 2

MATHEMATICAL FORMULATION

2.1 Background on LES

Large Eddy Simulations (LES) are used for simulating all turbulent jet flows in this work. LES is based on the idea that large scale motions of flow are responsible for majority of the energy transport and are explicitly computed, whereas the smaller, unresolved scales of flow are modelled. LES simulations are computationally less expensive than Direct Numerical Simulations (DNS), as in LES, instead of direct computation of all the scales of the Navier-Stokes equations, these equations are filtered by a low pass filter which filters out the large scale components, which are directly computed, and the small scale components, which are modelled, by subgrid-scale models. Thus, LES is used for simulation of flows where the Reynolds number is too high or the geometry is too complex for the use of DNS.

2.2 Grid Filtering Operation

The Navier Stokes equations are filtered into large scale and small scale components using a low pass spatial filter, defined as follows -

$$\bar{f}(x,t) = \int G(x')f(x-x')dx' \tag{2.1}$$

where G is the filter function, with some characteristic cut-off scale or filter width Δ. This filter operator separates the variable f into -

$$f = \tilde{f} + f' \tag{2.2}$$

where $\tilde{f}$ is the filtered (resolved) component and f' is the small scale (or sub-grid scale or unresolved) component. The filtered field $\bar{f}$ is preserved, and the residual field f' is removed after the application of the filter function. The field that is preserved, i.e., $\bar{f}$ represents the large scale motion, which can be resolved on a coarse mesh and the small scales (f') are modelled using certain empirical models.

However, instead of using an explicitly defined filter function, the computational grid is used as the filter, which filters out all the scales that are smaller than the cell spacing of the grid. This operation is called as grid filtering, and it is more commonly used in LES solvers. According to the Nyquist theorem, for a grid spacing of Δ then no scales smaller than 2Δ can be captured and are filtered out by the coarse computational grid.

2.3 Governing Equations

The filtered, incompressible Navier-Stokes equations are given by -

$$\frac{\partial \tilde{u}_i}{\partial x_i} = 0 \tag{2.3}$$

$$\frac{\partial \tilde{u}_i}{\partial t} + \tilde{u_j}\frac{\partial \tilde{u}_i}{\partial x_j} = -\frac{1}{\rho}\frac{\partial \tilde{p}}{\partial x_i} + \nu\frac{\partial^2 \tilde{u}_i}{\partial x_j \partial x_j} - \frac{\partial \tau_{ij}}{\partial x_j}, \tag{2.4}$$

where the sub-grid stress tensor is given by τ_{ij},

$$\tau_{ij} = \widetilde{u_i u_j} - \tilde{u}_i \tilde{u}_j \tag{2.5}$$

The non-linear term $\widetilde{u_i u_j}$ appearing in the Navier Stokes equations (in the form of τ_{ij}, i.e, the *sub-grid scale stress*) remains unresolved, and forms the well known closure problem in turbulence. It represents the interactions between the resolved large scales and unresolved small scales of motion. More specifically, the term $\frac{\partial \tau_{ij}}{\partial x_j}$ in equation 2.4 represents the momentum transfer between the resolved large scale and the sub-grid scales. This term cannot be represented exactly, and hence in order to close

the Navier Stokes equations, it is represented using models called as sub–grid scale models. The energy equation can be represented in the form of a transport equation for kinetic energy as -

$$\frac{\partial \tilde{k}}{\partial t} + \tilde{u_j}\frac{\partial \tilde{k}}{\partial x_j} = -\frac{\partial}{\partial x_j}\left(\frac{1}{\rho}\widetilde{pu_j} + \tau_{ij}\tilde{u_i} - 2\nu\tilde{u_i}\tilde{S_{ij}}\right) - 2\nu\tilde{S_{ij}}\tilde{S_{ij}} + \tau_{ij}\tilde{S_{ij}}, \tag{2.6}$$

where, $\tilde{k} = \frac{1}{2}\tilde{u_i}\tilde{u_i}$ is the kinetic energy per unit mass and $\tilde{S_{ij}} = \frac{1}{2}\left(\frac{\partial \tilde{u_i}}{\partial x_j} + \frac{\partial \tilde{u_j}}{\partial x_i}\right)$ is the resolved strain rate tensor. The first term on the right hand side of equation 2.6 represents the spatial transport of $\tilde{k}$ by pressure, turbulence and viscous diffusion, however this entire term is non-dissipative. Consequently, the second term represents the dissipation of $\tilde{k}$ by viscosity at the resolved scale and the third term represents the dissipation of $\tilde{k}$ through energy transfer to the sub-grid scale, where it is eventually dissipated as heat (due to viscosity at small scales). At high Reynolds numbers, the second term is exceedingly small whereas the third term dominates, and it is this term that the sub-grid scale models capture.

The dissipation of $\tilde{k}$ to sub-grid scales is captured by ε_{sgs} and is defined as -

$$\varepsilon_{sgs} = \tau_{ij}\tilde{S_{ij}} \tag{2.7}$$

The sub-grid scale dissipation can be instantaneously locally positive or negative, if it is locally positive, then the energy is transferred from sub-grid scale to resolved scale, and if it is negative, then the energy is transferred from the resolved scale to the sub-grid scale.

2.4 Sub-grid Scale Modelling

2.4.1 Dynamic Smagorinsky (Germano) Subgrid Model

In the original Smagorinsky model, the Smagorinsky model coefficient C_S must be explicitly specified, and varies for different types of flow configurations. The Dynamic

Smagorinsky Model, proposed by Germano *et al.* (1991) overcomes this limitation by allowing implicit calculation of C_S so that it does not need to be specified, but can be computed by the LES calculation dynamically. The Germano identity is based on filtering the resolved scale fields again with a second, larger "test" filter, which has a characteristic scale Δ_T (where Δ_T is larger than the original filter characteristic scale Δ) and "test stress" T_{ij}. If the test stress operator is $\widetilde{(.)}^T$, then the test stress T_{ij} can be defined as

$$T_{ij} = \widetilde{\widetilde{u_i u_j}}^T - \tilde{\tilde{u}}_i^T \tilde{\tilde{u}}_j^T$$

Since test filtering of τ_{ij} gives

$$\tilde{\tau_{ij}}^T = \widetilde{\widetilde{u_i u_j}}^T - \widetilde{\tilde{u}_i \tilde{u}_j}^T,$$

the "Germano identity" can be written as

$$\widetilde{\tilde{u}_i \tilde{u}_j}^T - \tilde{\tilde{u}}_i^T \tilde{\tilde{u}}_j^T = L_{ij} = T_{ij} - \tilde{\tau_{ij}}^T \tag{2.8}$$

The quantity L_{ij} can be evaluated from the u_i available in the LES by applying the test filter $\widetilde{(.)}^T$ to u_i and to the resolved scale product $\tilde{u}_i \tilde{u}_j$. Thus, L_{ij} is a known quantity in an LES. If both T_{ij} and τ_{ij} are modelled with a Smagorinsky-type model, then we obtain,

$$T_{ij} = 2(C_S \Delta^T)^2 |\tilde{\tilde{S}}^T| \tilde{\tilde{S}}_{ij}^T \, and \, \tau_{ij} = 2(C_S \Delta)^2 |\tilde{\tilde{S}}| \tilde{\tilde{S}}_{ij} \tag{2.9}$$

Applying the test filter to τ_{ij} gives,

$$\tilde{\tau_{ij}}^T = 2(C_S \Delta)^2 \widetilde{|\tilde{S}| \tilde{S}_{ij}}^T \tag{2.10}$$

Substituting equation 2.10 and 2.9 into equation 2.8, we get,

$$L_{ij} = T_{ij} - \tilde{\tau_{ij}}^T = {C_S}^2 M_{ij}, \tag{2.11}$$

where

$$M_{ij} = 2(\Delta^T)^2 |\tilde{\tilde{S}}^T| \tilde{\tilde{S}}_{ij}^T - 2(\Delta)^2 \widetilde{|\tilde{S}| \tilde{S}_{ij}}^T \tag{2.12}$$

Since both L_{ij} and M_{ij} can be evaluated from the $\tilde{u_i}$ available in the LES data, we can solve for C_S^2 by multiplying both sides of equation 2.11 by M_{ij} and simplifying, which gives,

$$C_S^2 = \frac{L_{ij}M_{ij}}{M_{kl}M_{kl}} \tag{2.13}$$

This approach is called the "Dynamic Smagorinsky (Germano) model" since there is no need to specify *a priori* a form for C_S. Morever, C_S is allowed to vary dynamically rather than allowing it to be a constant, which gives improved results compared to the conventional Smagorinsky model. For compressible flows where $\frac{\partial u_i}{\partial x_i} \neq 0, C_S$ in the Dynamic Smagorinsky Model is obtained from

$$C_S^2 = \frac{L_{kl}M_{kl}}{M_{ij}M_{ij}} - \frac{1}{3}\frac{L_{kk}M_{ll}}{M_{ij}M_{ij}} \tag{2.14}$$

where $L_{kk} \neq 0$ and $M_{ll} \neq 0$ in compressible flows.

2.5 CharLESx

CharLESx is a high fidelity compressible LES code, which solves the filtered compressible Navier Stokes equations using a finite volume based method. In compressible turbulent flows, an additional filtering operation called Favre filtering is employed to avoid the a sub-grid scale term in the continuity equation (Pino Martín *et al.* (2000)). It is defined as

$$\tilde{f} = \frac{\overline{\rho f}}{\bar{\rho}} \tag{2.15}$$

This Favre filter can then be applied to the Navier Stokes equations, and an equation for total Energy is used in addition to the mass and momentum equations. In CharLESx, the following filtered compressible Navier-Stokes equations are solved-

$$\frac{\partial \bar{\rho}}{\partial t} + \frac{\partial \bar{\rho}\tilde{u_i}}{\partial x_i} = 0 \tag{2.16}$$

$$\frac{\partial \bar{\rho}\tilde{u_i}}{\partial t} + \frac{\partial}{\partial x_j}[\bar{\rho}\tilde{u_i}\tilde{u_j} + \bar{p}\delta_{ij}] = \frac{\partial \tilde{\tau_{ij}}}{\partial x_j} \tag{2.17}$$

$$\frac{\partial \bar{\rho}\tilde{E}}{\partial t} + \frac{\partial}{\partial x_j}[(\bar{\rho}\tilde{E} + \bar{p})\tilde{u_j} - \tilde{\tau_{ij}}\tilde{u_i}] = -\frac{\partial \tilde{q_j}}{\partial x_j} \tag{2.18}$$

where $\bar{\rho}$, $\tilde{u_i}$ and $\bar{p}$ denote the filtered density, velocity components and pressure respectively. The filtered total energy $\tilde{E}$ is given by -

$$\tilde{E} = \frac{\bar{p}}{\bar{\rho}(\gamma - 1)} + \frac{1}{2}\tilde{u_k}\tilde{u_k} \tag{2.19}$$

The fluid is assumed to be calorically perfect, with the ratio of specific heats $\gamma = 1.4$. The ideal gas law $\bar{p} = \bar{\rho}R\tilde{T}$ is taken as the equation of state with R as the gas constant and $\tilde{T}$ as the filtered temperature. The shear stress tensor τ_{ij} and the heat flux vector $\tilde{q_j}$ are given by -

$$\tilde{\tau_{ij}} = 2(\tilde{\mu} + \mu_t)\left(\tilde{S_{ij}} - \frac{1}{3}\tilde{S_{kk}}\delta_{ij}\right) \tag{2.20}$$

$$\tilde{q_j} = -C_p\left(\frac{\tilde{\mu}}{Pr} + \frac{\mu_t}{Pr_t}\right)\frac{\partial \tilde{T}}{\partial x_j} \tag{2.21}$$

where, S_{ij} is the filtered strain rate tensor (as defined previously), $\tilde{\mu}$ is the molecular viscosity which is assumed to follow the simple power law

$$\tilde{\mu} = \mu_0\left(\frac{\tilde{T}}{T_0}\right)^{\alpha} \tag{2.22}$$

the default value of α is 0.76. The turbulent Prandtl number Pr_t is fixed at 0.9 and the molecular Prandtl number Pr is kept constant at 0.76 by default. C_p is the specific heat capacity at constant pressure. The SGS terms are modeled by the linear eddy viscosity model, based on the Boussinesq hypothesis. The turbulent eddy viscosity μ_t arising from this is calculated using the Dynamic Smagorisnky Model proposed by Moin *et al.* (1991), with modifications by Lilly (1992).

2.6 Numerical Methods

CharLESx uses a cell centered finite volume method to discretize the governing equations 2.16, 2.17, 2.18, these equations in semi-discretized form for a cell i in a

structured/unstructured mesh can be written as (Khalighi *et al.* (2011))-

$$\frac{\partial \tilde{U}}{\partial t} V_{cv} + \sum_f (\tilde{F}^e + \tilde{F}^d) A_f = S V_{cv} \tag{2.23}$$

where V_{cv} is the constant cv volume, the state vector of conservative variables $\tilde{U}$ the inviscid Euler flux $\tilde{F}^e$ and the viscous diffusive flux $\tilde{F}^d$ are given as -

$$\tilde{U} = \begin{bmatrix} \bar{\rho} \\ \bar{\rho}\tilde{u_i} \\ \bar{\rho}\tilde{E} \end{bmatrix}, \tilde{F}^e(\tilde{U}) = \begin{bmatrix} \bar{\rho}\tilde{u_n} \\ \bar{\rho}\tilde{u_i}\tilde{u_n} + \bar{p}n_i \\ (\bar{\rho}\tilde{E} + \bar{p})\tilde{u_n}) \end{bmatrix}, \tilde{F}^d\tilde{U} = \begin{bmatrix} 0 \\ \tilde{\tau_{ij}} n_j \\ q_n + \tau_{ij} u_i n_j \end{bmatrix} \tag{2.24}$$

where n_i denotes outward normal of face f, and subscript n denotes the component in n_i direction. The solution vector $\tilde{U}_i$ is stored at the cell centroid for a finite volume cell centered method, where as the flux vectors $\tilde{F}^e$ and $\tilde{F}^d$ are defined at the face center of bounding faces of i. The euler flux is calculated using a two-step approach, which will be described below and the viscous diffusive flux $\tilde{F}^d$ is calculated using a simple central flux. The euler flux is calculated as follows -

1) Biased polynomial reconstruction to face centroid

For a control volume based scalar ϕ at an internal face f associated with a control volume to it's left (L) and right (R), the left and right states are reconstructed at the face centroid as follows (see figure 2.1)-

$$\phi_l = \phi_L + a_l(\phi_R - \phi_L) + b_l \cdot \nabla\phi_L \tag{2.25}$$

$$\phi_r = \phi_R + a_r(\phi_L - \phi_R) + b_r \cdot \nabla\phi_R \tag{2.26}$$

where $\phi = \bar{\rho}, \tilde{u_i}, \bar{p}$ are the filtered primitive variables, a_l, b_l, a_r, b_r are the reconstruction coefficients and Δ_L and Δ_R are the second order gradients associated with the left and right control volumes. Consider the case of a cartesian grid with uniform spacing in the x-direction as shown in figure 2.2. For this case, the coefficients are

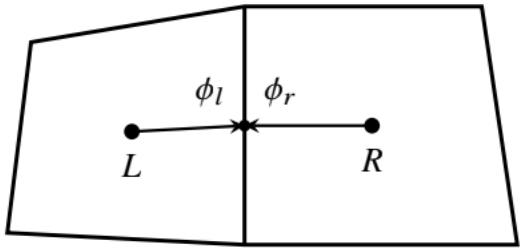

Figure 2.1: 2D Representation of Two Neighbouring Control Volume Representing the Left and Right States Associated With a Given Face

$a_l = a_r = 1/6, b_l = [h/3, 0, 0]$ and $b_r = [-h/3, 0, 0]$. Then the x-gradients at cell L is evaluated as follows (Khalighi *et al.* (2011)) -

$$\left.\frac{\partial \phi}{\partial x}\right|_L = \frac{\phi_R - \phi_{LL}}{2h} \tag{2.27}$$

Therefore, the reconstruction scheme reduces to the following quadratic polynomial for a uniform cartesian grid -

$$\phi_l = -\frac{1}{6}\phi_{LL} + \frac{5}{6}\phi_L + \frac{1}{3}\phi_R \tag{2.28}$$

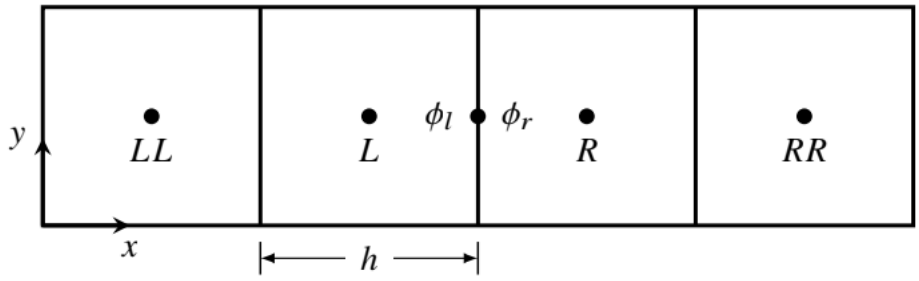

Figure 2.2: 2-d Schematic of the Flux Reconstruction in a Uniform Cartesian Mesh

It is essentially a third order quadratic upwinding scheme (QUICK, Park and Moin (2016)), and a similar procedure is used to calculate the x-gradients at cell R. The code switches to a second-order ENO reconstruction scheme when shocks are detected in the flow, which are essentially large density gradients that are detected

by shock sensors.

2) Euler flux computation using a blend of centered and upwind-biased Riemann flux

Flux vectors are calculated using the reconstructed values ϕ_l and ϕ_r at the face center. The Euler flux is calculated using a blend of a non-dissipative central flux and a dissipative HLLC upwinding flux

$$\tilde{F}^e = (1-\alpha)F_{central} + \alpha F_{HLLC}, \alpha\epsilon[0,1] \tag{2.29}$$

where α is a blending parameter whose value lies between 0 to 1. CharLESx uses an explicit sub-grid model to compute α, and varies it's value at any spatial location depending on the grid quality at that location. If the local grid quality is good, α can be set to 0, which also avoids excessive numerical dissipation due to upwinding. However in regions of less-than-perfect grid quality, the central scheme can introduce numerical instabilities that must be prevented from contaminating the solution by locally increasing the value of α (Khalighi *et al.* (2011)). The flux term $\tilde{F}_{central}$ in equation 2.29 is obtained by combining ϕ_l and ϕ_r with equal weights, and $\tilde{F}_{HLLC}$ is obtained by solving the Riemann problem at the face with left and right reconstructed states, using the HLLC Riemann solver (Toro *et al.* (1994)). The numerical method is second order accurate in space for generally unstructured mesh, but upgrades to a fourth-order accuracy on a cartesian mesh (Park and Moin (2016)). The discretized equations are advanced in time using an explicit third-order low storage Runge-Kutta scheme.

Chapter 3

SIMULATION SET UP

In this work, primarily, four cases are studied for characterizing the flow field of a jet and it's interaction with a flat plate. First two cases deal with a jet placed in a 'free' configuration, i.e. the jet is free to expand in the ambient air without any hindering surface near it. Two free jet cases will be discussed - the first one is discretized with 8 million control volumes, and the second case is discretized with 15 million control volumes, to characterize the effect of grid refinement on flow characteristics. Second two cases deal with the jet placed in an 'installed jet' configuration, i.e., the jet is placed with a tangential plate at a certain radial distance from the nozzle's exit. The plate's impact on the flow characteristics and more importantly the production of noise is studied in the two cases. In the first case, the simulation domain is discretized with 22 million control volumes, and in the second case, with 40 million control volumes, not only to study the effect of grid refinement on the flow characteristics, but also try to find it's effect on the pressure measurements at the plate surface. Since we are dealing with a Large Eddy Simulation, the effect of grid refinement on wall pressure characteristics may not be as intuitive as thought and hence must be treated cautiously, as will be seen in the subsequent sections.

3.1 Free Jet - 8 Million Cells

In this case, flow through a converging nozzle at a mach number of 0.35 is analyzed. The nozzle is placed in a computational domain with the ambient fluid as air at a pressure of $101325Pa$ (atmospheric pressure at mean sea level), and ambient temperature of $300K$. Air is used as the operating fluid, which is accelerated by the

nozzle to a Mach number of 0.35 at the nozzle exit, with the resulting jet free to expand in the ambient fluid, without any hindrance. The results from this simulation will be validated using data from experiments performed by Mancinelli and Camussi (2018) and will be discussed in chapter 4. The nozzle geometry was provided courtesy of Dr. Roberto Cammussi, and was generated using Solidworks 2019. An isometric view of the nozzle is show in figure 3.1 and a sectional view through the mid plane of the nozzle is shown in figure 3.2.

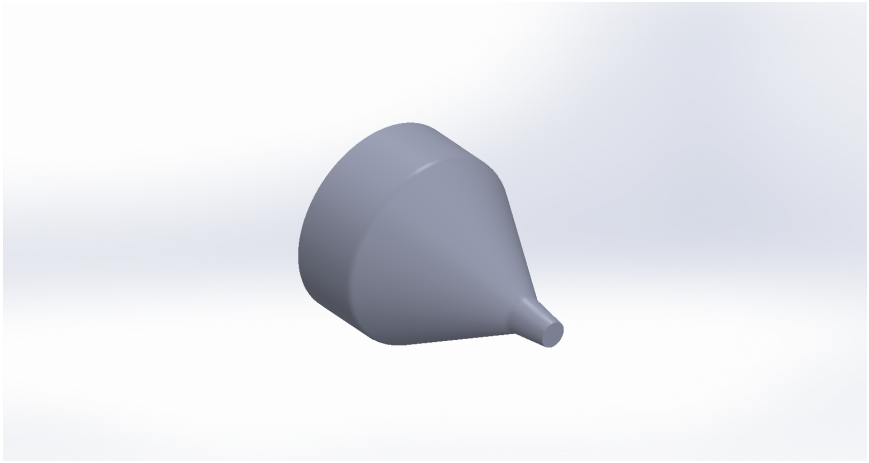

Figure 3.1: Isometric View of Nozzle

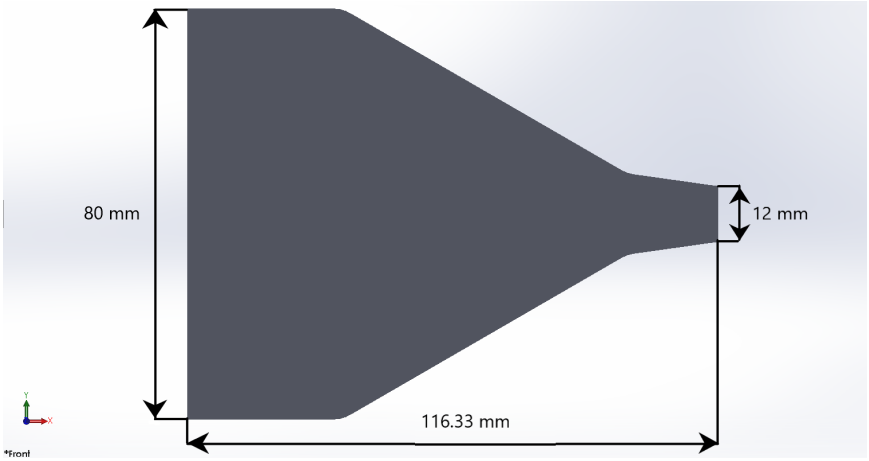

Figure 3.2: Sectional View of the Nozzle

3.1.1 Grid Generation

The nozzle geometry file generated by Solidworks was imported to Pointwise V18.3R2 for generating a 3D computational grid. As the nozzle is axisymmetric, it was meshed using an unstructured mesh with an O-H topology, to avoid a singularity/pole at the nozzle inlet and exit. Hexahedral cells are used for generating the volumetric mesh, with 128 grid points in the azimuthal direction, 60 in the radial and 120 points in the streamwise direction. An isometric view of the nozzle grid is shown figure 3.3, figure 3.4 shows the O-H grid at the nozzle inlet and figure 3.5 shows the same at the nozzle exit.

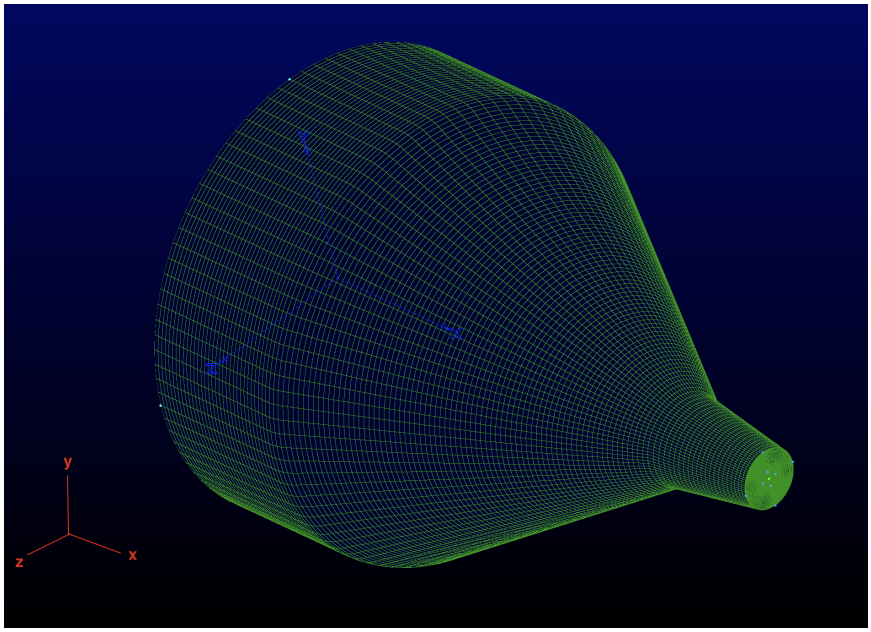

Figure 3.3: Isometric View of Nozzle Mesh

Once the nozzle meshing is complete, a cylindrical block was generated around it to simulate the freejet experimental conditions given in the aforementioned paper by the above Mancinelli and Camussi (2018). The coordinate origin of the entire domain is chosen at the center of the nozzle inlet ($x = 0$, $y = 0$, $z = 0$, $r = 0$), as can be seen in figure 3.6 by the axis in white. The cylindrical domain extends to $55D$ (where

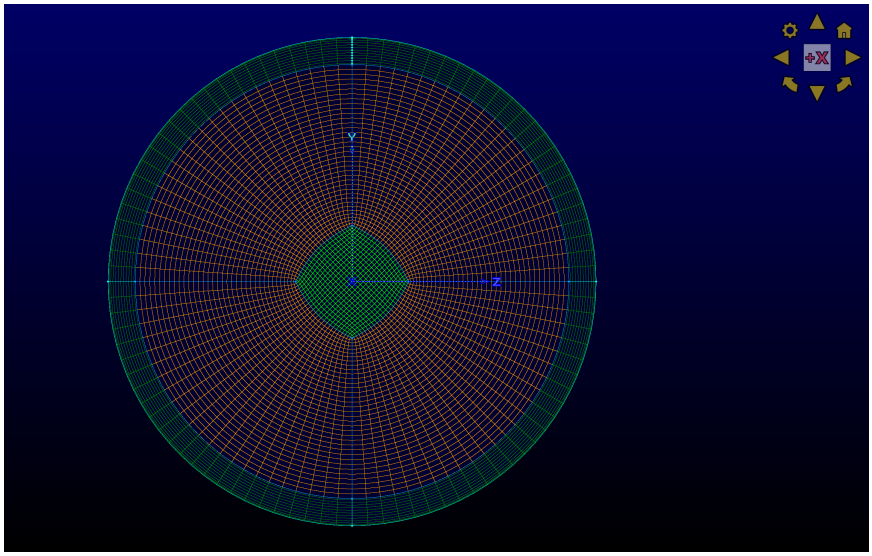

Figure 3.4: Nozzle Inlet

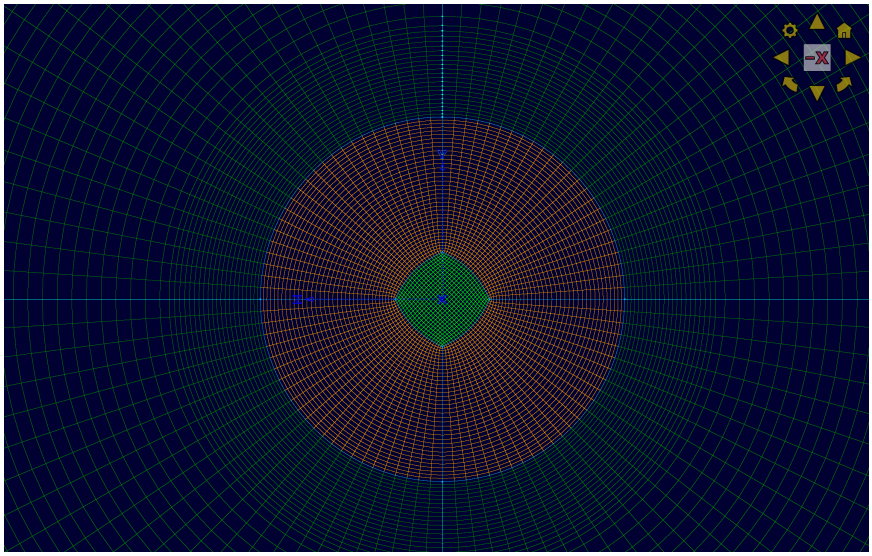

Figure 3.5: Nozzle Exit

$D = 12mm$ is the diameter of the nozzle exit) in the positive x-direction and $10D$ in the negative x-direction. So, the grid has a length of $65D$ in the streamwise direction and $20D$ in the radial direction. Figure 3.6 shows an isometric view of the full domain along with these dimensions. A schematic of the entire computational grid is shown in figure 3.7, with the grid split into two parts -

1) Physical domain (represented by the blue zone), which extends from $x = 0D$ to

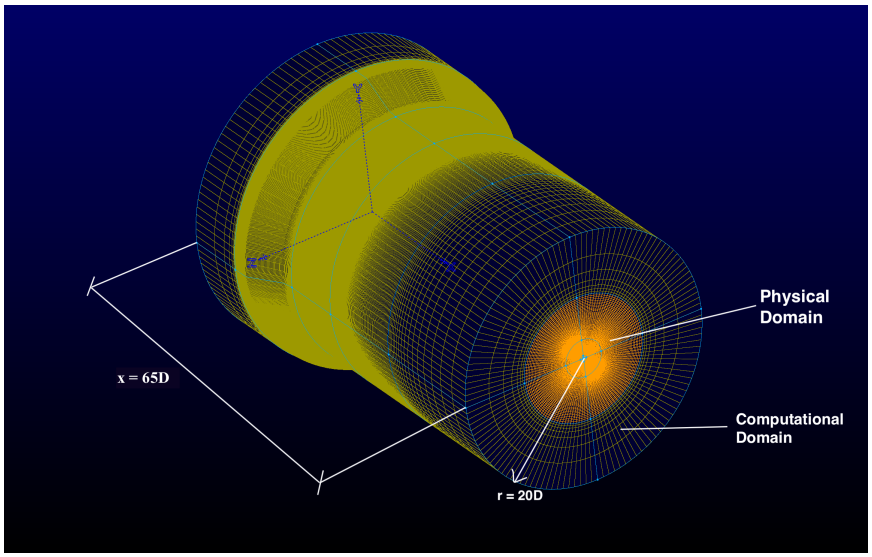

Figure 3.6: Computational Grid Schematics

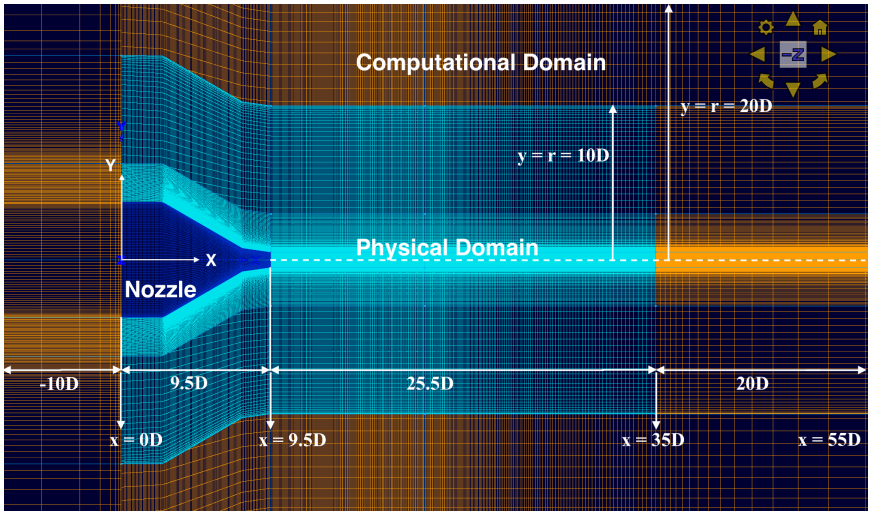

Figure 3.7: Computational Grid Schematics

$x = 35D$ in the streamwise direction and from $r = 0D$ to $r = 10D$ in the radial direction;

2) Computational domain (represented by the orange zone), which stretches from $x = -10D$ to $x = 0D$ and $x = 35D$ to $55D$ in the streamwise direction, and $r = 10D$ to $r = 20D$ in the radial direction.

In turbulent jet simulations, grid generation is the most important part, as the capturing of sub-grid scale effects is directly dependent on the cell size, type and refinement

in key regions of the flow. The grid must be sufficiently refined in key regions of flow, where the development of these small scales will have a major impact on the large scale structures of the flow, such as in the boundary layer along the nozzle walls and at the nozzle exit, where there is a development of a shear layer and its mixing with the ambient fluid. However, it must also be noted that the increase in refinement leads to a decrease in time step size and a consequent increase of simulation time.So, there is a trade-off between the simulation time and the grid refinement, hence, the grid should only be sufficiently refined in the key regions as mentioned above and stretched in other regions of flow to keep the simulation time reasonable, and also maintain the CFL number within 0.9 - 1.0 to maintain numerical stability.

In figure 3.8, the highlighted region (coloured in cyan), shows the mixing zone of the jet, where there are essentially two streams of flow mixing with each other - 1) jet at a mach number of 0.35 exiting from the nozzle and 2) ambient fluid at rest. This leads to the development of a Kelvin-Helmholtz instability and the formation of a shear layer along the nozzle lip-line. This shear layer expands radially in all directions, converging inwards from $-0.5D < r < 0.5D$, forming the 'potential core' of the jet, and expanding outwards at $r > |0.5D|$. This phenomenon causes a mixing of the two streams, and dictates the overall structure of the jet flow. To capture this phenomenon, the grid is refined up to a distance of $x = 10D, r = 3D$ from the nozzle exit, and is stretched in all other regions, to reduce the number of cells and minimize simulation time as stated above. Purely hexahedral cells are used throughout the entire domain to generate the volume mesh. The grid specifications are given in table 3.1.

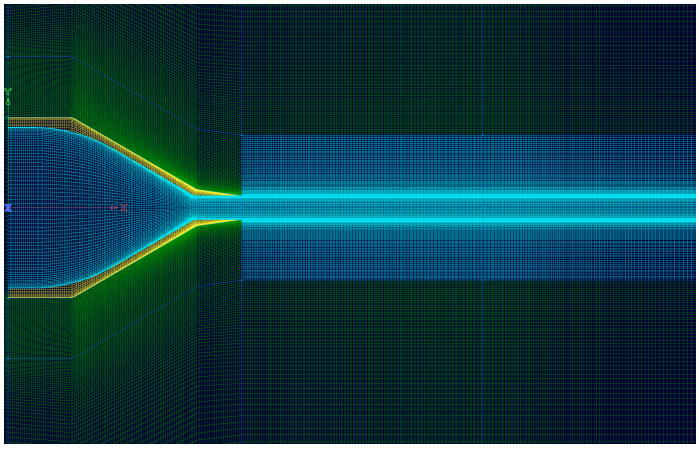

Figure 3.8: Cross Section of Domain Along Z = 0 Plane, Showing Grid Refinement in the Nozzle Exit Region

Table 3.1: Mesh Specifications

Region	Number of cells	Average spacing (δ_x/D)
Physical domain	7.06 million	
Computational domain	763,103	
Total	7,823,104	
$9.5D < x < 20D, -3D < r < 3D$	2.88 million	0.0625
$20D < x < 35D, -3D < r < 3D$	2.08 million	0.125

Here, the average spacing refers to the average cell length in the streamwise direction (δ_x), normalized by the nozzle diameter ($D = 12mm$). The grid spacing in the radial direction (δ_r) is given in table 3.2 and a cross sectional view of the grid at the nozzle outlet is shown in figure 3.9. The grid spacing near the nozzle walls in the radial direction is $\delta_r/D = 0.009525$ and stretches to $\delta_r/D = 0.3$ at $r/D = 10$, i.e. end of

the physical domain, to ensure sufficient resolution of boundary layer at the nozzle exit wall and also ensure proper radial cell spacing in the mixing zone of the jet.

Table 3.2: Mesh Specifications - Radial Direction

Region	Average spacing (δ_r/D)
$-0.5D < r < 0.5D$	0.012
$0.5D < r < 3D$	0.066
$3D < r < 10D$	0.155

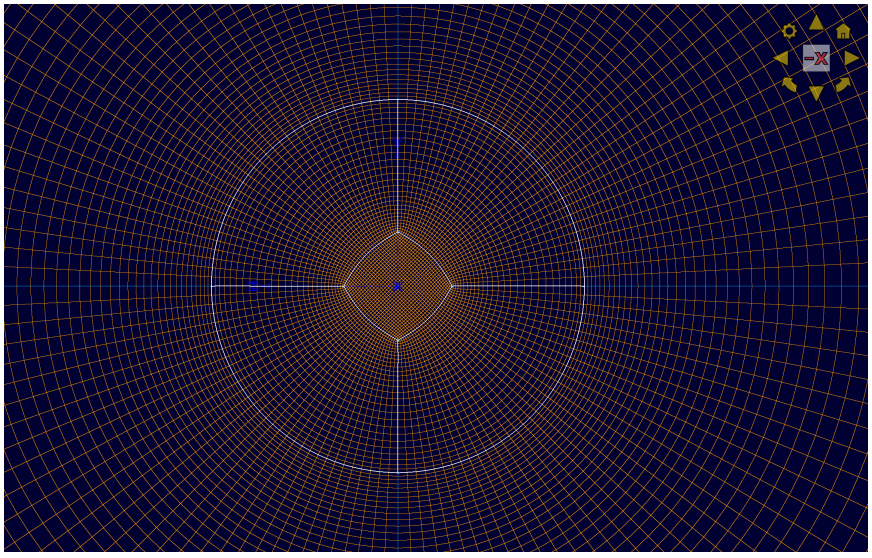

Figure 3.9: Cross Section of Domain at Nozzle Exit, Showing Grid Refinement in the Nozzle Exit Region

3.1.2 Physics Set Up

The ambient pressure and temperature in the flow domain (outside the nozzle) is assumed to be $101325Pa$ and $300K$. The flow through the nozzle is assumed to be ideal, isentropic, isothermal and the flow at the exit of the nozzle is fully expanded. The temperature of air at the inlet of the nozzle is $300K$, and the pressure at the

inlet is calculated from the isentropic theory of nozzle flow. The mach number of the flow at the exit is required as 0.35, according to the freejet experiment conditions as set by Mancinelli and Camussi (2018). Therefore, as per the isentropic model of the nozzle, the static pressure at the exit of the nozzle will be the same as that at the inlet, and it can be calculated based on the total-to-static relation as -

$$\frac{P_{ti}}{P_e} = \left[1 + \frac{(\gamma - 1)}{2} M_e^2\right]^{\frac{\gamma}{(\gamma-1)}} \tag{3.1}$$

where P_{ti} is the total pressure at the nozzle inlet, P_e is the static pressure at the nozzle exit, which is also equal to the atmospheric pressure. M_e is the mach number at the exit of nozzle, which is set to 0.35 and $\gamma = 1.4$ is the ratio of specific heats. The total pressure at the inlet is thus found to be **110282.977 Pa**. The flow at the inlet of the nozzle can be roughly assumed to be laminar, as the Reynolds number is $\sim$ 14,490 and turbulence intensity is 0.61%. The dynamic viscosity of air is set as $1.789 * 10^{-5} Pa - s$, the density of air is set as $1.1768 kg/m^3$, and the ideal gas law is used as the equation of state. As stated in Chapter 2, the Favre filtered compressible Navier-Stokes equations are solved and the Dynamic Smagorinsky Model is used for modelling the sub-grid scale stress. The turbulent Prandtl number Pr_t is set as 0.9.

3.1.3 Boundary Conditions

The computational domain for the freejet has to be modelled as 'open atmosphere', hence the domain is split into 7 control surfaces to impose the boundary conditions as follows -

1) Nozzle inlet

2) Nozzle wall interior surface

3) Nozzle wall exterior surface

4) Domain inlet

5) Domain outlet

6) Domain far field right (considering positive streamwise direction)

7) Domain far field left (considering positive streamwise direction)

Figures 3.10 to 3.16 illustrate all of these control surfaces in order.

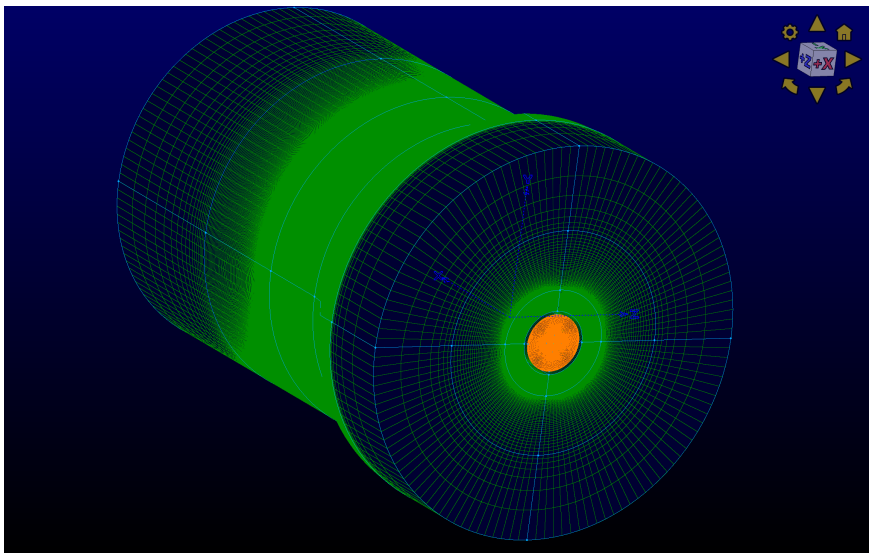

Figure 3.10: Nozzle Inlet, Highlighted by Orange

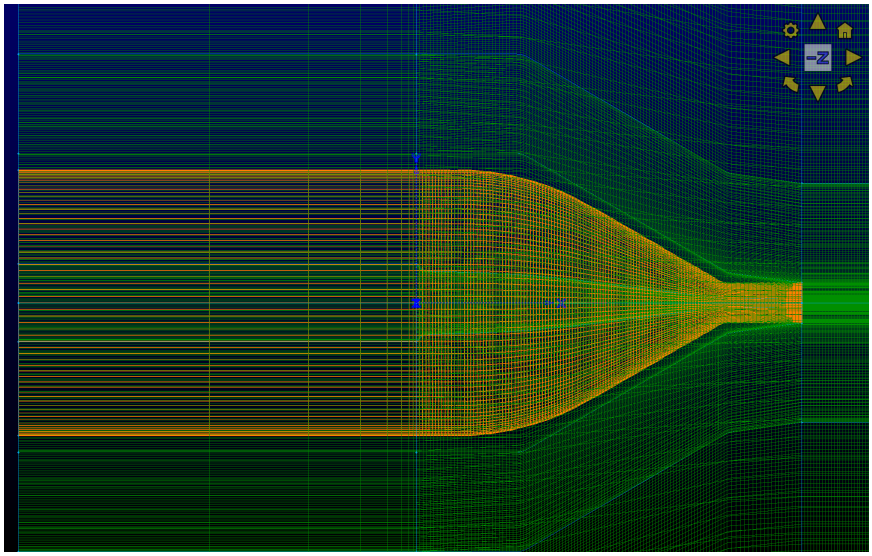

Figure 3.11: Nozzle Interior Wall, Highlighted by Orange

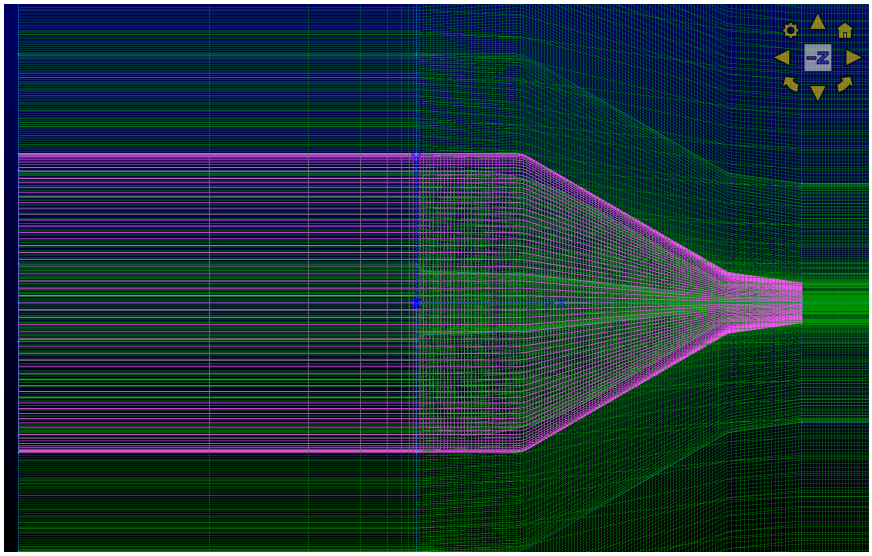

Figure 3.12: Nozzle Exterior Wall, Highlighted by Pink

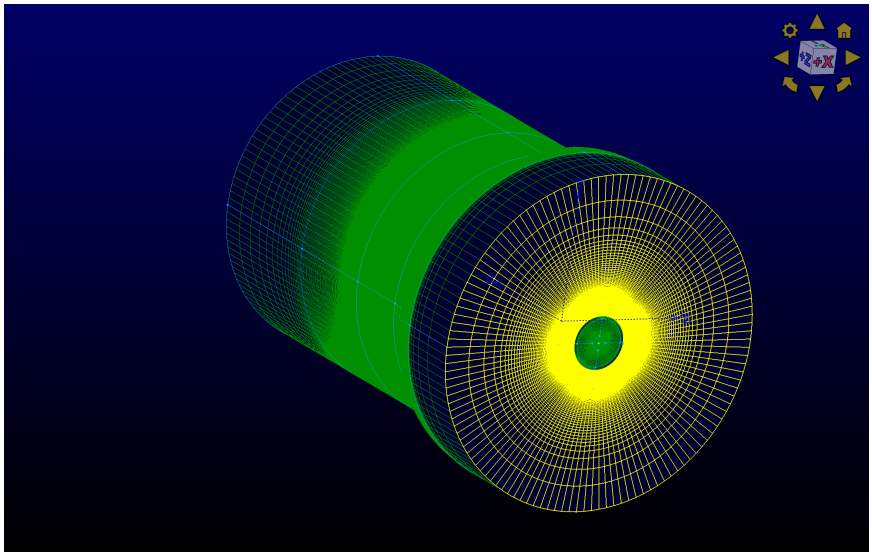

Figure 3.13: Domain Inlet, Highlighted by Yellow

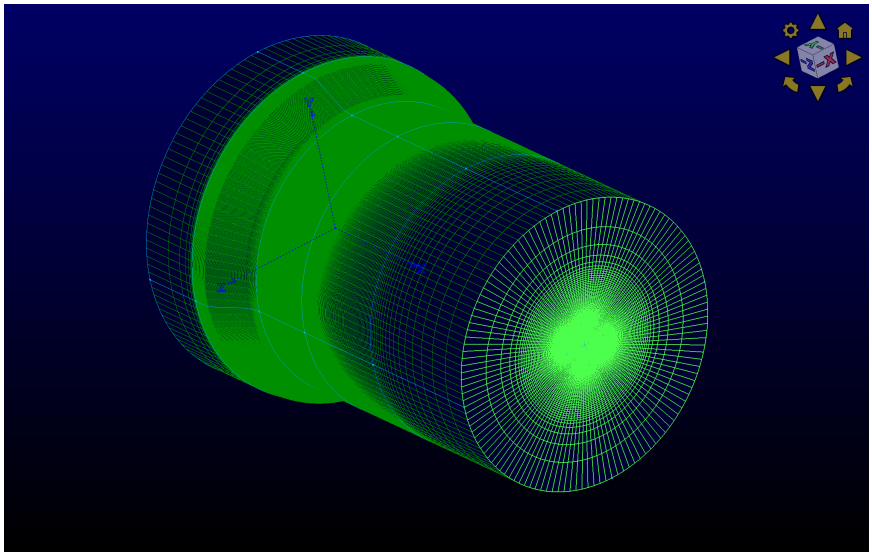

Figure 3.14: Domain Outlet Highlighted by Bright Green

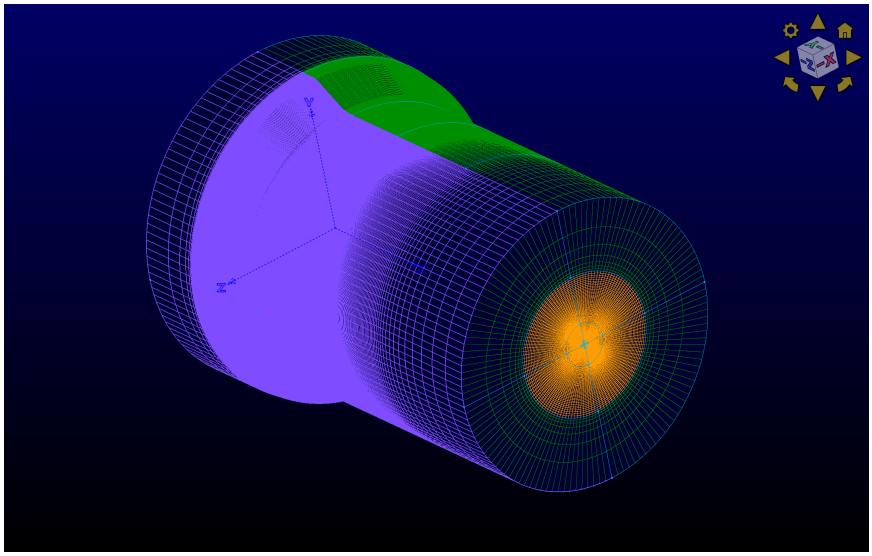

Figure 3.15: Domain Far Field Right, Highlighted by Purple

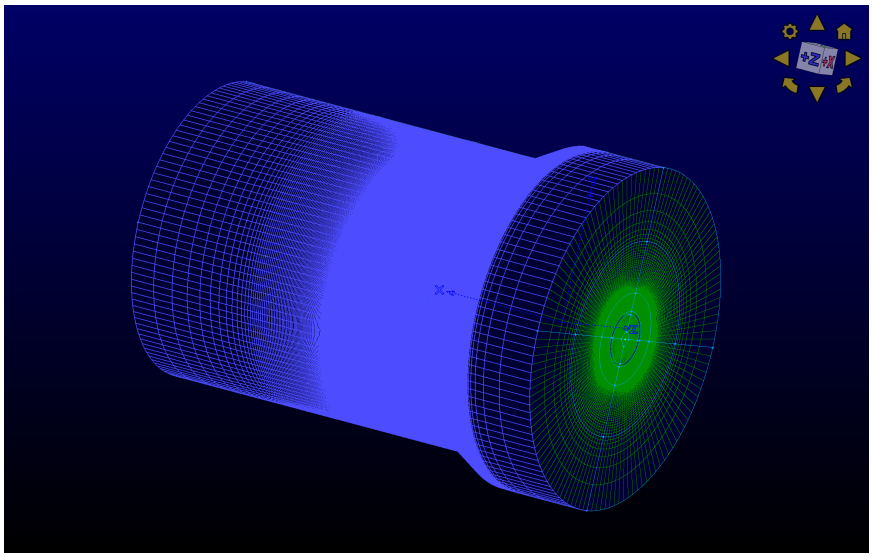

Figure 3.16: Domain Far Field Left, Highlighted by Purple

Table 3.3: Boundary Conditions

Surface	Type	Total Pressure (Pa)	Total Temperature (K)
Nozzle Inlet	'Pressure Inlet'	110282.977	300
Nozzle wall interior surface	Adiabatic wall		
Nozzle wall exterior surface	Adiabatic wall		
Domain inlet	'Pressure Inlet'	101325	300
Domain outlet	'Pressure Outlet'	101325	300
Domain far field right	'Pressure Inlet'	101325	300
Domain far field left	'Pressure Inlet'	101325	300

The nozzle interior and exterior walls are modelled as adiabatic since there is no heat transfer occurring through these surfaces. Although CharLESx does not explicitly have a 'Pressure Inlet' boundary condition, it allows setting of total Pressure and total temperature when the mass flux/velocity through that surface is unknown. Thus, the nozzle inlet, domain inlet and domain far fields are defined with a total pressure and total temperature as stated in table 3.3 and named as a 'Pressure Inlet'. Similarly, the domain outlet is set as a Pressure outlet, to model it as an outflow surface. A pressure of 101325 Pa and temperature of 300 K is set to the domain inlet, outlet and far field to model it as the surrounding 'open atmosphere', or, the quiescent fluid. A pressure of 110282.977 Pa and temperature of 300 K is set to the nozzle inlet as per equation 3.1.

3.2 Free Jet - 22 Million Cells

This case is a continuation of the previous case, but the grid is refined to 22 million cells/control volumes to produce more accurate results and check the effect of grid refinement on flow characteristics. Therefore the nozzle geometry, simulation physics and boundary conditions remain the same as the free jet 8 million cells case with the only difference of internal grid refinement.

3.2.1 Grid Generation

The grid consists of unstructured hexahedral cells with 22 million cells making up the flow domain and 196x512x256 points in the azimuthal, streamwise and radial direction. Similar to the previous case, the coordinate axis is located at the center of the nozzle inlet and a cylindrical grid is constructed around the nozzle body. The cylindrical domain extends to $55D$ (where $D = 12mm$ is the diameter of the nozzle exit) in the positive x-direction and $10D$ in the negative x-direction. So, the grid has

a length of $65D$ in the streamwise direction and $20D$ in the radial direction.

An isometric view of the entire computational grid is shown in figure 3.18, showing the structure of the grid and figure 3.17 shows a cross section of the grid along the XY plane (at z = 0). The grid is split into two parts -

1) Physical domain (represented by the cyan block), which extends from $x = 0D$ to $x = 35D$ in the streamwise direction and from $r = 0D$ to $r = 10D$ in the radial direction;

2) Computational domain (represented by the orange block), which stretches from $x = -10D$ to $x = 0D$ and $x = 35D$ to $55D$ in the streamwise direction, and $r = 10D$ to $r = 20D$ in the radial direction. A full schematic of the mesh is given in figure 3.17 and a detailed breakdown of mesh statistics is given in table 3.4.

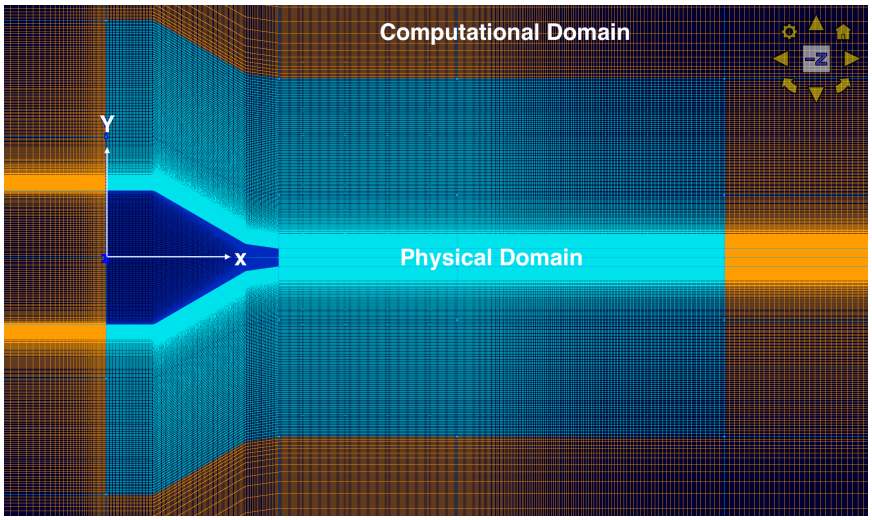

Figure 3.17: Computational Grid Schematics for Free Jet Case With 22 Million Cells

As mentioned in section 3.1.1, the grid is refined further in the region $9.5D < x < 20D$, $-3D < r < 3D$ and $20D < x < 35D$, $-3D < r < 3D$ by 1.5 times to better capture flow characteristics in the mixing zone of the jet. The average spacing in the

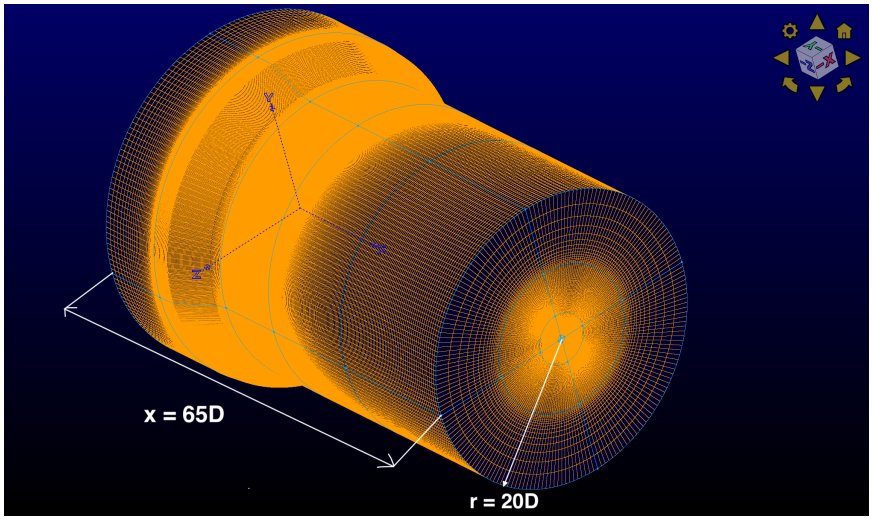

Figure 3.18: Computational Grid Schematics for Free Jet Case With 22 Million Cells

Table 3.4: Mesh Specifications for 22 Million Case

Region	Number of cells	Average Spacing (δ_x/D)
Physical Domain	16,507,757	
Computational Domain	5,413,814	
Total	21,921,571	
$9.5D < x < 20D, -3D < r < 3D$	4.43 million	0.0625
$20D < x < 35D, -3D < r < 3D$	3.32 million	0.125

streamwise direction was maintained the same as that in the 8 million cells case, but the grid resolution in the radial and azimuthal direction was increased, because the flow characteristics of a freejet are more dependent on the grid resolution in these directions, than the streamwise direction. A brief overview of the mesh statistics is given in table 3.5.

Table 3.5: Mesh Specifications - Radial Direction

Region	Average Spacing (δ_r/D)
$-0.5D < r < 0.5D$	0.01195
$0.5D < r < 3D$	0.0285
$3D < r < 10D$	0.1

The grid spacing is maintained in the region $-0.5D < r < 0.5D$, it was increased by 2 times in the region $0.5D < r < 3D$ and by 1.5 times in the region $3D < r < 10D$ to better capture the flow statistics in the mixing zone of the jet.

3.2.2 Physics Set Up

As this case is just a refined grid version of the 8 million cells case, the physics set up remain the exactly the same as in section 3.1.2.

3.2.3 Boundary Conditions

The boundary conditions also remain the same as in section 3.1.3 as the mesh structure and simulation case remains the same. A summary of boundary conditions is given in table 3.6 and an illustration of these surfaces is given in figures 3.19 to 3.25.

Table 3.6: Boundary Conditions

Surface	Type	Total Pressure (Pa)	Total Temperature (K)
Nozzle Inlet	'Pressure Inlet'	110282.977	300
Nozzle wall interior surface	Adiabatic wall		
Nozzle wall exterior surface	Adiabatic wall		
Domain inlet	'Pressure Inlet'	101325	300
Domain outlet	'Pressure Outlet'	101325	300
Domain far field right	'Pressure Inlet'	101325	300
Domain far field left	'Pressure Inlet'	101325	300

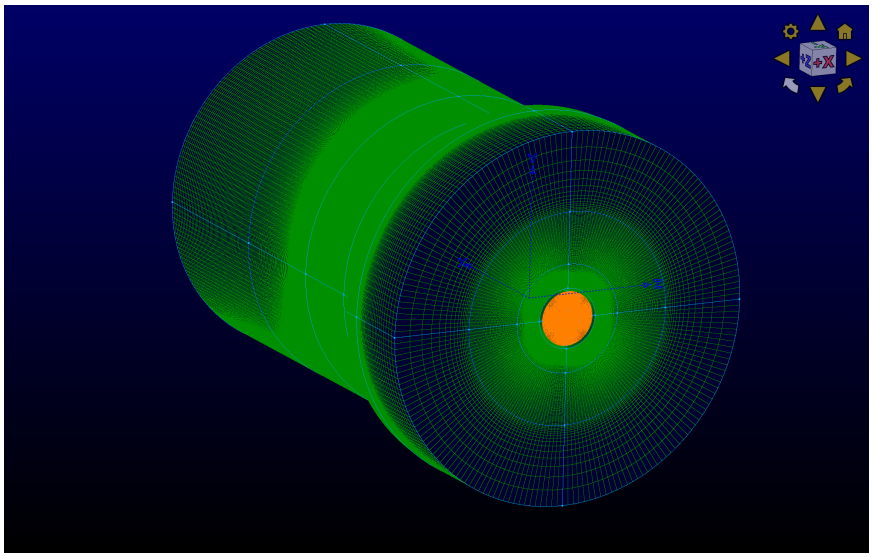

Figure 3.19: Nozzle Inlet, Highlighted by Orange

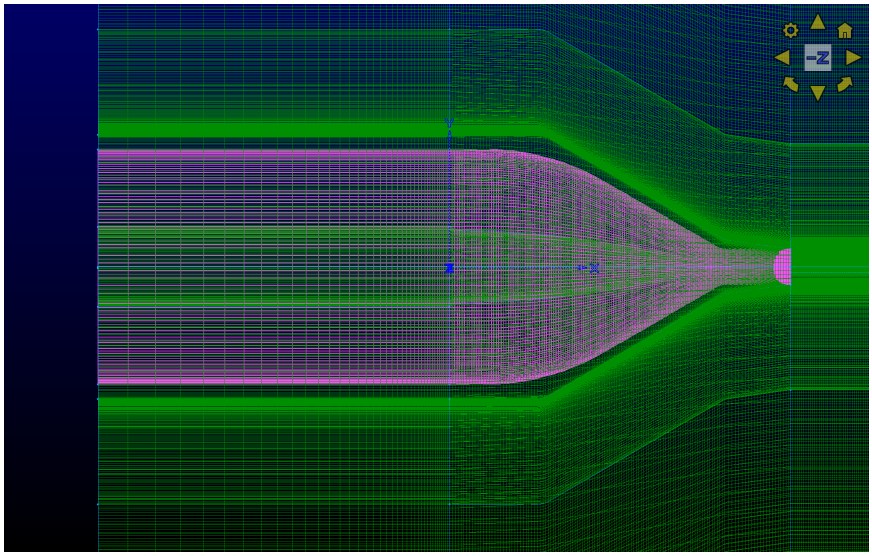

Figure 3.20: Nozzle Interior Wall, Highlighted by Pink

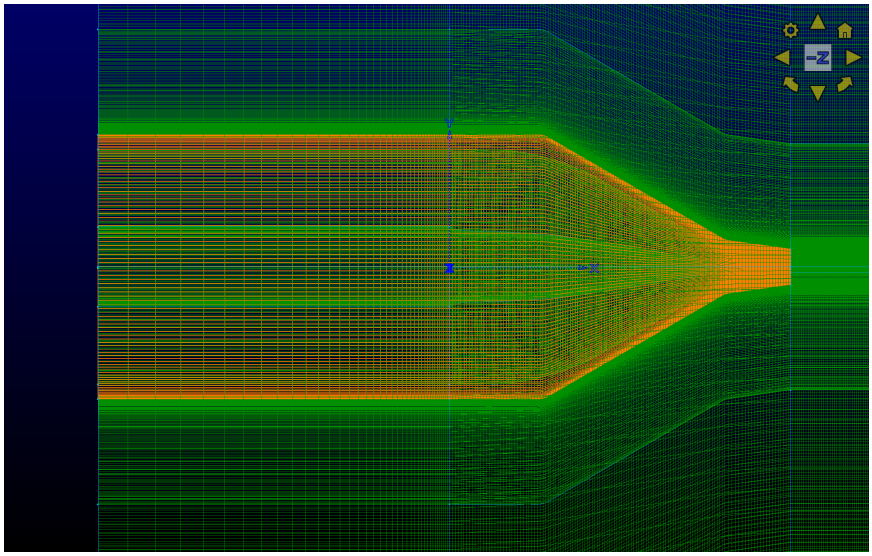

Figure 3.21: Nozzle Exterior Wall, Highlighted by Orange

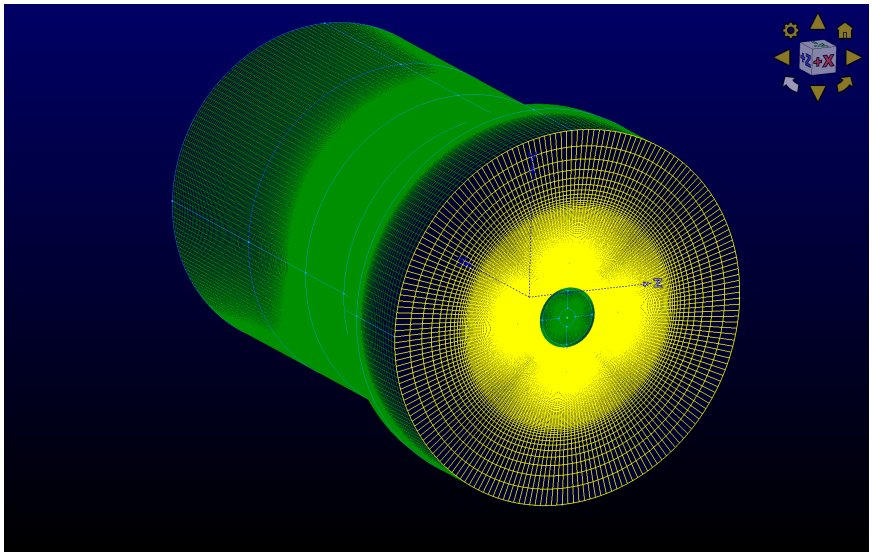

Figure 3.22: Domain Inlet, Highlighted by Yellow

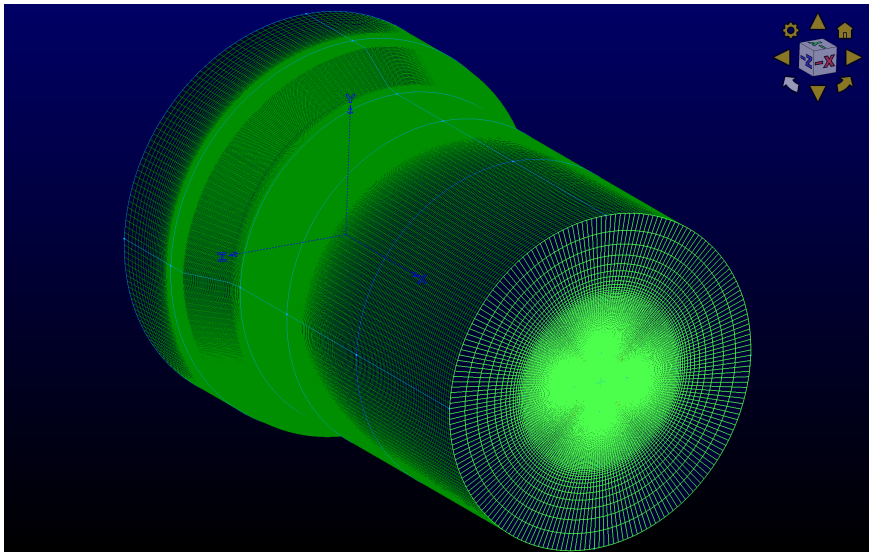

Figure 3.23: Domain Outlet Highlighted by Bright Green

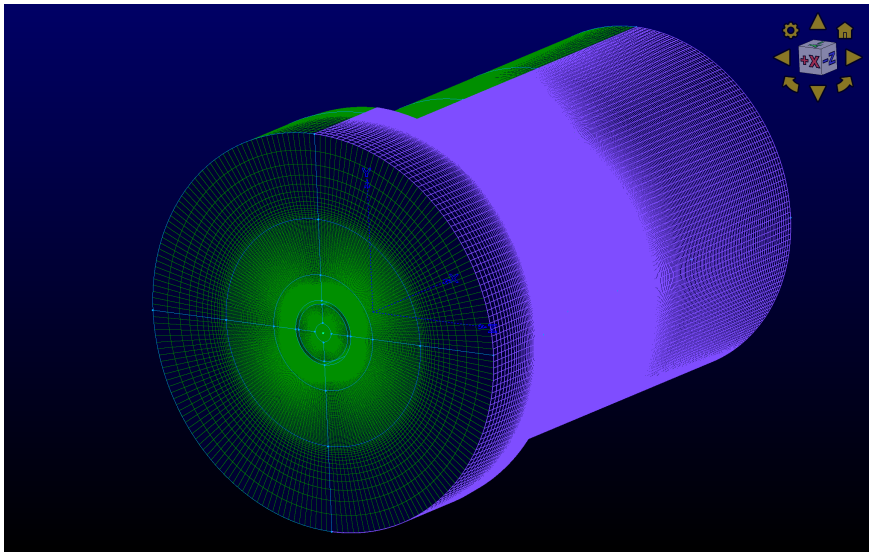

Figure 3.24: Domain Far Field Right, Highlighted by Purple

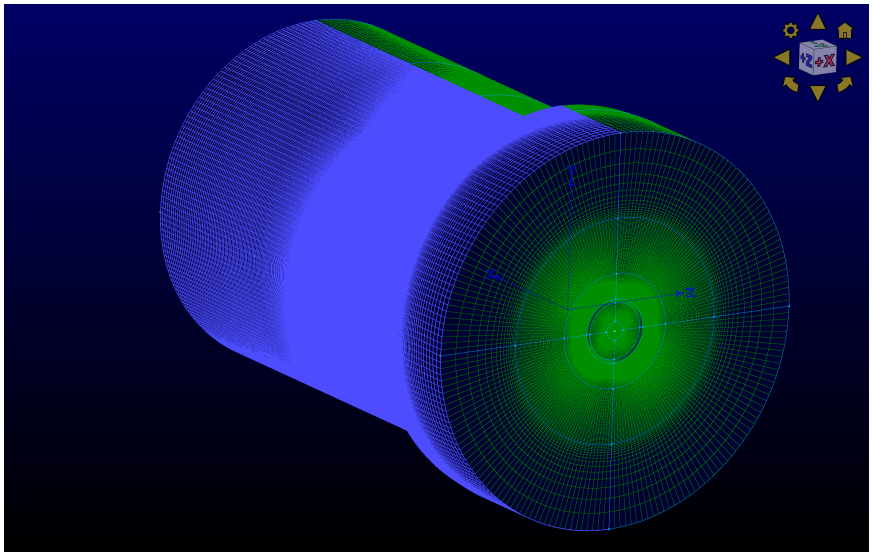

Figure 3.25: Domain Far Field Left, Highlighted by Purple

3.3 Installed Jet - 15 Million Cells

In this case, flow through the same converging nozzle is analyzed, however the flow speed at the nozzle exit is higher, at mach 0.7, and a flat plate is placed at a distance of $2D$ (where $D = 12$ mm is the nozzle exit diameter) radially below the nozzle exit center. This set-up is analyzed to check the effect of the flat plate on the jet flow characteristics and the impact it has on the sound produced by this high speed flow. A computational domain is built around this set-up and it is assumed that the entire set-up is placed in environment with standard atmospheric pressure and temperature (101325 Pa and $300K$). The results from this simulation will be validated from experiments performed by Meloni *et al.* (2019), and additional statistics will also be analyzed along the plate surface to utilize the spatially resolved data, otherwise not available with a traditional experimental set-up.

3.3.1 Grid Generation

Due to the presence of a flat plate below the nozzle exit, a complex interaction between the jet and the plate takes place, which modifies the flow characteristics of the jet significantly as compared to the freejet case. A combination of the Coanda effect, formation of a Turbulent Boundary Layer (TBL) along the plate surface and the mixing phenomenon discussed in section 3.1.1 make grid refinement in these regions critical to best capture the turbulence phenomenon and the wall pressure induced on the plate surface. Also, as CharLESx does not support prismatic elements in a grid, purely hexahedral cells have be used for grid generation. Automatic mesh refinement is also not available in CharLESx, so these factors complicate the grid generation process for installed jet case. The grid has to be refined manually in the regions described above, and a completely new grid has to be generated for every

refinement step. Finally, the effect of grid refinement on time step size has to be taken into consideration, as any level of refinement leads to a significant decrease of time step size, and a consequent increase in simulation time, therefore, only small level of refinements can be made a time. Taking all these factors into consideration, a grid with 15 million cells was chosen for the simulation.

The grid consists of unstructured hexahedral cells with 15 million cells and 96x300 x100 grid points in the azimuthal, streamwise and radial direction. The coordinate axis of the domain is located at the center of the nozzle inlet and a cuboid shaped domain is constructed around the nozzle and flat plate to simulate the flow conditions in an experiment wind tunnel. The grid domain extends to $55D$ in the positive x-direction and $10D$ in the negative x direction from the origin. The flat plate is located at a distance of $2D$ from the center of the nozzle inlet to mimic the set up as given in Meloni *et al.* (2019), where D is the nozzle outlet diameter (12 mm). The grid extends to $40D$ in the spanwise direction, 22D in the vertical direction (y-direction, as shown in figure 3.26). As with the freejet case, the domain is split into two parts - 1) Physical domain (represented by the blue block in figure 3.27), which extends from $x = 0D$ to $x = 35D$ in the streamwise direction, $y = -2D$ to $10D$ in the vertical direction and $z = -10D$ to $10D$ in the spanwise direction.

2) Computational domain (represented by the orange block) which stretches from $x = -10D$ to $x = 0D$ and $x = 35D$ to $x = 55D$ in the streamwise direction, $z = -10D$ to $-20D$ and $z = 10D$ to $z = 20D$ in the spanwise direction, $y = -2.1D$ to $y = -7D$ and $y = 10D$ to $y = 20D$ in the vertical direction. A gap of $y = -0.1D$ was purposefully left between $x = 9.5D$ to $x = 55D$ and $z = -20D$ to $z = 20D$ to model the flat plate in the flow domain.

A full schematic of the mesh is given in figure 3.27 and a detailed breakdown of mesh statistics is given in table 3.7 and table 3.8.

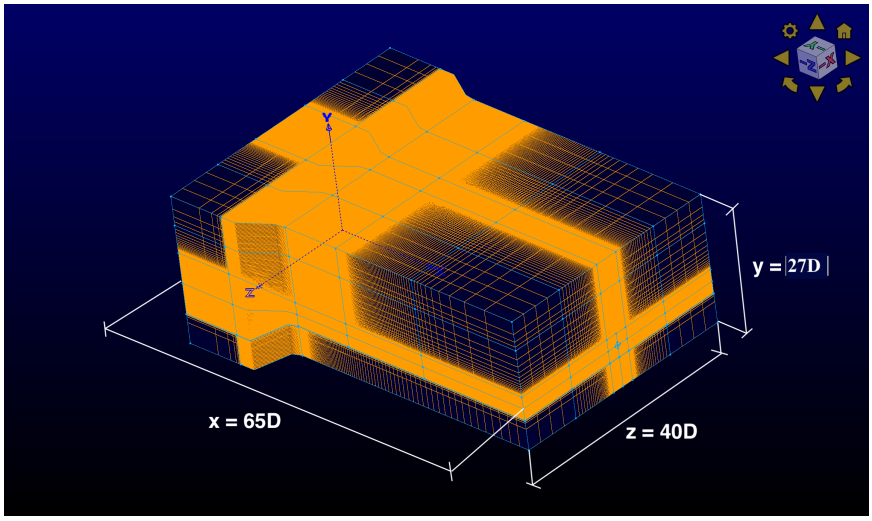

Figure 3.26: Computational Grid for Installed Jet Case With 15 Million Cells

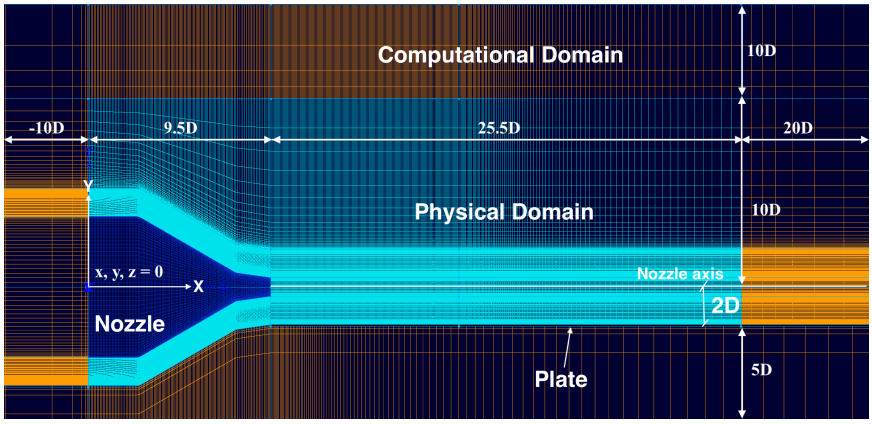

Figure 3.27: Computational Grid Schematics for Installed Jet Case With 15 Million Cells

The grid is refined in the region $9.5D < x < 35D, -2D < y < 2D, -2D < z < 2D$ to capture the mixing of the two streams of fluid (i.e. high speed jet and ambient fluid at rest), and $9.5D < x < 55D, y = -2D, -20D < z < 20D$, i.e. the mesh just above the flat plat to capture the development of the turbulent boundary layer.

Table 3.7: Mesh Specifications in Streamwise Direction

Region	Number of cells	Average Spacing (δ_x/D)
Physical Domain	11,884,869	
Computational Domain	3,262,232	
Total	14,933,520	
$9.5D < x < 20D, -2D < y < 2D, -2D < z < 2D$	3.26 million	0.06
$20D < x < 35D, -2D < y < 2D, -2D < z < 2D$	1.572 million	0.1875

Table 3.8: Mesh Specifications in Spanwise Direction

Region	Average spacing in the z-direction (δ_z/D)	Average spacing in the y-direction (δ_y/D)
$-0.5D < y, z < 0.5D$	0.01025	0.01025
$-2D < y, z < 2D$	0.038	0.02625
$y = -2D$ (Near plate surface)	0.038	0.02

3.3.2 Physics Set Up

The ambient pressure and temperature in the flow domain is assumed to be 101325 Pa and 300 K. The flow through the nozzle is assumed to be ideal, isentropic, isothermal, and the flow at the exit of the nozzle is fully expanded. The total temperature of air at the inlet of the nozzle in 300 K, and the pressure at the inlet is calculated based on isentropic theory of nozzle flow. The mach number of flow at the exit is required as 0.7, according to the experiment conditions set in Meloni *et al.* (2019).

Therefore, the total pressure at the inlet of the nozzle can be calculated based on the total to static relation as -

$$\frac{P_{ti}}{P_e} = \left[1 + \frac{(\gamma - 1)}{2} M_e^2\right]^{\frac{\gamma}{(\gamma-1)}} \tag{3.2}$$

where P_{ti} is the total pressure at the nozzle inlet, P_e is the static pressure at the nozzle exit, which is equal to the atmospheric pressure. M_e is the mach number at the exit of the nozzle, which is set to 0.7 and $\gamma = 1.4$ is the ratio of specific heats. The total pressure at the inlet is thus found to be 139743.685177 Pa. The flow at the inlet of the nozzle is uniform, with a Reynolds number of 28,584 and a turbulence intensity of 3.81%. The dynamic viscosity of air is set as $1.846 * 10^{(-5)} Pa - s$, the density of air is set as $1.1768 kg/m^3$, and the ideal gas law is used as the equation of state. The Favre filtered Navier Stokes equations are solved and the Dynamic Smagorinsky Model is used for modelling the sug-grid scale stress. The turbulent Prandtl number Pr_t is set as 0.9.

3.3.3 Boundary Conditions

The computational domain for the installed jet is split into 13 control surfaces to impose the boundary conditions as follows -

1) Nozzle inlet

2) Nozzle wall interior surface

3) Nozzle wall exterior surface

4) Domain inlet

5) Domain outlet (above plate)

6) Domain outlet (below plate)

7) Flat plate top surface

8) Flat plate bottom surface

9) Flat plate surface facing domain inlet

10) Domain far field right (considering positive streamwise direction)

11) Domain far field left (considering positive streamwise direction)

12) Domain far field top

13) Domain far field bottom

Figures 3.28 to 3.39 illustrate all these control surfaces in order.

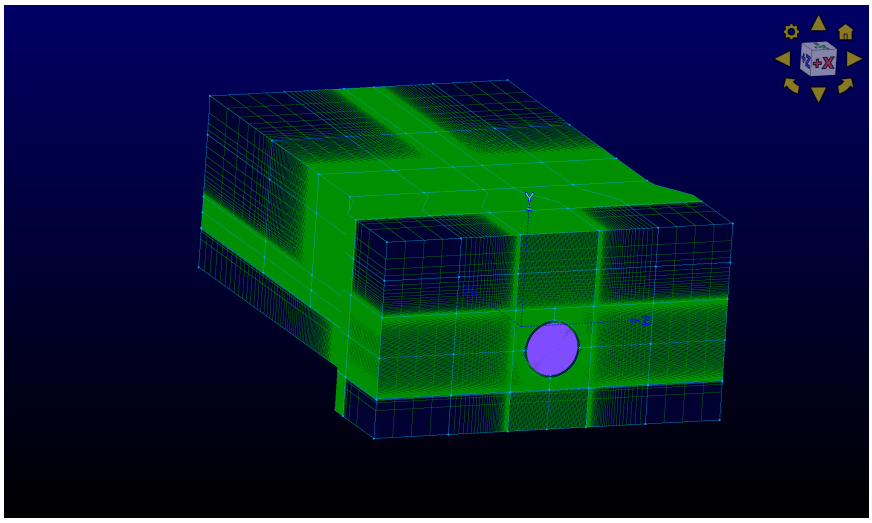

Figure 3.28: Nozzle Inlet, Highlighted by Purple

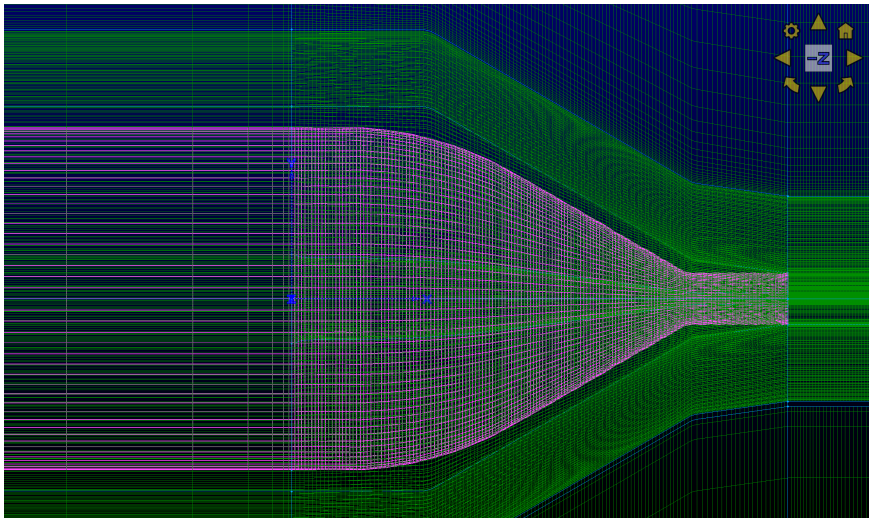

Figure 3.29: Nozzle Interior Wall, Highlighted by Pink

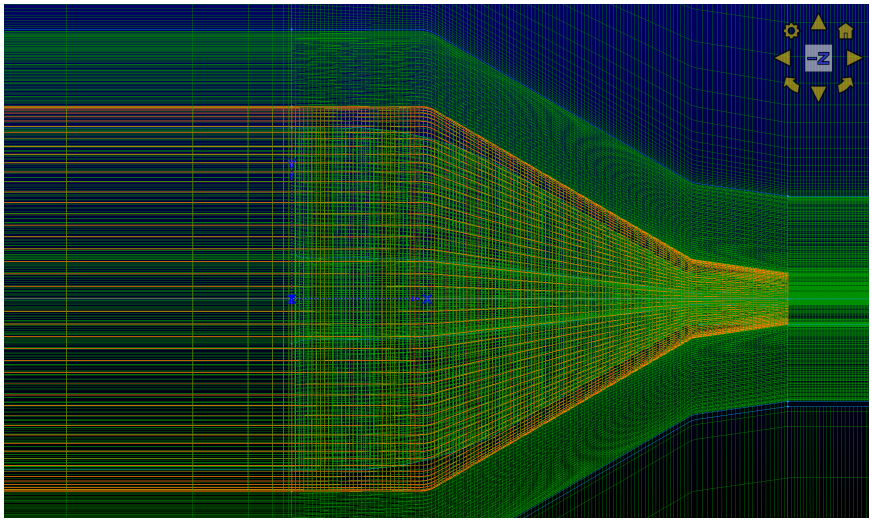

Figure 3.30: Nozzle Exterior Wall, Highlighted by Orange

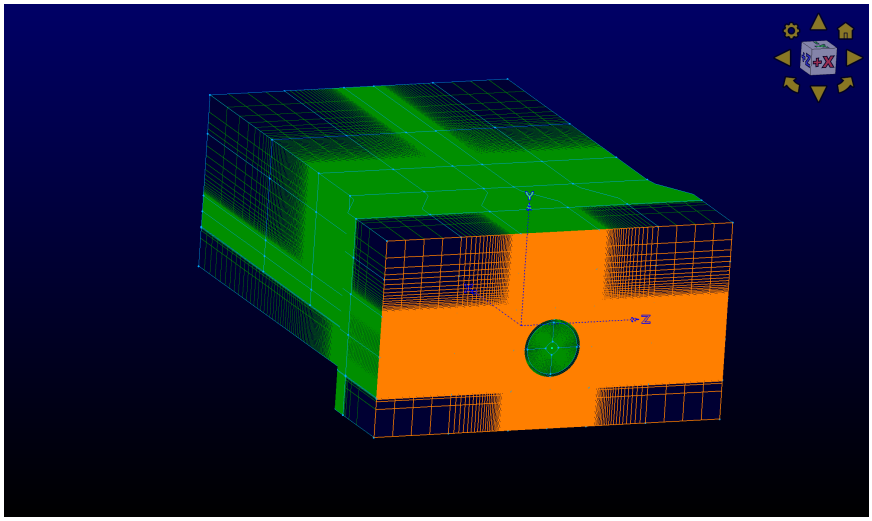

Figure 3.31: Domain Inlet, Highlighted by Orange

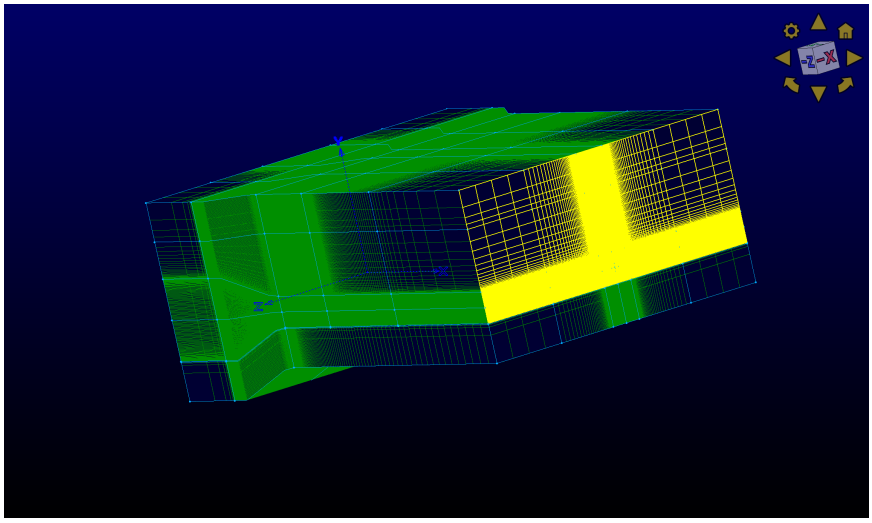

Figure 3.32: Domain Outlet (Above Plate) Highlighted by Yellow

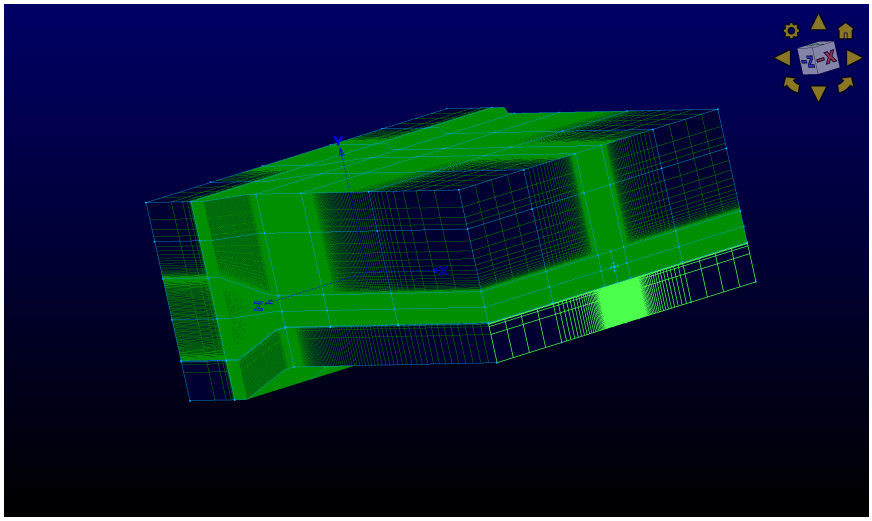

Figure 3.33: Domain Outlet (Below Plate) Highlighted by Bright Green

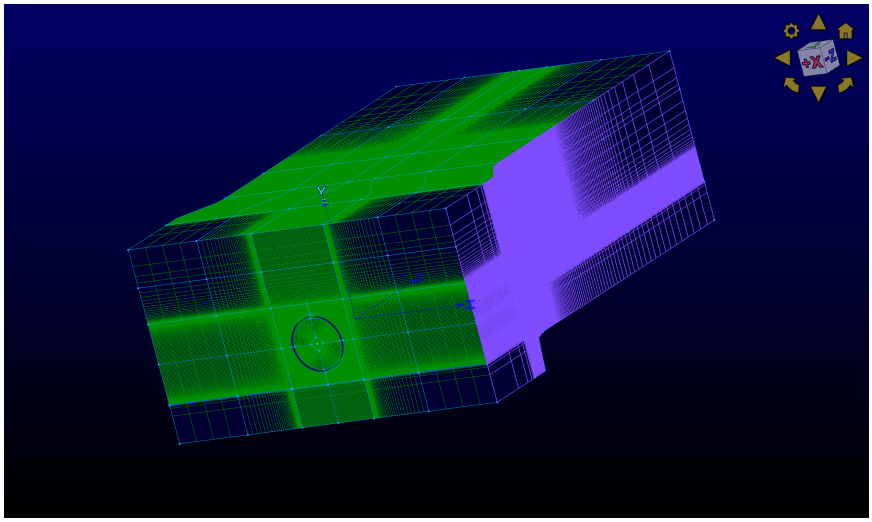

Figure 3.34: Domain Far Field Right, Highlighted by Purple

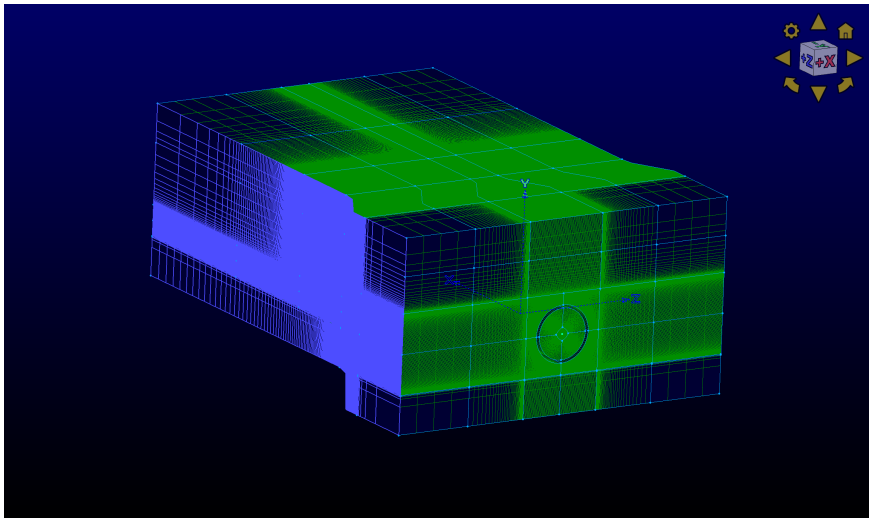

Figure 3.35: Domain Far Field Left, Highlighted by Purple

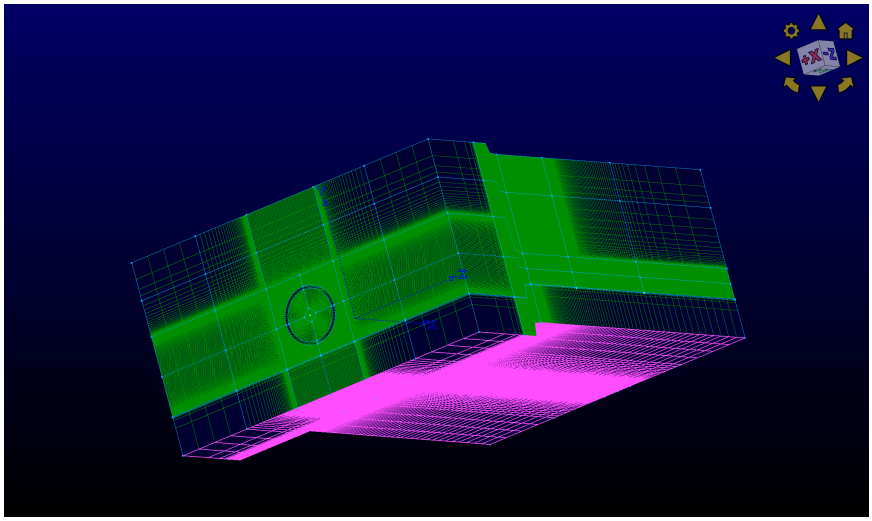

Figure 3.36: Domain Far Field Bottom, Highlighted by Pink

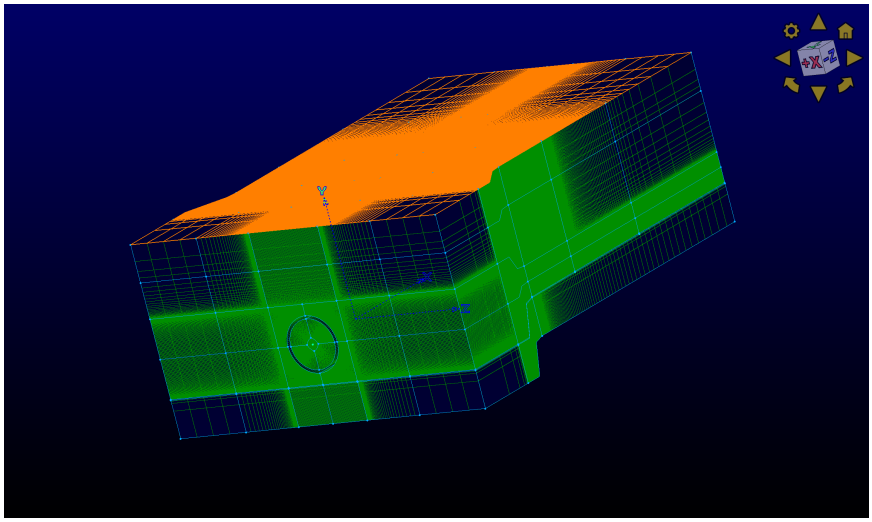

Figure 3.37: Domain Far Field Top, Highlighted by Orange

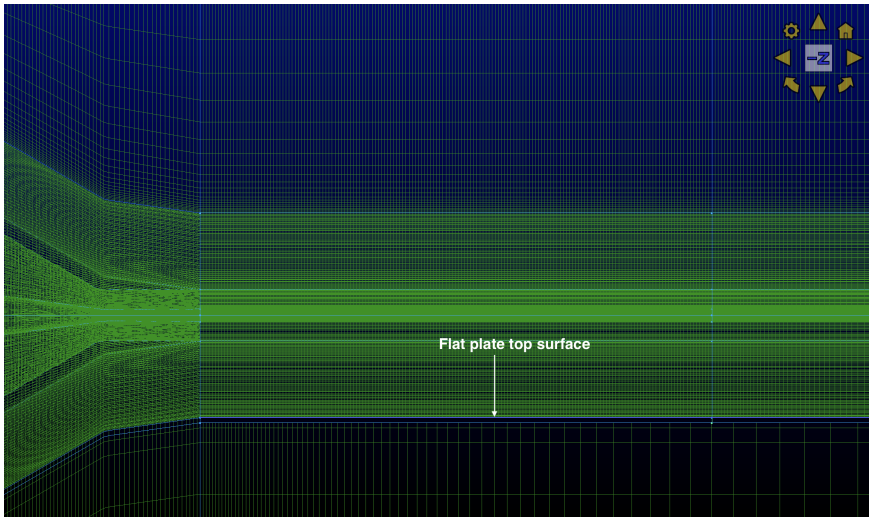

Figure 3.38: Flat Plate Top Surface

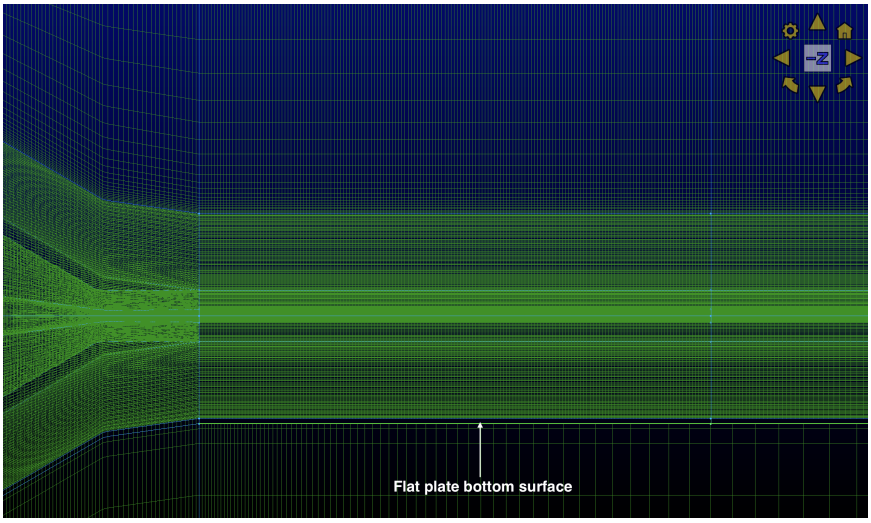

Figure 3.39: Flat Plate Bottom Surface

The domain inlet, outlet and farfield sides as given in table 3.9 are set with a total pressure and total temperature of 103344.43375 Pa and 300 K to model the ambient conditions as set in the experiment by Meloni *et al.* (2019). The total pressure and total temperature of 300 K at the nozzle inlet is set to 139743.685177 Pa as given in equation 3.2. The flat plate walls are modelled as adiabatic to prevent heat transfer across it surface.

Table 3.9: Boundary Conditions for Installed Jet Case With 15 Million Cells

Surface	Type	Total Pressure (Pa)	Total Temperature (K)
Nozzle Inlet	'Pressure Inlet'	139743.685177	300
Nozzle wall interior surface	Adiabatic wall		
Nozzle wall exterior surface	Adiabatic wall		
Domain inlet	'Pressure Inlet'	103344.43375	300
Domain outlet (above plate)	'Pressure Outlet'	103344.43375	300
Domain outlet (below plate)	'Pressure Outlet'	103344.43375	300
Flat plate top surface	'Adiabatic wall'		
Flat plate bottom surface	'Adiabatic wall'		
Domain far field right	'Pressure Inlet'	103344.43375	300
Domain far field left	'Pressure Inlet'	103344.43375	300
Domain far field top	'Pressure Inlet'	103344.43375	300
Domain far field bottom	'Pressure Inlet'	103344.43375	300

3.4 Installed Jet - 40 Million Cells

This case is a continuation of the installed jet case with 15 million cells, but the grid is refined to $\sim$ 40 million cells. The grid is refined in the boundary layer along the nozzle walls, along the plate surface and in the mixing layer region of the jet. As this is just a refinement of the previous simulation, the nozzle geometry, simulation physics and boundary conditions remain the same as the installed jet case with 15 million cells.

3.4.1 Grid Generation

The grid contains 587 x 496 x 128 points in the streamwise, radial and azimuthal directions. The coordinate origin of the entire domain is located at the center of the nozzle inlet. The entire set up including the dimensions of the domain remain the same as in section 3.3.1 and it is split into two components - physical domain and computational domain, with the same dimensions. A full schematic of the mesh is given in figure 3.40, 3.41 and a detailed breakdown of the mesh statistics is given in table 3.10 and table 3.11.

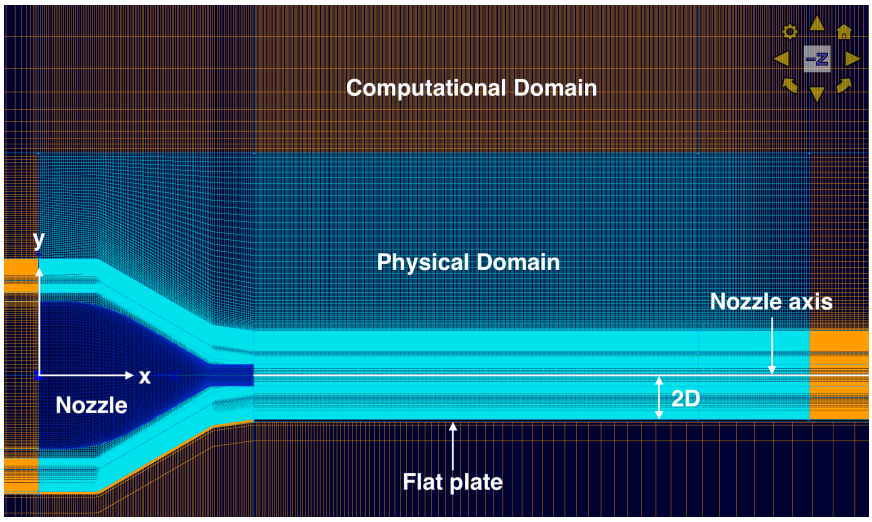

Figure 3.40: Computational Grid Schematics for Installed Jet Case With 40 Million Cells

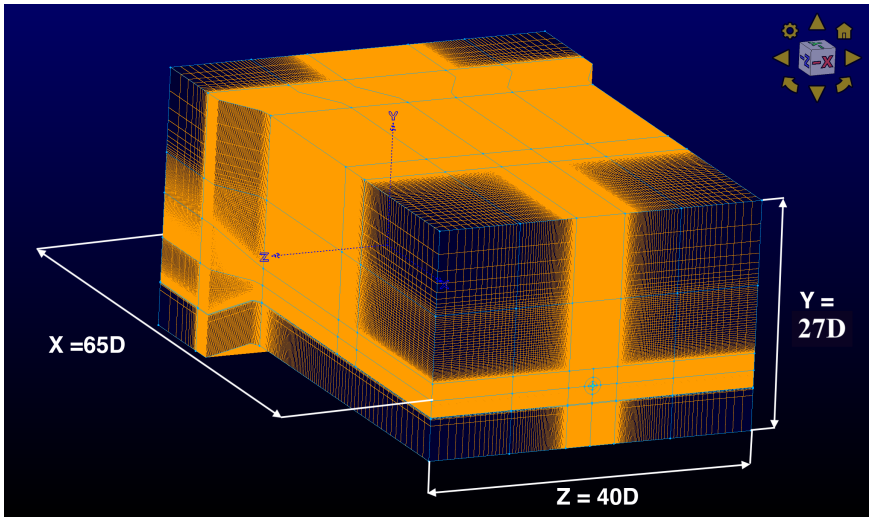

Figure 3.41: Computational Grid for Installed Jet Case With 40 Million Cells

Table 3.10: Mesh Specifications in Streamwise Direction for Installed Jet 40 Million Case

Region	Number of cells	Average Spacing (δ_x/D)
Physical Domain	29,974,408	
Computational Domain	9,746,312	
Total	39,720,720	
$9.5D < x < 35D, -2D < y < 2D, -3D < z < 3D$	13.9 million	0.058

The grid has 25 points in the boundary layer of the nozzle, i.e., a thickness of $\delta/D = 0.08$ along the nozzle wall, as compared to ~ 8 points in the boundary layer of the nozzle in the 15 million cell case. The grid is further refined in the region $9.5D < x < 35D, -2D < y < 2D, -3D < z < 3D$, i.e., in the flow field of the jet, by ~ 3 times the previous case, to increase the accuracy of predictions. To capture the development of the turbulent boundary layer along the plate surface, it is resolved by

20 points in the vertical (y) direction, for a thickness of $\delta/D = 0.1$ from the plate's top surface. Figure 3.42 depict a cross section of the grid showing the cell structure and distribution at the nozzle exit, and figure 3.43 shows the grid distribution in the region close to the nozzle exit (cut section at the mid-plane of the grid (z = 0)).

Table 3.11: Mesh Specifications in Spanwise Direction for Installed Jet 40 Million Case

Region	Average Spacing in y-direction(δ_y/D)	Average Spacing in z-direction(δ_z/D)
$-0.5D < y, z < 0.5D$	0.006	0.006
$0.5D < y, z < 1D$	0.02	0.02
$-2D < y < 2D, 1D < z < 3D$	0.0241	0.046
Boundary layer on top of plate	0.000436	0.046

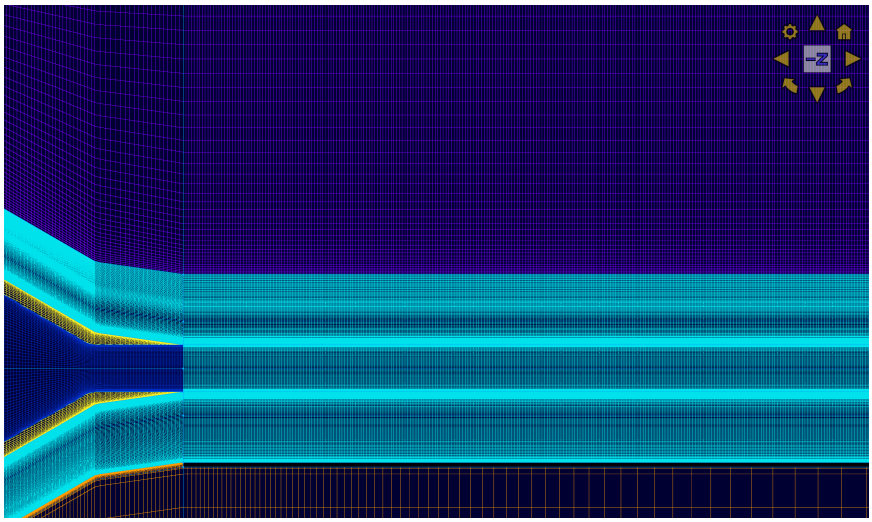

Figure 3.42: Cross Section of Domain Along Z = 0 Plane, Cyan Coloured Region Showing Grid Refinement at the Nozzle Exit

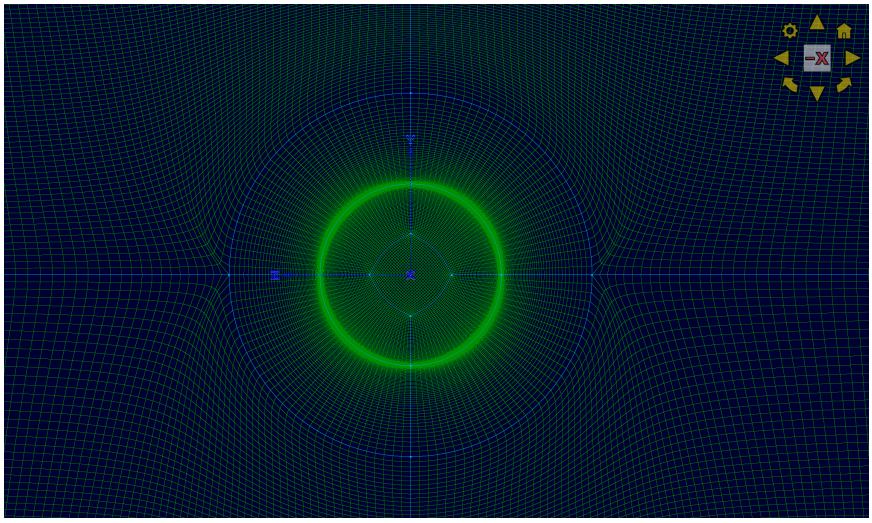

Figure 3.43: Cross Section of Domain Along X = 9.5d Plane, Zone Shows Grid Refinement in the Nozzle Boundary Layer and Nozzle Exit Region

3.4.2 Physics Set Up

As this case is just a refined grid version of the 15 million cell installed jet case, the physics set up remain exactly the same as in section 3.3.2.

3.4.3 Boundary Conditions

The boundary conditions also remain the same as in section 3.3.3, as the mesh structure and simulation case remains the same as the 15 million cells case. A summary of boundary conditions is given in table 3.12 and an illustration of these surfaces is given in figures 3.44 to 3.54.

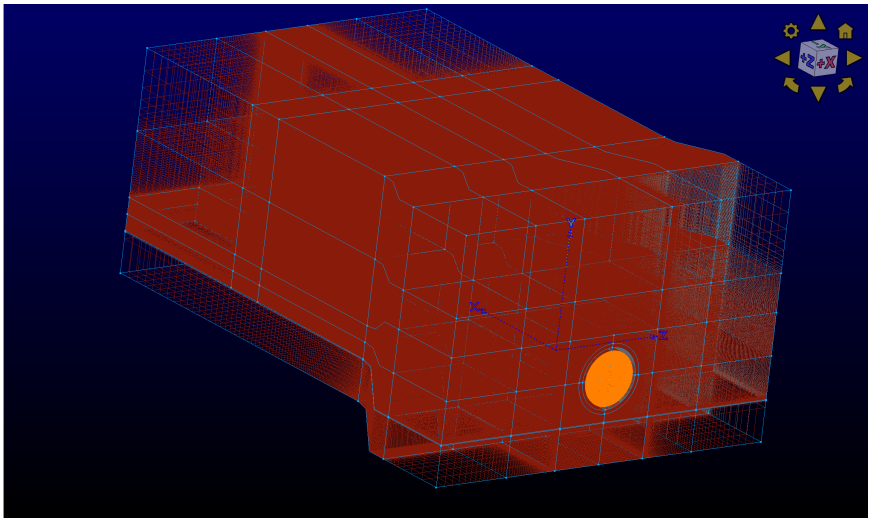

Figure 3.44: Nozzle Inlet, Highlighted by Orange

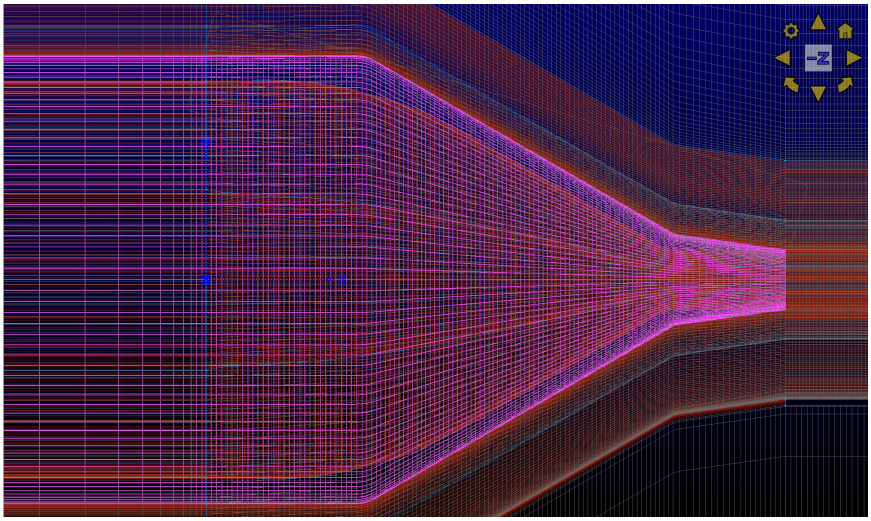

Figure 3.45: Nozzle Exterior Wall, Highlighted by Pink

Table 3.12: Boundary Conditions for Installed Jet Case With 40 Million Cells

Surface	Type	Total Pressure (Pa)	Total Temperature (K)
Nozzle Inlet	'Pressure Inlet'	139743.685177	300
Nozzle wall interior surface	Adiabatic wall		
Nozzle wall exterior surface	Adiabatic wall		
Domain inlet	'Pressure Inlet'	103344.43375	300
Domain outlet (above plate)	'Pressure Outlet'	103344.43375	300
Domain outlet (below plate)	'Pressure Outlet'	103344.43375	300
Flat plate top surface	'Adiabatic wall'		
Flat plate bottom surface	'Adiabatic wall'		
Flat plate front edge	'Adiabatic wall'		
Domain far field right	'Pressure Inlet'	103344.43375	300
Domain far field left	'Pressure Inlet'	103344.43375	300
Domain far field top	'Pressure Inlet'	103344.43375	300
Domain far field bottom	'Pressure Inlet'	103344.43375	300

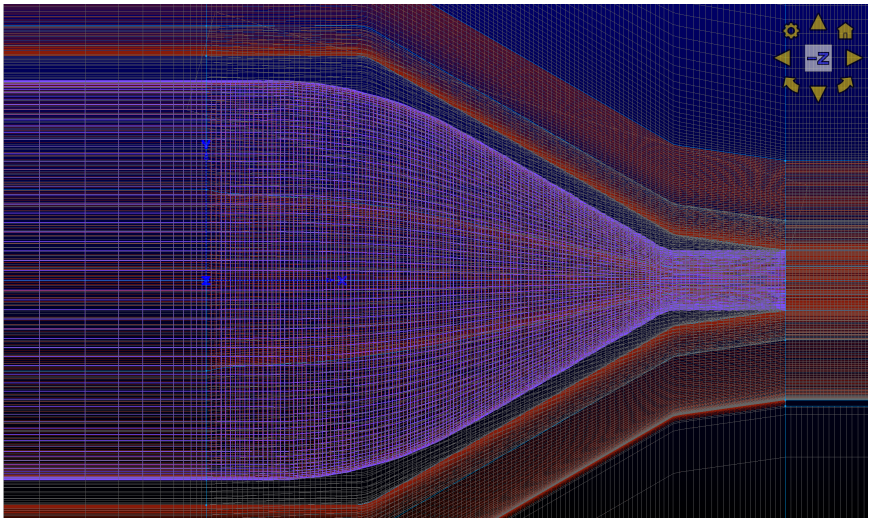

Figure 3.46: Nozzle Inlet Wall, Highlighted by Purple

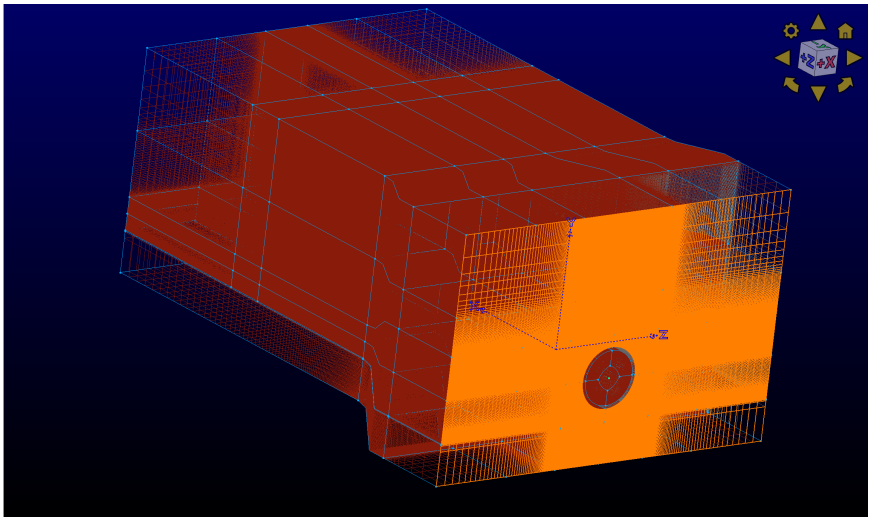

Figure 3.47: Domain Inlet, Highlighted by Orange

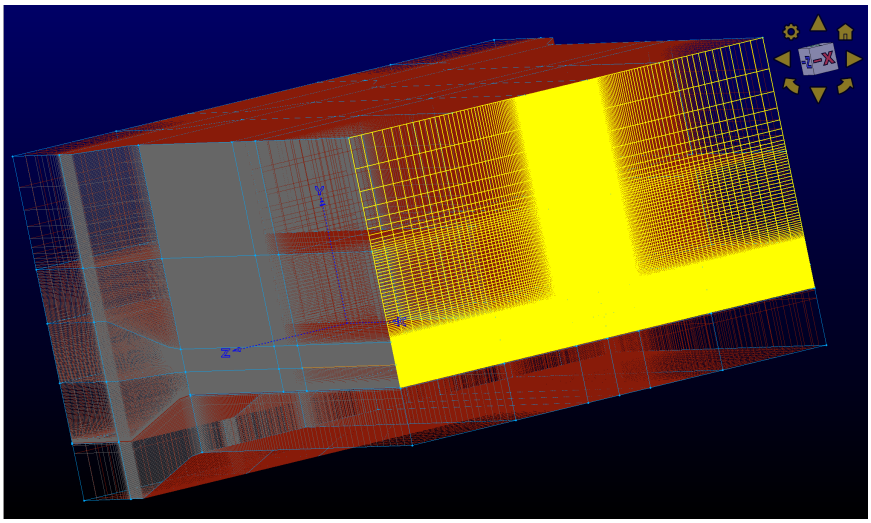

Figure 3.48: Domain Outlet (Above Plate) Highlighted by Yellow

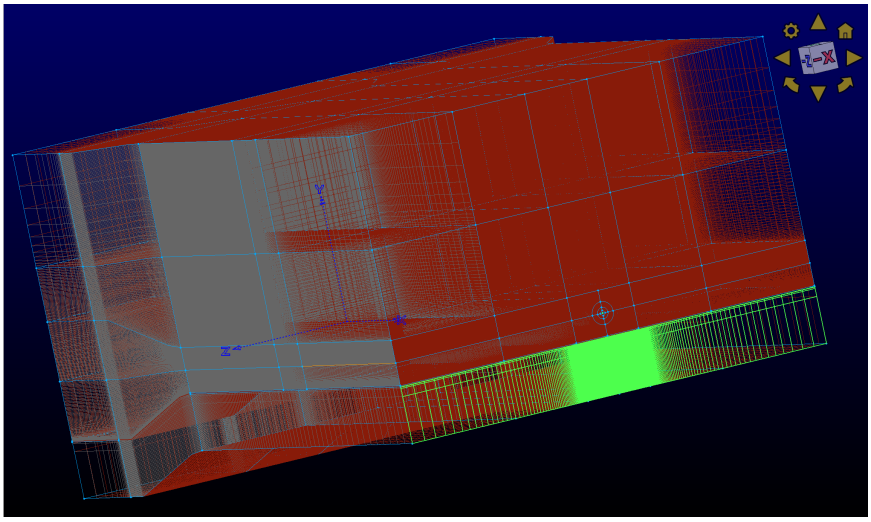

Figure 3.49: Domain Outlet (Below Plate) Highlighted by Bright Green

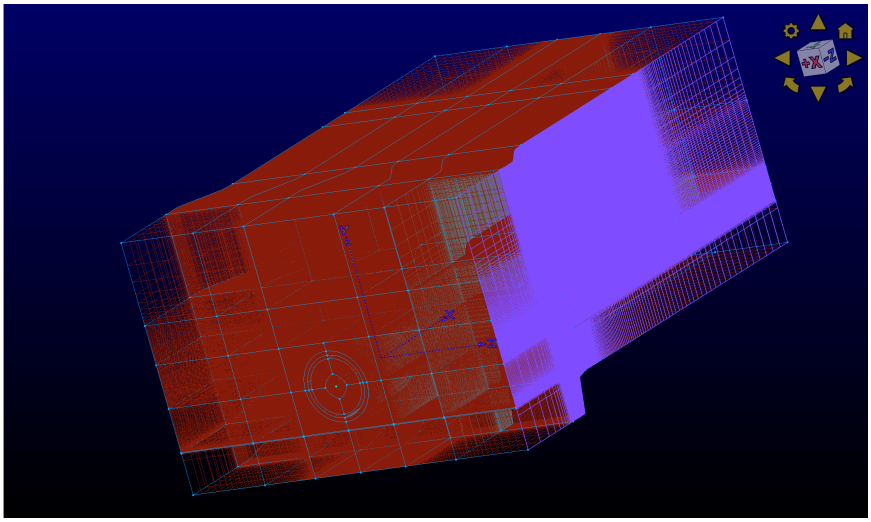

Figure 3.50: Domain Far Field Right, Highlighted by Purple

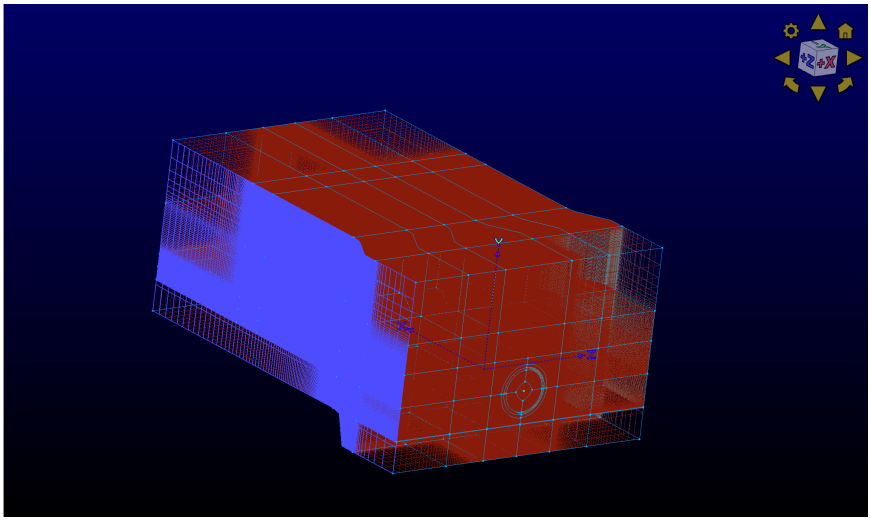

Figure 3.51: Domain Far Field Left, Highlighted by Purple

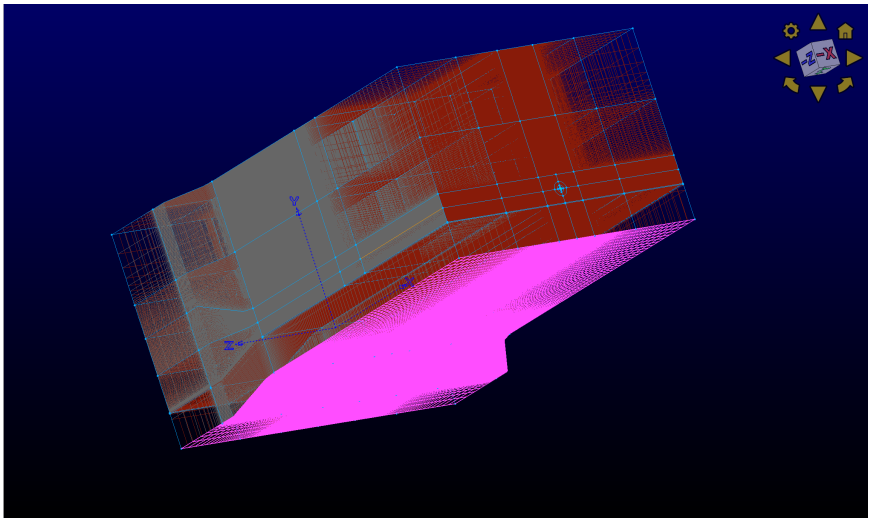

Figure 3.52: Domain Far Field Bottom, Highlighted by Pink

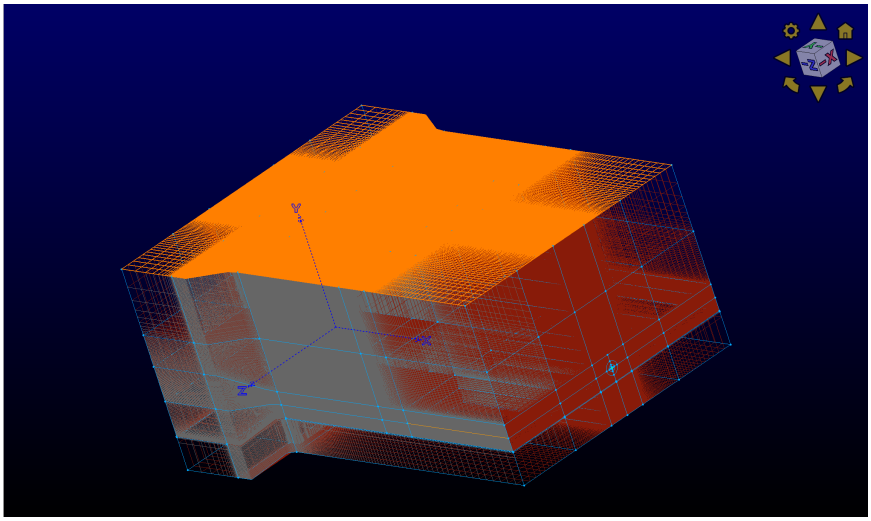

Figure 3.53: Domain Far Field Top, Highlighted by Orange

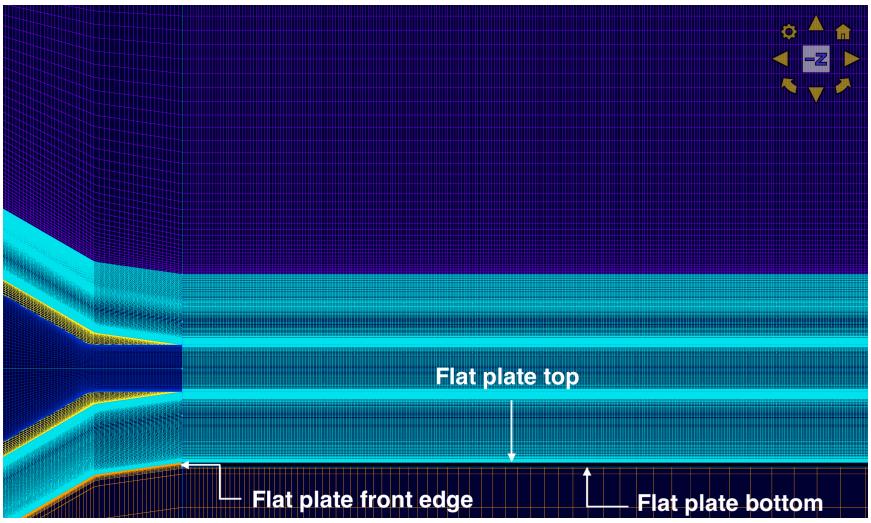

Figure 3.54: Flat Plate Boundary Surfaces

Chapter 4

RESULTS AND DISCUSSION

The primary purpose of this research is to validate the jet simulations with laboratory experiments of the same cases, to check the feasibility of using Large Eddy Simulation as an analysis tool for noise prediction and flow characterisation of a high-speed jet. Once the simulation results are validated with sufficient confidence, they can be used for further analysis of the flow field of a jet, as a CFD simulation provides more spatially resolved data than an experiment. However, the major drawback of a simulation is that it has poor temporal resolution - a high fidelity simulation (such as LES) has a very small time step (of the order of 10^{-7} to 10^{-9} seconds) to maintain numerical stability, and therefore requires a long time to reach statistically stationary state, after which accurate results will be produced (can range from 1 week to a couple of months, depending on computational resources). Thus, simulation time for a jet simulation is measured in terms of flow through times - the time required by the jet to cross the computational domain, i.e., from the nozzle exit to the domain outlet. The simulation is assumed to be complete or "converged" when the flow quantities attain a stable or a statistically stationary state (mean remains constant over time) over sufficient number of flow through times. Typically, for jet simulations, this is understood to be in the range of 10-20 flow through times, after which, the results can be used for validation with experiment data with high confidence.

Therefore, all the jet-simulation cases in this research are simulated for at least 10 flow through times with the exception of the 37 million cells installed jet case, because of a shortage of time. All the simulations are run on Arizona State University's supercomputer - Agave utilizing its large parallel computing capability. Due to the

large number of cells involved in the computational grids of each simulation case, the size of data generated by each simulation run is quite large, ranging from 1 gigabyte to 15 gigabytes. Therefore, post-processing of data is carried out by using a combination of Tecplot 360 and post-processing scripts written on MATLAB. The results of each case will be discussed in the subsequent sections.

4.1 Freejet - 8 Million Cells

The freejet simulations will be validated using corresponding freejet experiment data from Mancinelli and Camussi (2018). The freejet case described in section 3.1 is simulated for 10 flow through times using a time step of $1.1 * 10^{-8}s$ at a Courant Friedrich-Levy (CFL) number of ~ 0.95 throughout the run. The time step can be expressed in dimensionless form by multiplying and dividing by the jet velocity at the nozzle exit and nozzle exit diameter; it is obtained as $\Delta t_{nd} = 0.000108$. As mentioned above, the jet simulation time is measured in terms of the number of times the jet crosses the computational domain, called the flow through time (FTT), and it is calculated as follows -

$$1 \text{ FTT} = \frac{\Delta x_{dom}}{(U_j * \Delta_t)} \tag{4.1}$$

where, Δx_{dom} is the length of the domain from the nozzle exit to the domain exit, U_j is the velocity of the jet at the nozzle exit, and Δ_t is the time step used for the simulation. Based on the simulation set-up, these values are as follows -

$$\Delta x_{dom} = 0.54m,\ U_j = 120m/s,\ \Delta_t = 1.1 * 10^{-8} \text{ s}$$

$$\text{Therefore, 1 FTT} \quad 400{,}000 \text{ iterations}$$

The simulation was run for 4,250,000 iterations, corresponding to a flow through time of ~ 10, and it took ~ 2.5 months for the simulation to complete. We can observe the statistically stationary state of the mean of flow velocity in figures 4.1 to 4.3. The

time averaged velocity of the jet at various locations along the nozzle axis is plotted as a function flow through time.

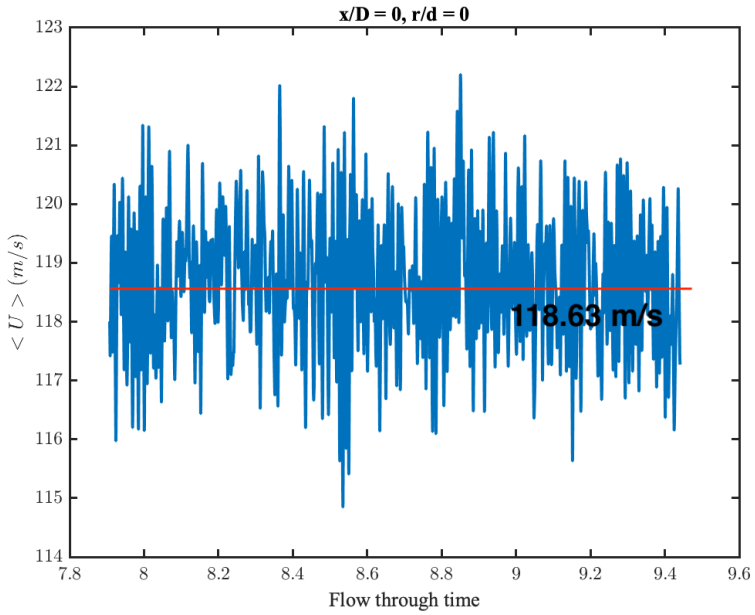

Figure 4.1: Variation of Time Averaged Velocity as a Function of FTT at $x/D = 0$, I.E. at Nozzle Exit

However, at axial locations further downstream of the exit, i.e. at x/D = 15, 20 & 25 (end of physical domain), the solution shows a higher fluctuation about the mean because of coarse grid resolution in that region. This can be seen in figures 4.4 to 4.6. Please note that all the distances mentioned in the figures are measured from nozzle exit ($x/D = 0$).

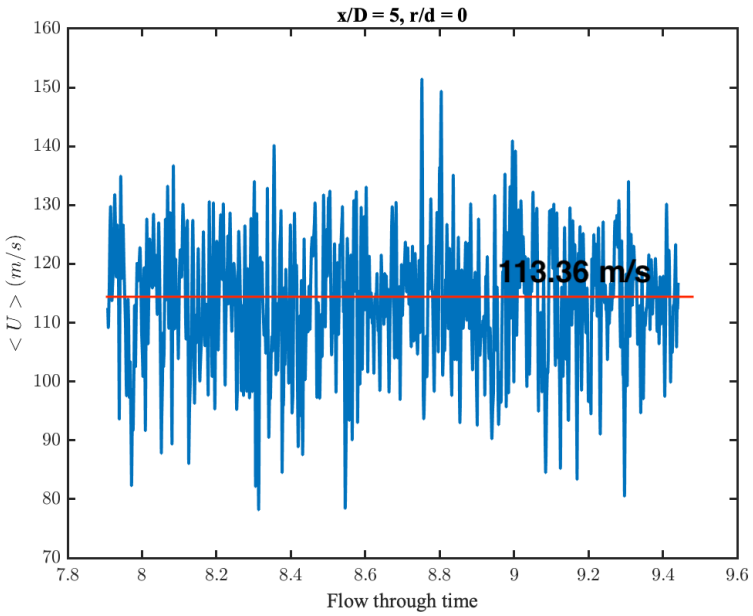

Figure 4.2: Variation of Time Averaged Velocity as a Function of FTT at $x/D = 5$

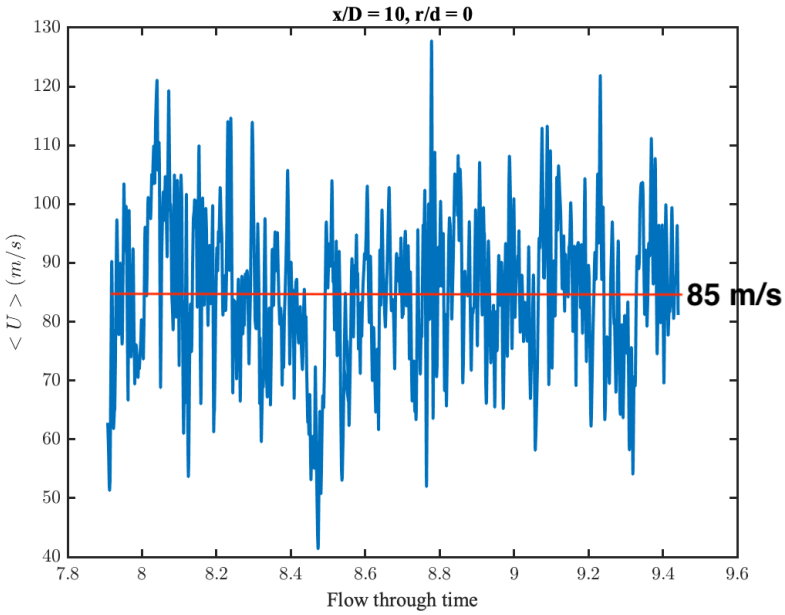

Figure 4.3: Variation of Time Averaged Velocity as a Function of FTT at $x/D = 10$

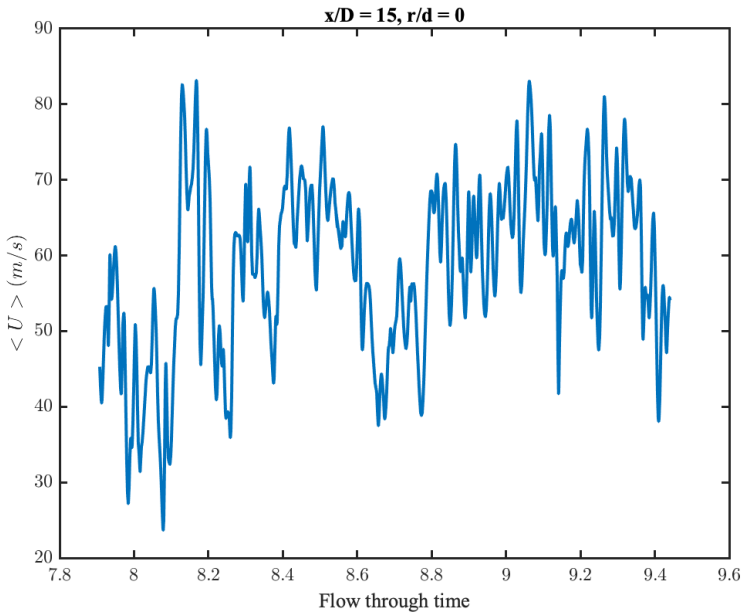

Figure 4.4: Variation of Time Averaged Velocity as a Function of FTT At $x/D = 15$

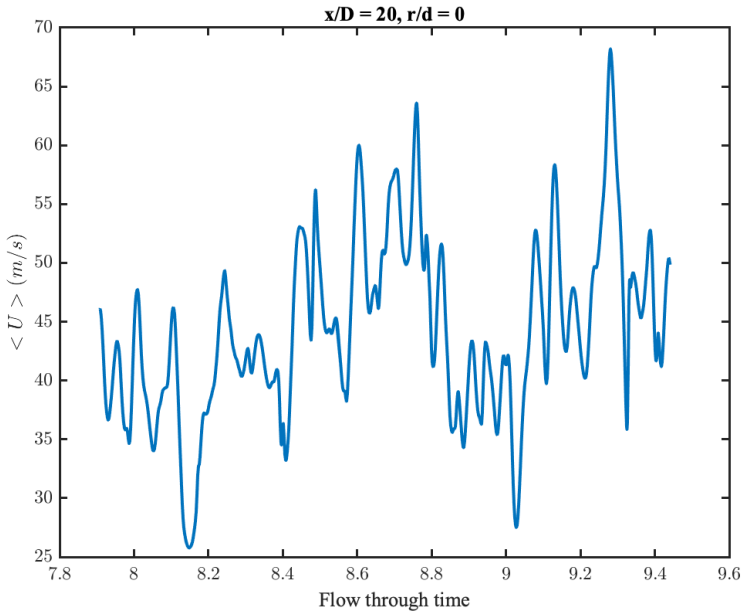

Figure 4.5: Variation of Time Averaged Velocity as a Function of FTT At $x/D = 20$

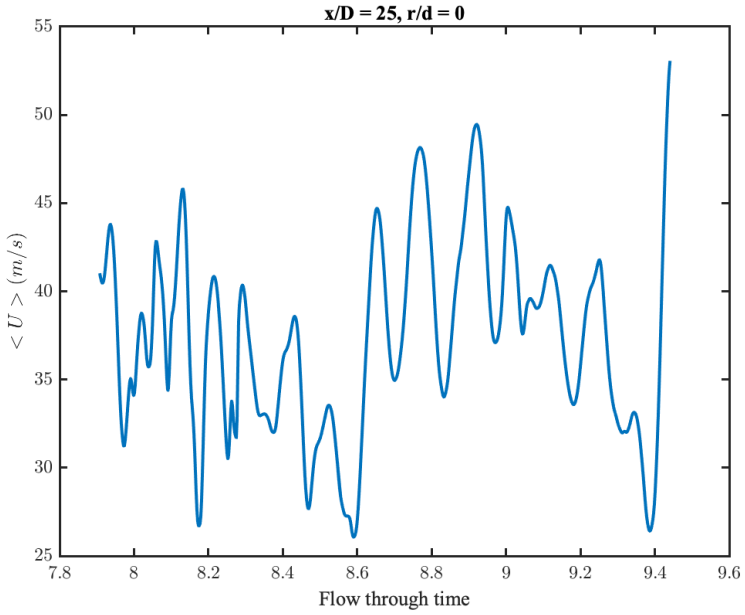

Figure 4.6: Variation of Time Averaged Velocity as a Function of FTT At $x/D = 25$

Once a stationary statistical mean has been established, low order statistics of the flow can be calculated. Figures 4.7 and 4.8 show a contour plot of the mach number and velocity of the jet (at z = 0 plane) as it flows through the computational domain, and a mach number of 0.35 can be observed at the nozzle exit.

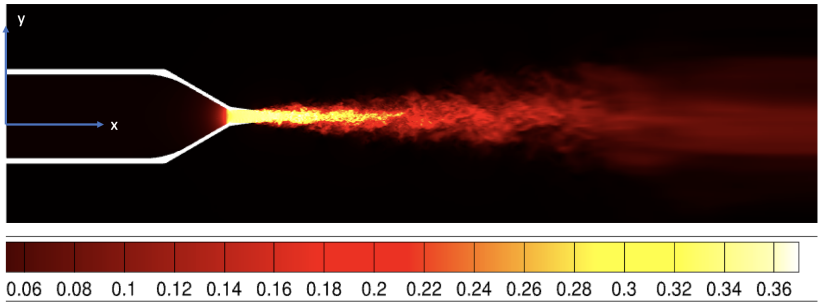

Figure 4.7: Contour Plot of Jet Mach Number at $z = 0$ Plane

Figure 4.9 shows the contour plot of the jet temperature as it flows through the domain. Since we are dealing with an unheated stream of air, it has a temperature of 300 K at the nozzle inlet (equal to the ambient temperature in the domain), it cools

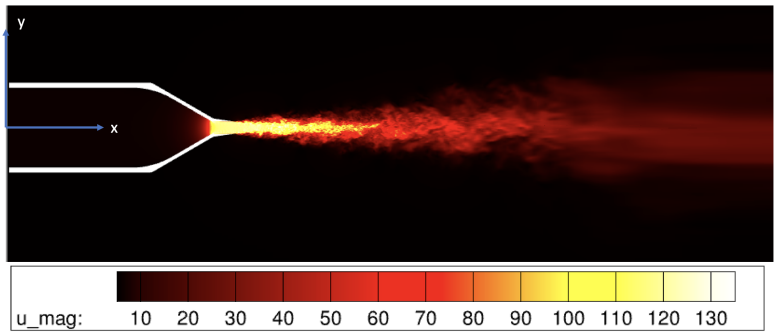

Figure 4.8: Contour Plot of Jet Velocity (in m/s) at $z = 0$ Plane

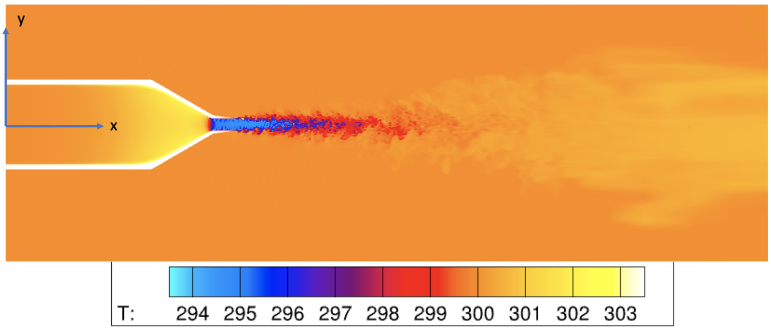

Figure 4.9: Contour Plot of Jet Temperature (in K) at $z = 0$ Plane

down as it exits the nozzle and recovers to the ambient temperature of 300 K far downstream. This is caused by the conversion of thermal energy to kinetic energy as the flow is accelerated by the nozzle and therefore this temperature gradient between the colder jet and the hotter ambient air aids in the mixing of the two streams of flow.

The streamwise evolution of axial velocity of the jet was measured by placing a line probe along the nozzle axis (y = 0, z = 0). The mean velocity of the jet normalized by it's velocity at the nozzle exit (exhaust velocity) was compared against the experiment results (Mancinelli and Camussi (2018)) and shows an encouraging agreement. In figure 4.10, the blue line indicates mean velocity predicted by the simulation and the black circles indicate the mean velocity as measured in the experiment. $< U >$ refers

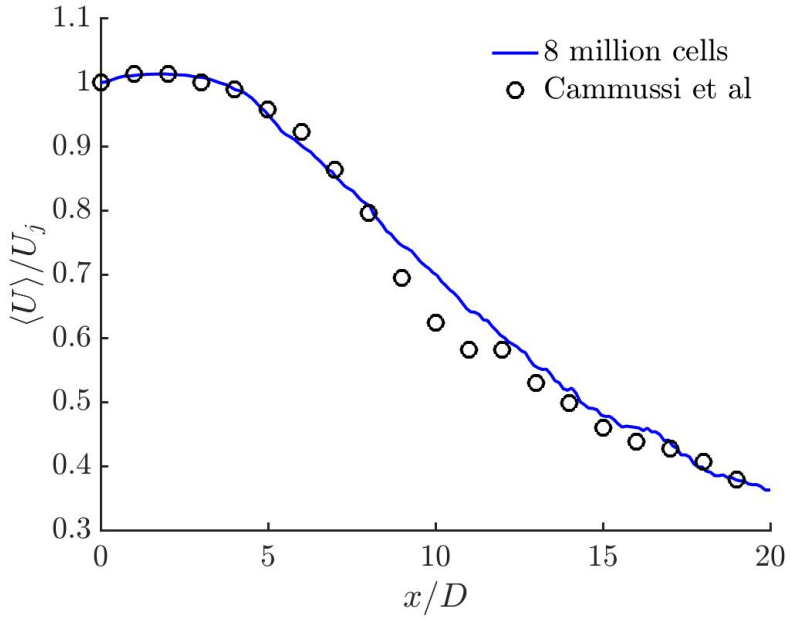

Figure 4.10: Mean Velocity of Jet Along Nozzle Axis

to the mean velocity and U_j indicates the velocity at the nozzle exit.

The variation of turbulence intensity of the jet along the nozzle axis was calculated by dividing the root mean square of velocity fluctuations ($\langle u'^2 \rangle^{(1/2)}$) by the jet exhaust velocity (U_j).

It can be observed from figure 4.10 that the mean velocity remains ~ 1 up to x/D = 5 and then decays rapidly further downstream. This axial distance marks the end of the potential core of the jet, and this can also be observed in figure 4.11 where the turbulence intensity remains low till an axial distance of x/D = 4, then starts to increase rapidly downstream. The turbulence intensity predicted by the simulation is higher than that of the experiment after x/D = 4, because the grid is not refined enough to capture the smallest scales of turbulence.

The spanwise variation of axial velocity ($\langle U \rangle / U_j$) and turbulence intensity ($\langle u'^2 \rangle^{(1/2)} / U_m$) at various axial locations is shown in figures 4.12 and 4.13. The solid lines indicate results predicted by the simulation and the solid markers indicate the

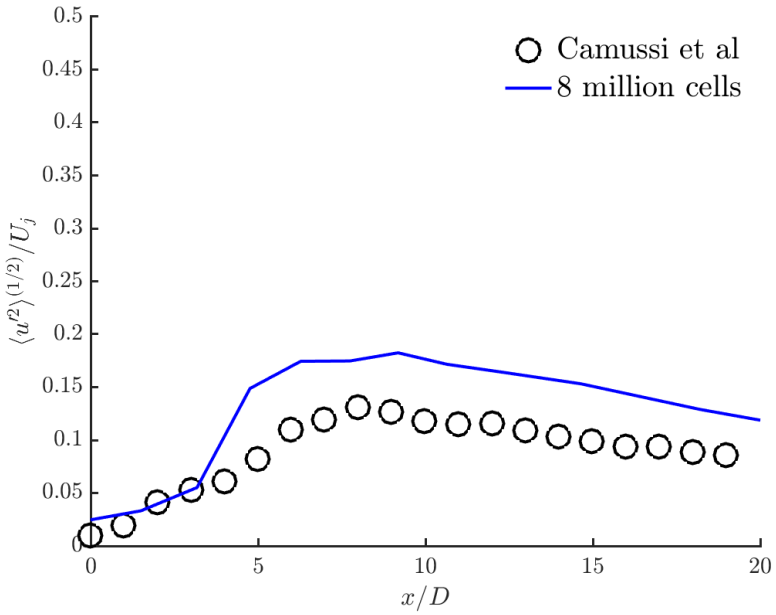

Figure 4.11: Turbulence Intensity of Jet Along Nozzle Axis

experiment results (Mancinelli and Camussi (2018)). Figure 4.12 shows an encouraging correlation of the spanwise velocity with the experiment results, however at axial distances greater than x/D $\sim$ 14, the correlation is poor along the radial direction, which indicates that a higher grid resolution is required in that direction. This is further reinforced by the trend of spanwise variation of turbulence intensity (T.I.) with axial distance, where the T.I. predicted by the simulation is much higher than that of the experiment at $-5 < z/D < 5$.

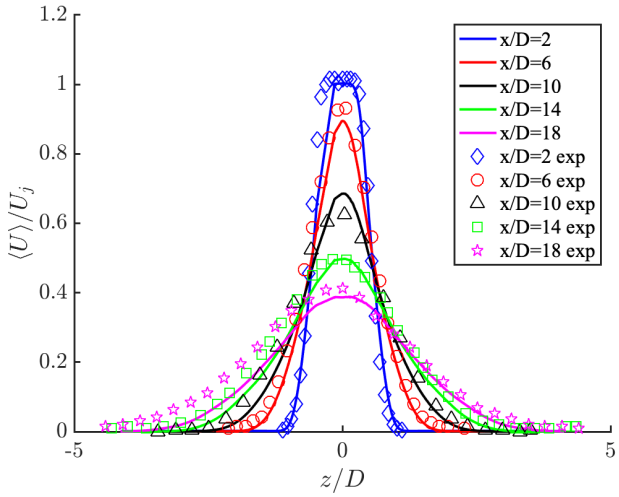

Figure 4.12: Spanwise Variation of Mean Velocity at Various Axial Distances

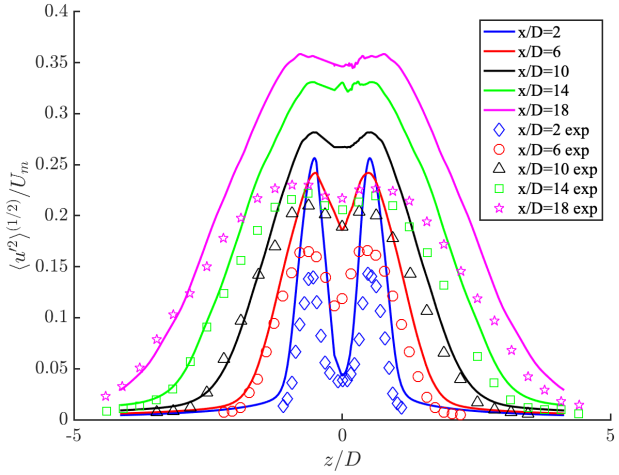

Figure 4.13: Spanwise Variation of Turbulence Intensity at Various Axial Distances

What is encouraging is that the mean velocity profiles exhibit a top hat shape within the potential core region (i.e, at $x/D < 5$ from the nozzle exit) and form a Gaussian-like shape outside the potential core of the jet (at axial distance $x/D > 6$ from the nozzle exit), i.e., in the developed region of the jet. The turbulence intensity plot also assumes a canonical shape, where the T.I. is relatively low inside the potential core and increases in the mixing zone and fully developed region of the jet, after which it slows down and dissipates into the ambient fluid. This behaviour is typical of jet

flows, and the poor correlation with experiment results at far downstream locations can be improved with refining the grid further in those regions.

Figures 4.14 to 4.18 show the characterization of the flow velocity along the nozzle axis in terms of Power Spectral Density, plotted against the Strouhal number based on the nozzle exit diameter and the nozzle exhaust velocity. The power spectral density is calculated at 5 axial positions, i.e., at x/D = 3, 7, 11, 15 and 19 (measured from the nozzle exit); corresponding to the experiment measurements at these locations. The Power Spectral Density (PSD) is normalized by dividing it by the nozzle exhaust velocity (U_j) multiplied by nozzle exit diameter (D) and the Strouhal number is calculated as -

$$St_D = \frac{(f * D)}{U_j} \tag{4.2}$$

where St_D is the Strouhal number based on the nozzle exit diameter and f is the vector of frequencies obtained by using Welch's method on the velocity time signal. A brief overview of Welch's method implemented on MATLAB using the pwelch() function is as follows -

1) A given time series is split into N number of overlapping windows or segments

2) Each segment is multiplied by a window function (for example, Hamming , Hanning , Rectangular function, etc.)

3) A Fast Fourier Transform (FFT) of each segment is calculated to get the Power Spectral Density

4) The Power Spectral Density is averaged over all the windows to get an estimate of the PSD of the signal.

The velocity along nozzle axis is measured at the axial positions as stated above at a Strouhal number of 900, for a sampling time of 1.5 flow through time, corresponding to 0.038 seconds in real time. In comparison, the velocity signal in the experiment was sampled at a Strouhal number of 10 for a sampling time of 10 seconds. The PSD

of the velocity time series is then calculated using pwelch() function on MATLAB, using 10 windows with 50% overlap and a Hanning window function.

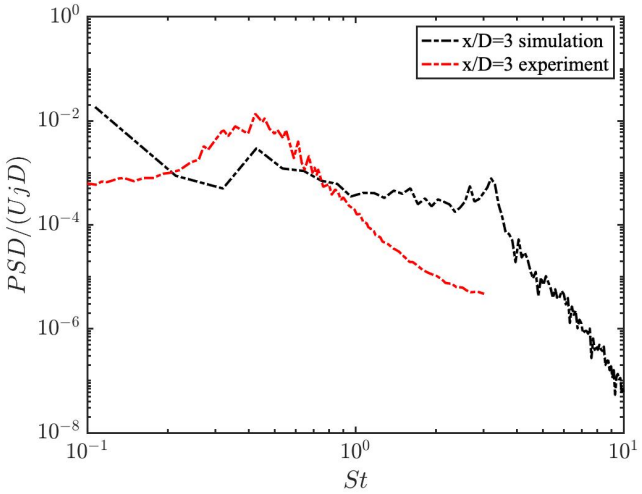

Figure 4.14: Velocity PSD at $x/D = 3$

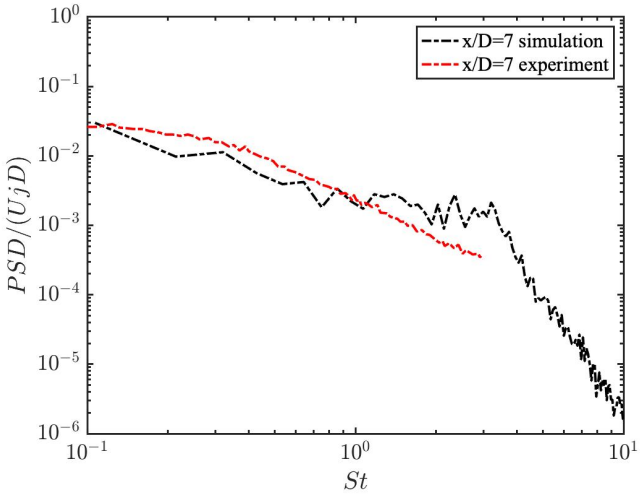

Figure 4.15: Velocity PSD at $x/D = 7$

Considering the relatively coarse resolution of the grid, we get encouraging correlations with the experiment at Strouhal numbers in the range of 0.1 - 1, corresponding to lower frequencies of the signal, at all axial distances given in figures 4.14 to 4.18. At strouhal numbers greater than 1, the correlation with experiment results is poor,

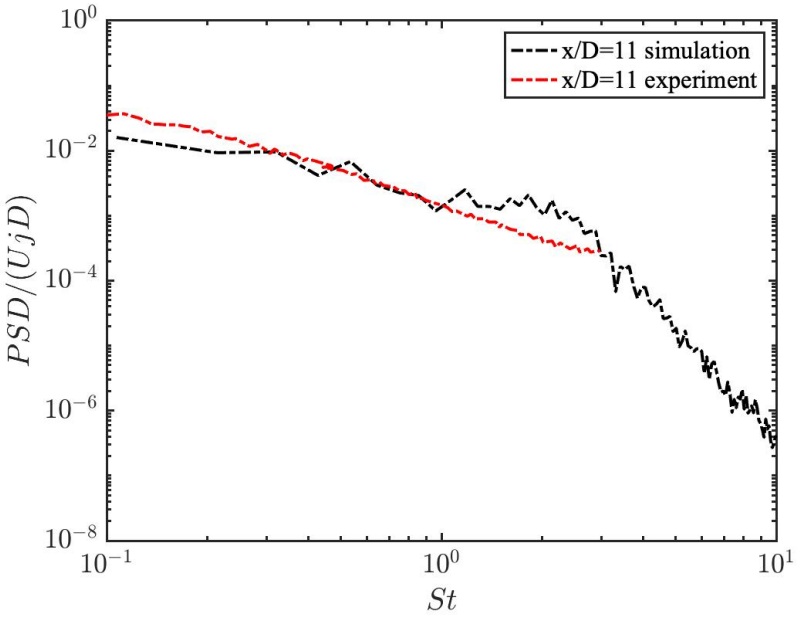

Figure 4.16: Velocity PSD at $x/D = 11$

partly because of the shorter sampling time and higher sampling frequency than the experiment, and also because of coarse grid resolution in the radial and azimuthal directions. A good agreement at lower Strouhal numbers can be attributed to the LES model itself, as the lower Strouhal numbers correspond to larger eddy sizes, and the LES code is built to resolve larger scales of flow accurately. Therefore, the simulation can resolve larger scales of flow accurately but cannot resolve the smaller scales or sub-grid scales of flow accurately as they are modelled. In order to accurately predict the smaller scales of flow and get better correlation of velocity spectra, the grid must be further refined in the radial and azimuthal directions as these majorly contribute to the generation of small scale structures in a turbulent jet.

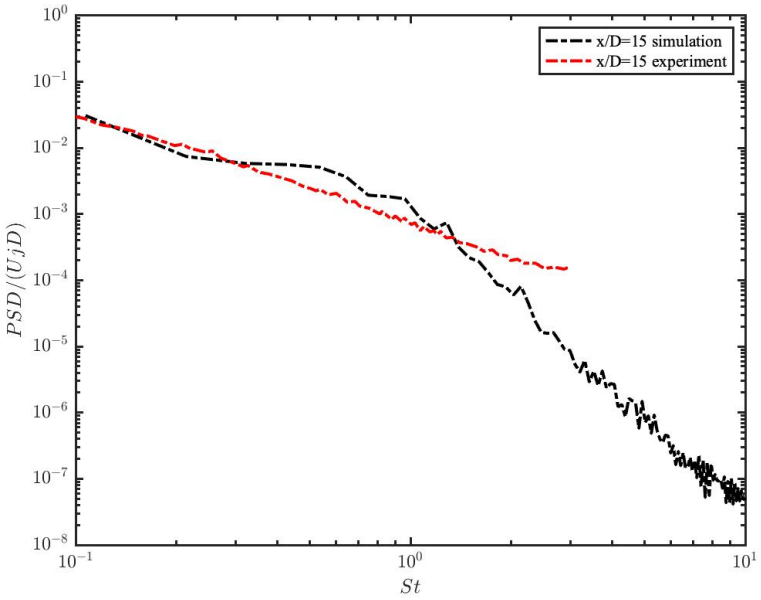

Figure 4.17: Velocity PSD at $x/D = 15$

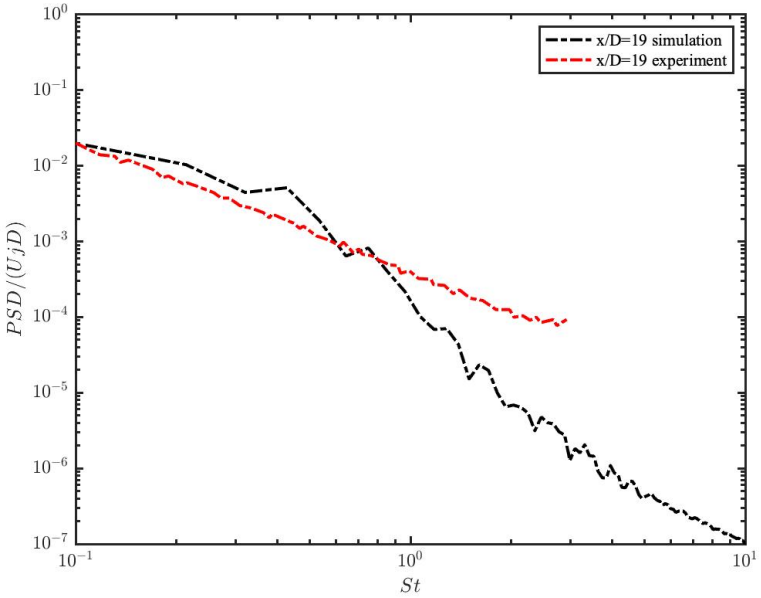

Figure 4.18: Velocity PSD at $x/D = 19$

At small axial distances, i.e., within the potential core (x/D = 3, figure 4.14), we can observe a bump in the velocity PSD at a St $\sim$ 0.4, which represents the jet column mode frequency. A bump at higher Strouhal number, corresponding to St $\sim$ 4 can be observed at axial distances x/D = 3 to 11 (figures 4.14 to 4.16), due to presence of high frequency components, which can be attributed to the coarse nature of the mesh. Figure 4.19 shows the velocity spectra at the above axial points, and at axial distances greater than x/D = 10, the spectra roughly follow Kolmogorov's -5/3 energy decay law, however, at $x/D = 19$, the dissipation of energy is faster than the Universal decay. This is caused by the stretching of the grid at large axial distances, which causes a faster dissipation of energy than the universal decay law. Refining the grid in these regions can lead to a better resolution of the small scales of turbulence present in the inertial subrange, that is present at these large axial distances.

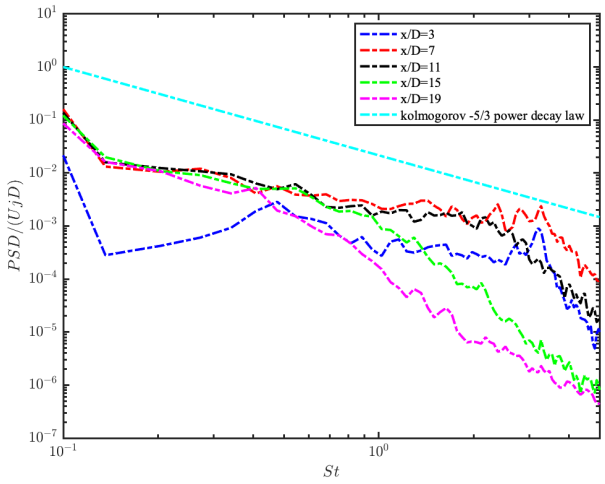

Figure 4.19: Velocity Spectra of Simulation Results at Various Axial Distances

4.1.1 Lipline Statistics

The mean velocity, static pressure and static temperature are measured along the nozzle lipline using 200 probe points at $x/D = 0$ to $x/D = 25$ (measured from

the nozzle exit), $r/D = 0.5$ (i.e, nozzle exit wall or nozzle lipline). Figures 4.20 show the variation of mean velocity, static pressure and static temperature along the lipline. These statistics are calculated by taking a time average of the probe signal, measured at a sampling frequency of 900 St_D (where St_D is the exit diameter based Strouhal number) and a sampling time of 1.5 FTT. A sharp increase in velocity can be observed as the jet leaves the nozzle exit at x/D = 0, which is mixing of the slow moving boundary layer with the high speed jet adjacent to it. Consequently, there is a sharp decrease of pressure at the nozzle exit as per the conservation of linear momentum, and it slowly recovers to the static pressure in the ambient fluid as the jet slows down further. Also, a sharp temperature gradient can also be observed at the nozzle exit, caused by this sudden decrease of velocity, after which it mixes with the ambient fluid and recovers to a value of $300K$.

Figures 4.21 shows the time varying velocity signal, plotted against the flow through time. A statistically stationary mean at various axial positions can be observed, thus further promoting the analysis as performed in this study.

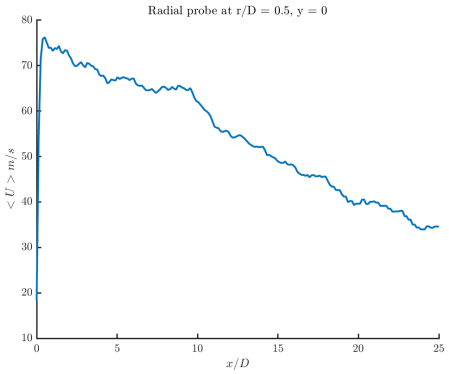

(a) Variation of Mean Velocity

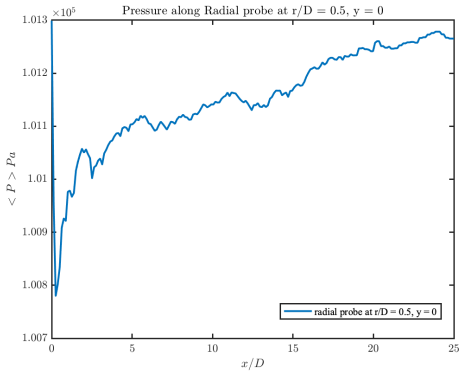

(b) Variation of Time Averaged Pressure

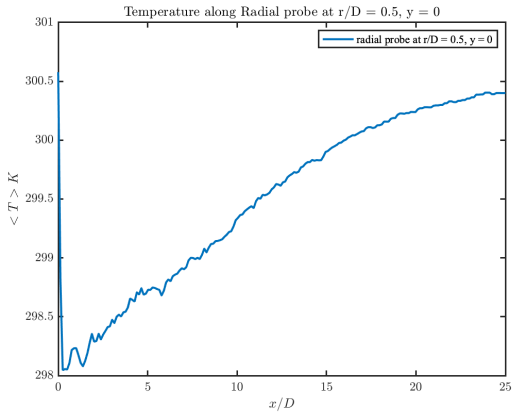

(c) Variation of Time Averaged Temperature

Figure 4.20: Variation of Statistics Along Nozzle Lipline

The two point statistics are also computed for this case, to check the cross correlation between two consecutive probe points. The cross correlation is calculated by measuring the time varying velocity field using probes located along the nozzle lipline (x/D = 0 to x/D = 25 - measured from the nozzle exit, r/D = 0.5), with each probe point separated by a distance of $1D$, where D is the nozzle exit diameter. The cross correlation function is given as follows -

$$R_{u_{i+1},u_i}(\zeta,\tau) = (u(x+\zeta,t+\tau),u(x,t)) \tag{4.3}$$

where $\zeta = 1D = 12mm$ is the separation between two consecutive probe points, τ is the time lag between two consecutive sensors and $R_{u_{i+1},u_i}(\zeta,\tau)$ is the cross correlation

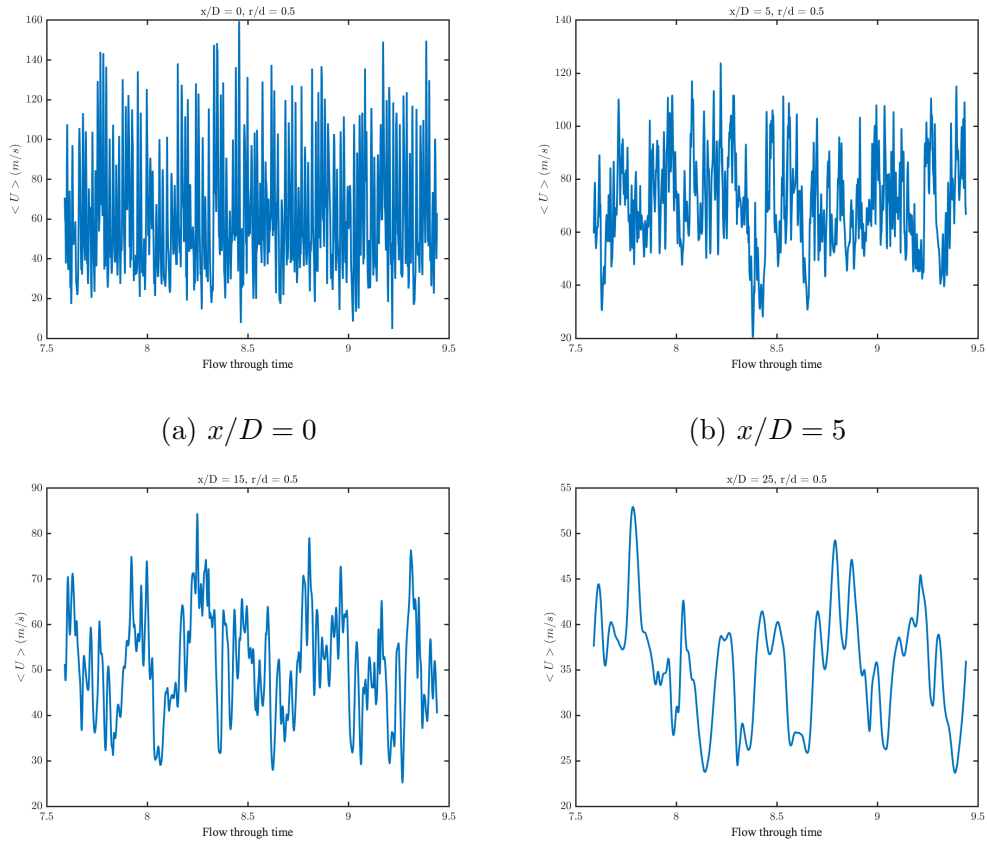

(a) $x/D = 0$ (b) $x/D = 5$

(c) $x/D = 15$ (d) $x/D = 25$

Figure 4.21: Time Varying Velocity Signal As a Function of FTT, at Nozzle Lipline

function. The cross correlation coefficient is calculated by splitting the time signal into 10 overlapping windows (5 in the case of $x/D = 5$) with 50% overlap and the cross correlation was computed for each of these windows of the two consecutive probe signals. The MATLAB function 'xcorr' is used for this purpose, which calculates the normalized cross correlation function based on two input time signals (The MathWorks (2022b)). The normalization is carried out by dividing the raw correlations with the auto correlation of each signal such that the auto correlation at zero lag is equal to 1. Then, the normalized cross correlation is averaged over these 10 windows to find the cross correlation of the two signals, and the results are given in figures 4.22a to 4.22.

At $x/D = 5$ there is an oscillatory behaviour of the cross correlation coefficients, which is associated with the Kelvin-Helmholtz instability in the jet shear layer. As the axial distance increases, the time scale of cross correlations increases, which is associated with the development of large scale turbulent structures far downstream. Consequently, the velocity power spectral density was computed for each of the above

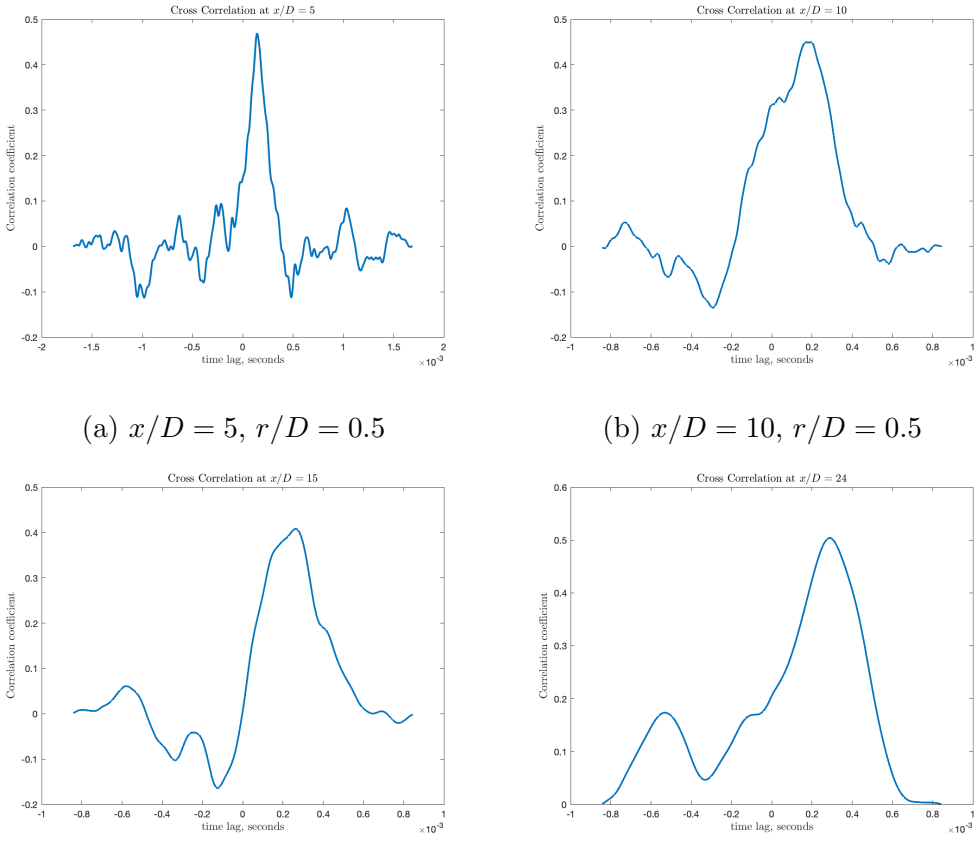

(a) $x/D = 5$, $r/D = 0.5$

(b) $x/D = 10$, $r/D = 0.5$

(c) $x/D = 15$, $r/D = 0.5$

(d) $x/D = 25$, $r/D = 0.5$

Figure 4.22: Cross Correlation Coefficient at Various Streamwise Locations

cross correlation functions and plotted against the Strouhal number. The spectra are calculated using 10 windows with 50% overlapping. The signal is sampled at 900 St_D for a sampling time of 1.5 FTT. Here, the spectra show highly dissipative behaviour at all axial distances and dissipate energy faster than the universal power decay law in the inertial sub-range.

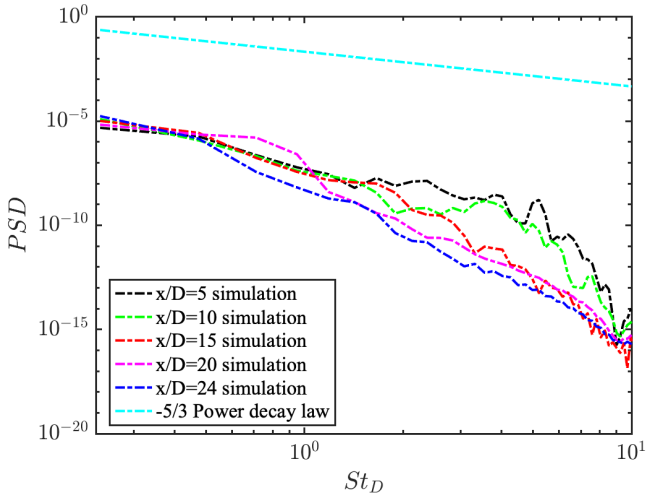

Figure 4.23: Velocity PSDs for Cross Correlation Coefficients, Plotted Against Kolmogorov's -5/3 Law

The cross correlations are used for estimating the convection velocity of the turbulent structures along the nozzle lipline. It is calculated by finding the time lag at which cross correlation peak is detected for each probe point, and then the separation distance between each probe ($x/D = 1$ in this case) is divided by the resulting time lag to find the convection velocity. The evolution of convection velocity (normalized by the jet exhaust velocity) along the lipline is shown in figure 4.24. A lot of fluctuations can be observed in the convection velocity, which can be attributed to the large gradients in flow variables caused by the coarse grid resolution. The convection velocity can be used along with a wavelet decomposition technique to analyze the components of sound in the jet flow, and a brief overview of this technique will be given in section 4.3.3. Due to the time constraints on this research, this analysis will be left for future studies.

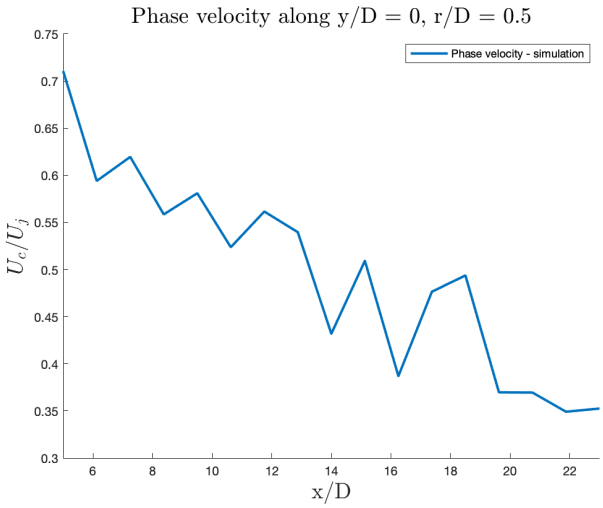

Figure 4.24: Streamwise Evolution of Convection Velocity Along the Nozzle Lipline

4.2 Freejet 22 Million Cells

As mentioned in section 3.2, the freejet grid is refined to 22 million cells, to check the effect of refinement on the flow characteristics. The results will be validated with corresponding freejet experiment data from Mancinelli and Camussi (2018). This case was simulated for ~ 5 flow through times (calculated using equation 4.1) using a time step of $2 * 10^{-8}s$ at a CFL number of $\sim$ 0.92 throughout the run. The time step can be expressed in dimensionless form by multiplying and dividing by the jet velocity at the nozzle exit (U_j) and nozzle exit diameter (D); it is obtained as $\Delta t_{nd} = 0.000196$. The simulation was run for $\sim$ 360 hours of CPU time using 252 cores on ASU's supercomputer Agave. Figure 4.25 shows the variation of mean velocity with flow through time at various streamwise positions along the nozzle axis. A statistically stationary mean can be observed at all measurement points, which is a clear improvement from the 8 million cells case, especially at a distance greater than x/D = 15 from the nozzle axis.

A snapshot of the simulation along z = 0 plane at a flow through time of 4.8 is

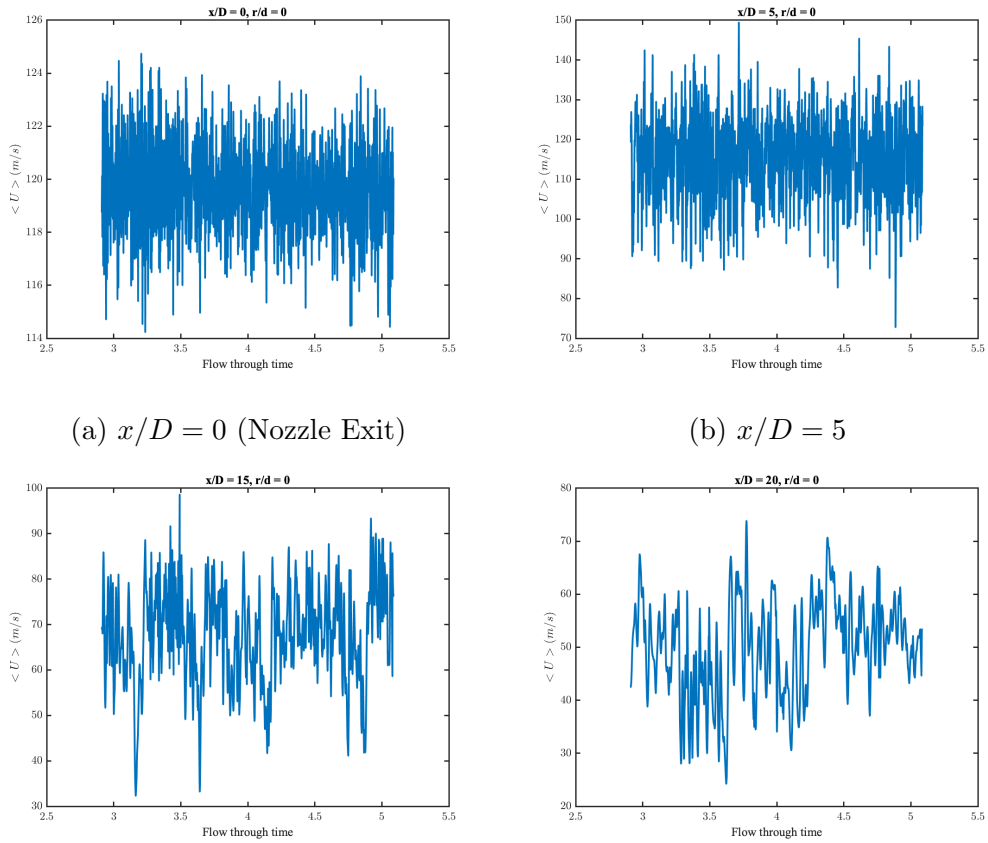

(a) $x/D = 0$ (Nozzle Exit)

(b) $x/D = 5$

(c) $x/D = 15$

(d) $x/D = 20$

Figure 4.25: Mean Velocity at Various Streamwise Locations As a Function of FTT

shown in figures 4.26 and 4.27. The instantaneous contours of jet Mach number and temperature field are shown, and we can observe a Mach number of 0.33 (corresponding to a mean velocity of 114 m/s) at the nozzle exit. However, since we are dealing with turbulent flows and the values are extremely fluctuating in nature, a time average of the Mach number and mean velocity was calculated, and a Mach number of 0.342 (118.34 m/s) is found at the nozzle exit, compared to a Mach number of 0.35 (120 m/s), found in the experiment.

The temperature field shows a similar behaviour to the one described in section 4.1, where the jet cools down at the nozzle exit, due to the conversion of thermal energy to kinetic energy, and heats up to an ambient temperature of 300 K as it

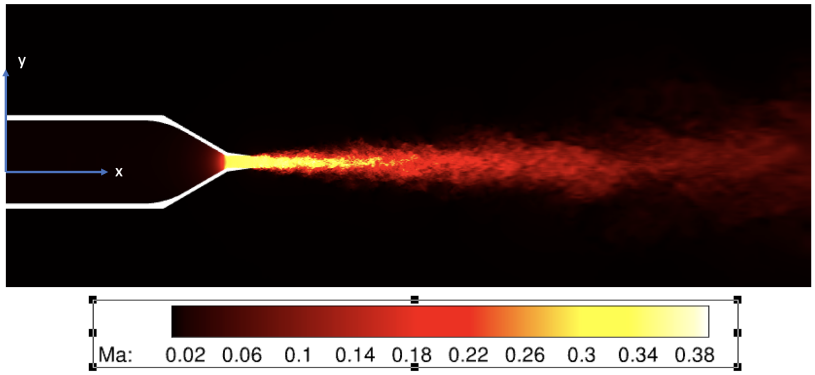

Figure 4.26: Contour Plot of Mach Number of the Jet at $z = 0$ Plane

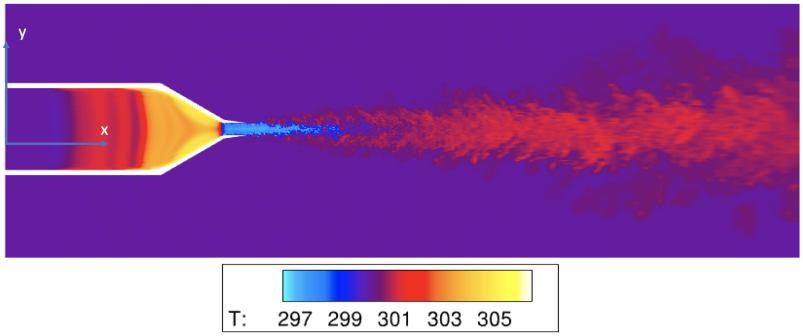

Figure 4.27: Contour Plot of Temperature of the Jet at $z = 0$ Plane

mixes with the quiescent fluid. The single point statistics are calculated along the nozzle axis to compare the simulation results with the experiment and also to check the effect of grid refinement on flow characteristics. The streamwise evolution of axial velocity is measured by placing 200 probe points along the nozzle axis, with each probe measuring the velocity signal at a sampling rate of 400 St_D, for a sampling time of 2 FTTs. The mean velocity of the jet ($\langle U \rangle$) normalized by the jet exhaust velocity (U_j), is plotted as a function of the axial distance from the nozzle exit (normalized by the nozzle exit diameter, D), as shown in figure 4.28.

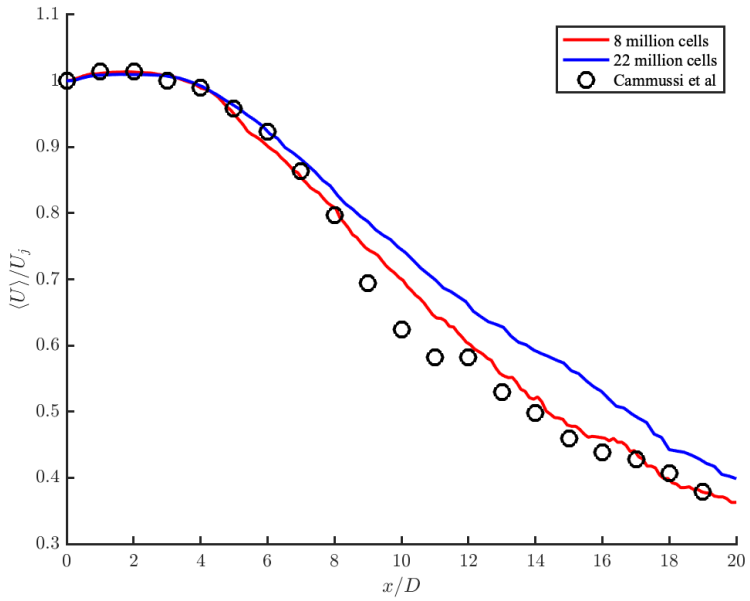

Figure 4.28: Streamwise Evolution of Mean Velocity

The blue curve represents the current 22 million cells simulation, red curve represents the 8 million cells simulation and black markers represent the experiment results. The 8 million cells simulation appears to have a better correlation with the experiment than the refined, 22 million cells case after axial distance of $x/D > 6$, but it should be noted that the coarse grid case was simulated for a longer period of time (10 FTT as compared to 5 FTT), hence we obtained a more statistically converged solution. The benefit of grid refinement on simulation results can be observed in the plot of turbulence intensity along the nozzle axis (figure 4.29), where the finer grid run shows less TI than the coarser grid run, and follows the experiment results more closely. Thus it is expected that the mean axial velocity will converge to the experiment value if the simulation is run for a longer period of time. The spanwise evolution of axial velocity ($\langle U \rangle / U_j$) and turbulence intensity ($\langle u'^2 \rangle^{(1/2)} / U_m$) at various axial locations is shown in figure 4.30 and 4.31. A top hat shape can be observed inside the potential core (x/D = 2), and the velocity curves assume the canonical Gaussian like

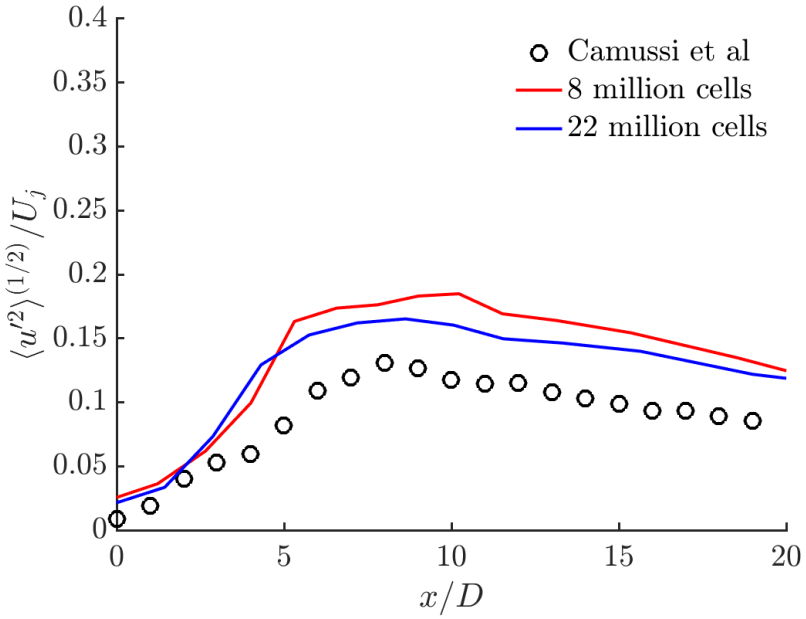

Figure 4.29: Streamwise Evolution of Mean Velocity

shape outside the potential core. The effect of grid refinement in the radial direction can be seen as we get a better correlation with the experiment results than the coarse grid simulation at x/D = 2 and 6 (figure 4.30). However, as the simulation is not run for enough time, the results are not statistically converged and the velocity starts to deviate from experiment at $x/D > 10$. This trend can also be observed in figure 4.31, where a fluctuating value of turbulence intensity from $-4 < z/d < 4$ can be seen at all streamwise probe points, as the jet is still in the transient phase of turbulence, and thus the flow statistics are yet to fully stabilize.

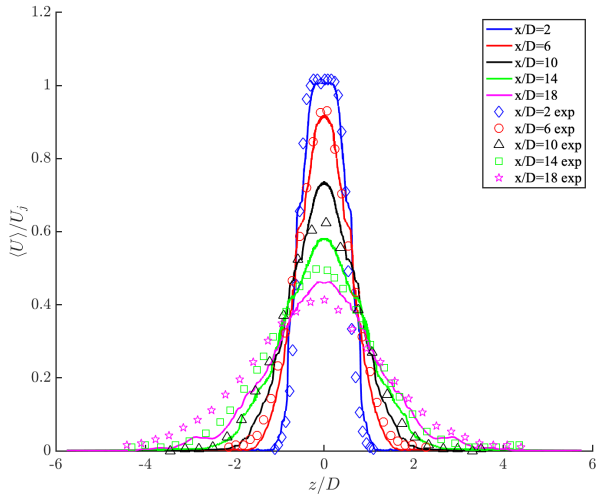

Figure 4.30: Spanwise Variation of Mean Velocity at Various Axial Distances

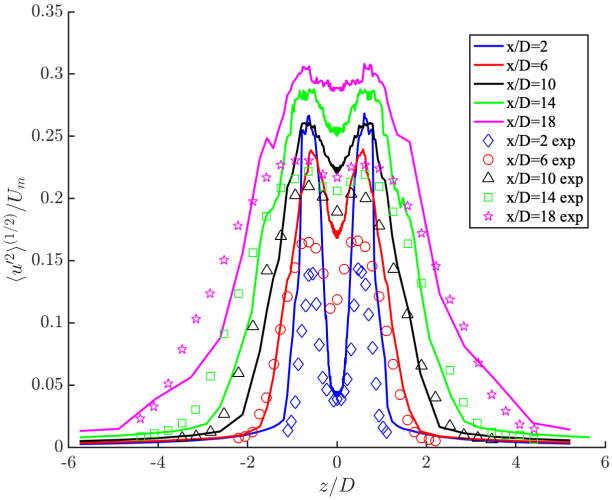

Figure 4.31: Spanwise Variation of Turbulence Intensity at Various Axial Distances

The velocity spectra at various streamwise positions along the nozzle axis are plotted in figures 4.32 to 4.36. Similar to the 8 million cells case, the velocity Power Spectral Density is calculated at 5 axial positions, i.e. at x/D = 3, 7, 11, 15 and 19 (measured from the nozzle exit) and plotted against the Strouhal Number (calculated from equation 4.2). The velocity is sampled at the axial positions shown above using point probes placed in the simulation domain, at a sampling rate of 400 St_D for a sampling time of 2 FTTs. The power spectral density is calculated using the pwelch() function on MATLAB, using 10 windows with 50% and a Hanning window function.

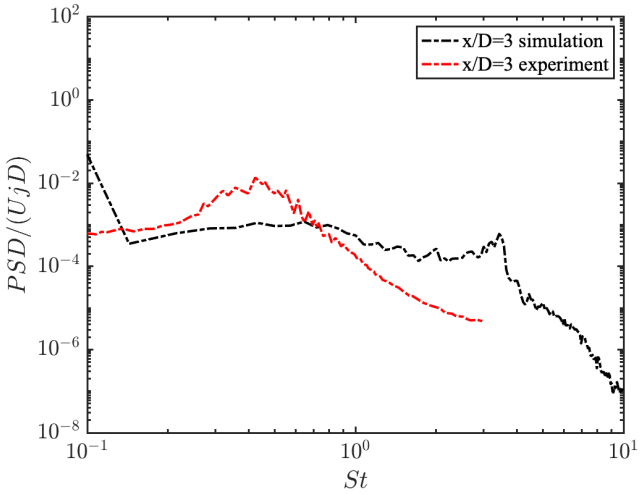

Figure 4.32: Velocity PSD at $x/D = 3$

The correlation of velocity spectra with the experiment is encouraging at lower Strouhal numbers, however at $St_D > 1$, the simulation tends to taper off faster than the simulation. This can be due to the relatively coarse resolution grid that fails to capture the smaller/sub grid scales of turbulence and hence there is a high level of turbulence in this region. This instability propagates further downstream and can also be seen in figure 4.33 at a Strouhal number of 2, where there is a bump in the energy and faster dissipation after this. Also, the simulation is still in the

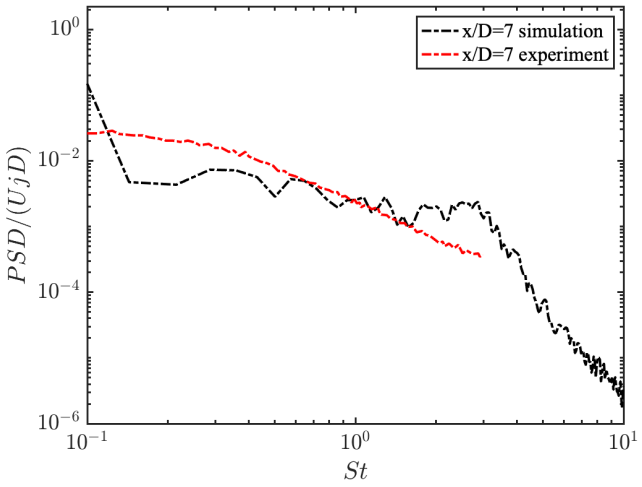

Figure 4.33: Velocity PSD at $x/D = 7$

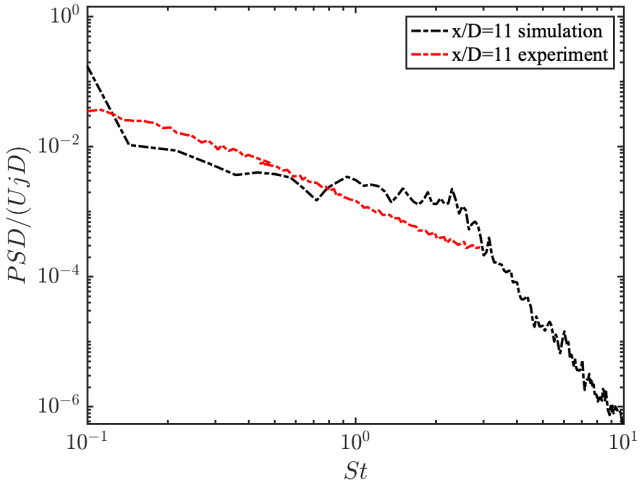

Figure 4.34: Velocity PSD at $x/D = 11$

transient phase so the statistics have not 'settled' and the simulation needs to be run longer for a more accurate result. Figure 4.37 shows the velocity spectra compared to the Kolmogorov's -5/3 law to check for the dissipation in the inertial sub range. The presence of transient effects at downstream locations, i.e. $x/D > 11$ can be observed in this figure, as we can see a hump in the spectra at $St_D > 0.6$. This is because of the fact that the sub-grid scales of turbulence are modelled by a LES code and not exactly resolved (like large scales), therefore if the grid spacing is coarse at

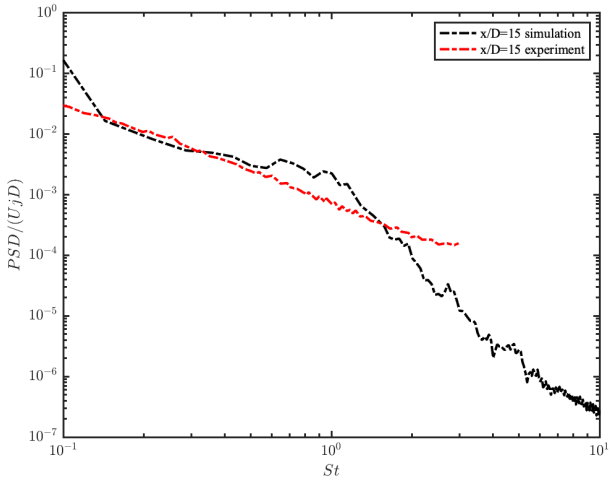

Figure 4.35: Velocity PSD at $x/D = 15$

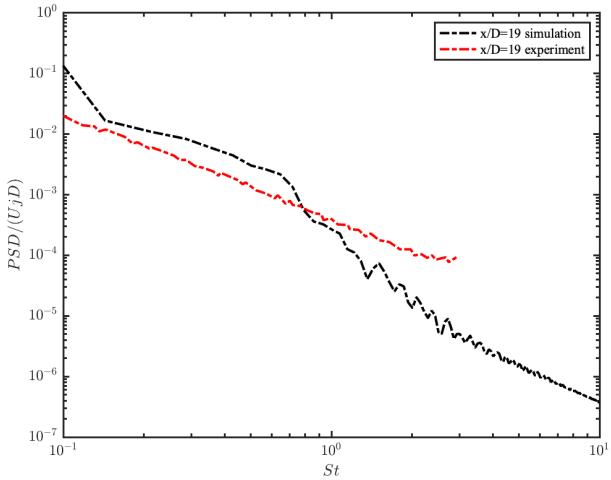

Figure 4.36: Velocity PSD at $x/D = 19$

downstream locations (where large scale structures of the jet break down to smaller scales and dissipate the energy to ambient air) the grid will be too large to model this viscous dissipation, and thus, it will be faster than the Universal dissipation rate. To counteract these coarse grid effects, the turbulent simulation should be run for a longer time, so that the initial transient effects settle down and the flow becomes statistically stationary (mean flow characteristics do not change with time).

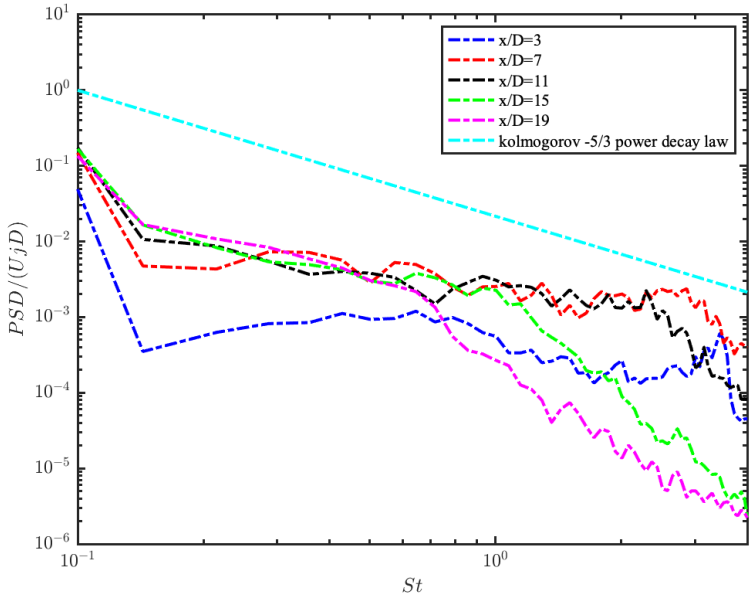

Figure 4.37: Velocity Spectra Compared to Kolmogorov's -5/3 Decay Law

4.2.1 Lipline Statistics

Mean velocity, static pressure and static temperature are measured along the nozzle lipline using 200 probe points equally spaced along the nozzle lipline extending from $x/D = 0$ (measured from nozzle exit) to $x/D = 25$ and $r/D = 0.5$. Figure 4.38 shows the variation of mean velocity, static pressure and static temperature along the nozzle lipline, calculated by taking a time average of the probe signal which sampled at a frequency of 400 St_D and sampling time of 2 FTT.

As was observed in section 4.1.1, the mean velocity increases sharply just at the exit of the nozzle, as the ambient air at rest is accelerated by the high speed jet. This sharp increase in velocity causes a consequent sharp decrease in temperature and pressure (as per the conservation of energy principal). The temperature and pressure recover to their respective values in the ambient air as the jet slows down further. Figure 4.39 shows the time varying velocity signal plotted against flow through time, to demonstrate the statistically stationary mean at various axial positions.

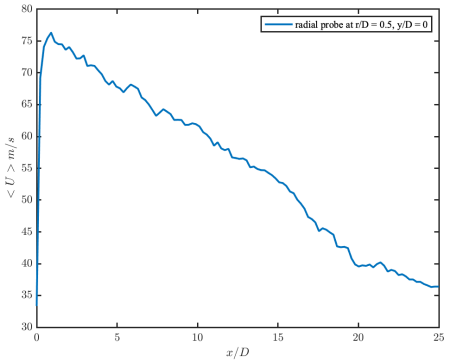

(a) Mean Velocity

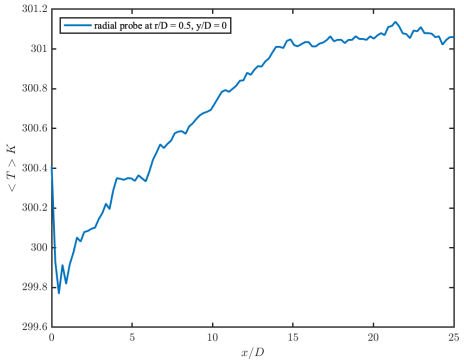

(b) Time Averaged Temperature

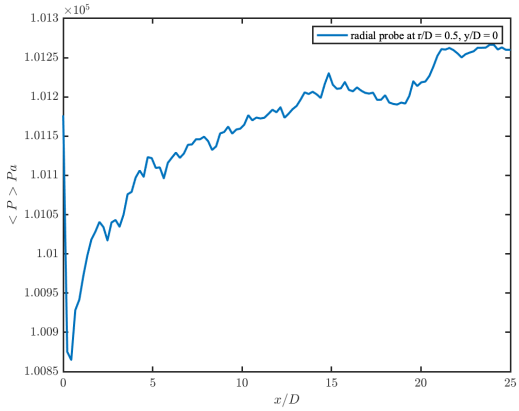

(c) Time Averaged Pressure

Figure 4.38: Variation of Statistics Along Nozzle Lipline

Two point statistics are computed along the nozzle lipline to check whether the large scale turbulent structures dissipate energy to smaller scales according to Kolmogorov's -5/3 law. The two point correlations are computed at two consequent probes separated by a distance of $1D$ (along the nozzle lipline), and the cross correlation between two velocity signals is calculated using equation 4.3 and the xcorr() function on MATLAB. It is calculated by splitting the signal into 10 overlapping windows, with 50 % overlap between each window, and then averaging the cross correlation over these windows. The cross correlations at various axial positions is given in figure 4.40. As given in section 4.1.1, the Kelvin - Helmholtz instability can be

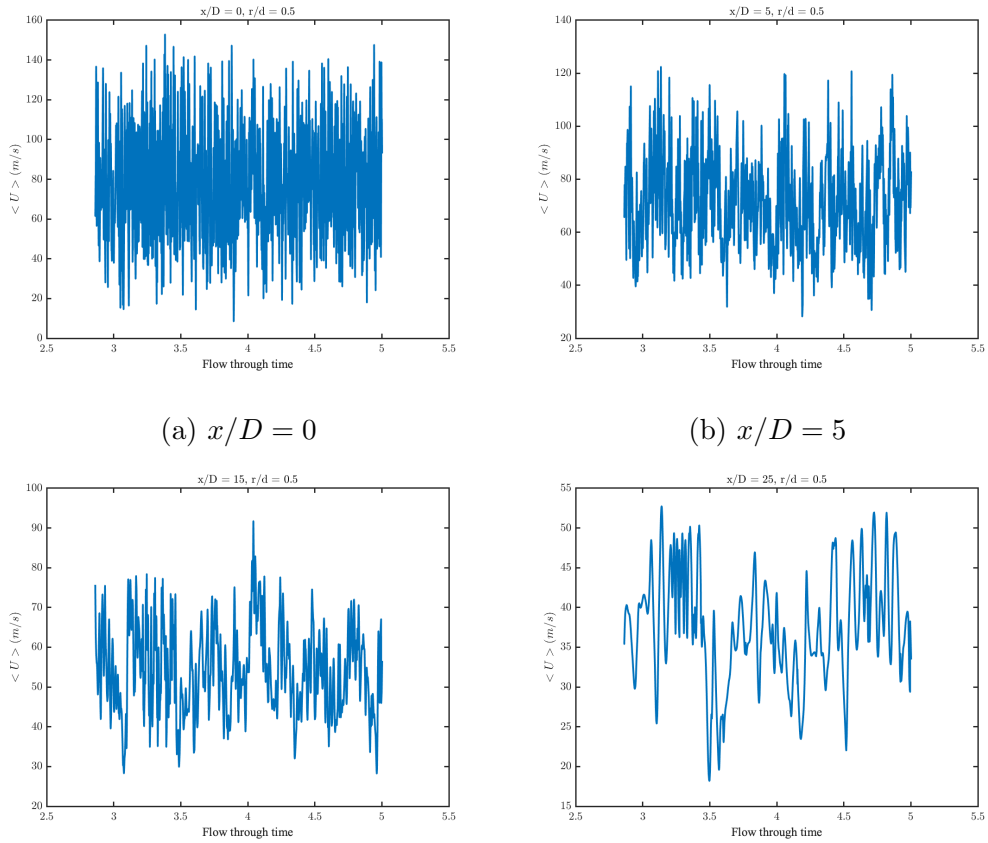

(a) $x/D = 0$ (b) $x/D = 5$

(c) $x/D = 15$ (d) $x/D = 25$

Figure 4.39: Time Varying Velocity Signal as a Function of FTT, At Nozzle Lipline

observed at small axial distances close to the nozzle exit by the high oscillations of the cross correlations. The increasing time scale of correlations indicate the development of turbulent structures far downstream of the nozzle exit. Once the cross correlation is computed at each streamwise position, the power spectral density is calculated based on the correlations, to check the dissipation of energy in the inertial subrange. The PSD is calculated using Welch's method on MATLAB, using 10 windows with 50% overlap between each window. The corresponding spectra are then compared with Kolmogorov's -5/3 law (figure 4.41), and at axial distance greater than $x/D = 10$, the spectra follow the Universal dissipation law till a Strouhal number of 1, then decay rapidly. This is again because of the large dissipation caused by coarse resolution

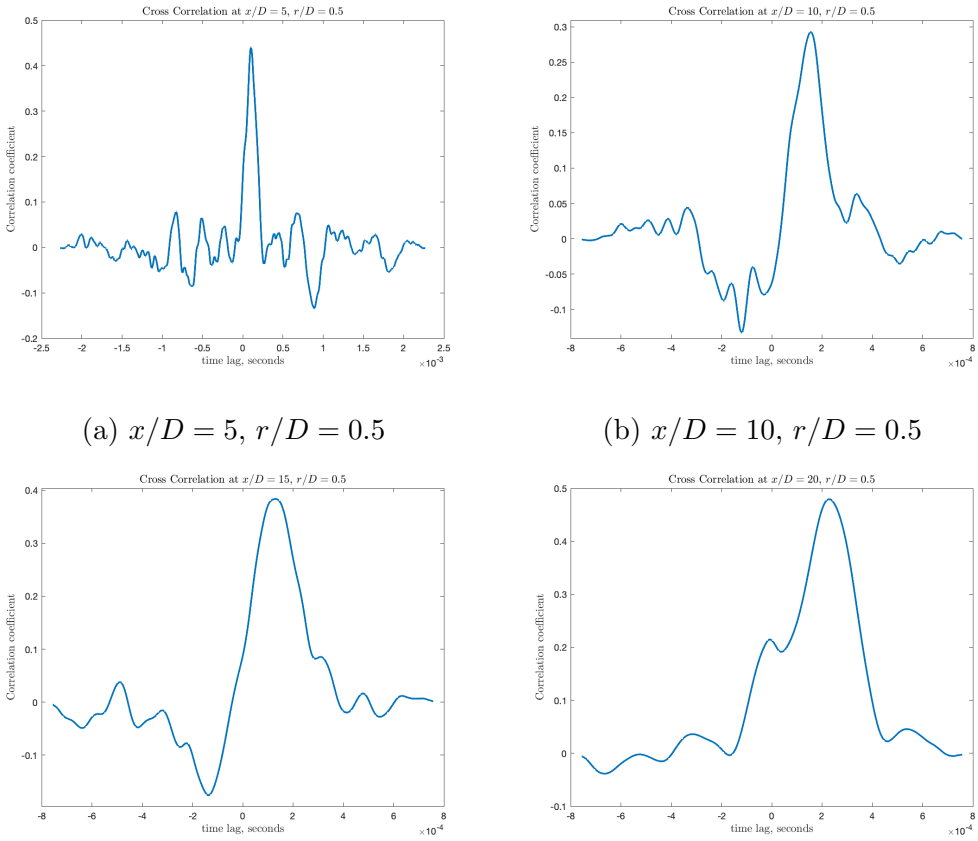

(a) $x/D = 5$, $r/D = 0.5$

(b) $x/D = 10$, $r/D = 0.5$

(c) $x/D = 15$, $r/D = 0.5$

(d) $x/D = 20$, $r/D = 0.5$

Figure 4.40: Cross Correlation Coefficient at Various Streamwise Locations

of grid in the downstream region. The cross correlations are used for estimating the convection velocity of the turbulent structures along the nozzle lipline. The evolution of convection velocity (normalized by the jet exhaust velocity) along the lipline is shown in figure 4.42. As the simulation in this case has not been run till a statistically stationary state is attained (i.e., to a Flow Through Time of 10 or above) and still has transient effects of turbulence, the flow statistics have not settled, and a large fluctuation in the convection velocity can be observed. As detailed in section 4.1.1, the convection velocity can be coupled with a wavelet decomposition technique to better understand the noise characteristics, and will be left for future investigations.

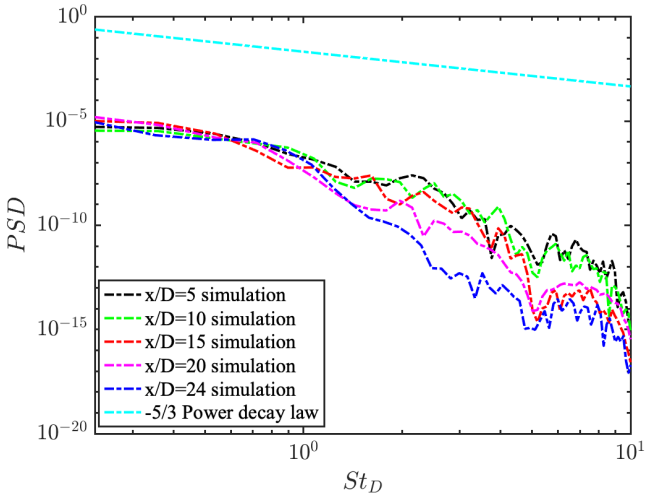

Figure 4.41: Velocity Spectra Compared to Kolmogorov's -5/3 Decay Law

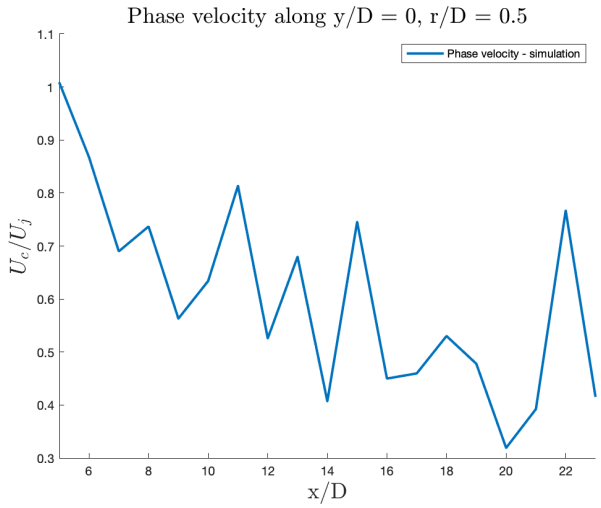

Figure 4.42: Streamwise Evolution of Convection Velocity

4.3 Installed Jet 15 Million Cells

The installed jet simulation will be validated using data taken from experiments performed by Meloni *et al.* (2019), as mentioned before. A baseline simulation was run on a grid of 1.5 million cells, to check the correct set up of the code, then the grid was refined subsequently to 8 million cells and 15 million cells to check the effect of grid refinement on the accuracy of the set up. Once it was established that the

code was producing encouraging results with respect to the experiment results, the 15 million cells case was chosen for further analysis. The 1.5 million cells and 8 million cells case will not be discussed in this report for maintaining brevity and keeping the report concise. A brief overview of the effect of grid refinement on the results is given in figure 4.44.

The set-up described in section 3.3 is simulated for $\sim$ 10 flow through times using a time step of $3.0184 * 10^{-8}$ s at a CFL number of $\sim$ 0.863 throughout the run. The time step can be expressed in dimensionless form by multiplying and dividing by the jet velocity at the nozzle exit and nozzle exit diameter; it is obtained as $\Delta t_{nd} = 0.00055$. The simulation was run for 179 hours of CPU time (approximately 8 days of computing time) using $\sim$ 280 cores on the ASU Agave computing cluster. Figure 4.43 shows the variation of mean flow velocity with flow through times at various axial positions located along the nozzle center line, with the velocity at each position monitored by using a point probe placed in the simulation domain. We can observe that the statistical mean of velocity remains constant at all the 4 axial positions, which are chosen in the following regions - inside potential core (x/D = 3), just outside the potential core (x/D = 5), mixing region (x/D = 10) and far field (x/D = 20).

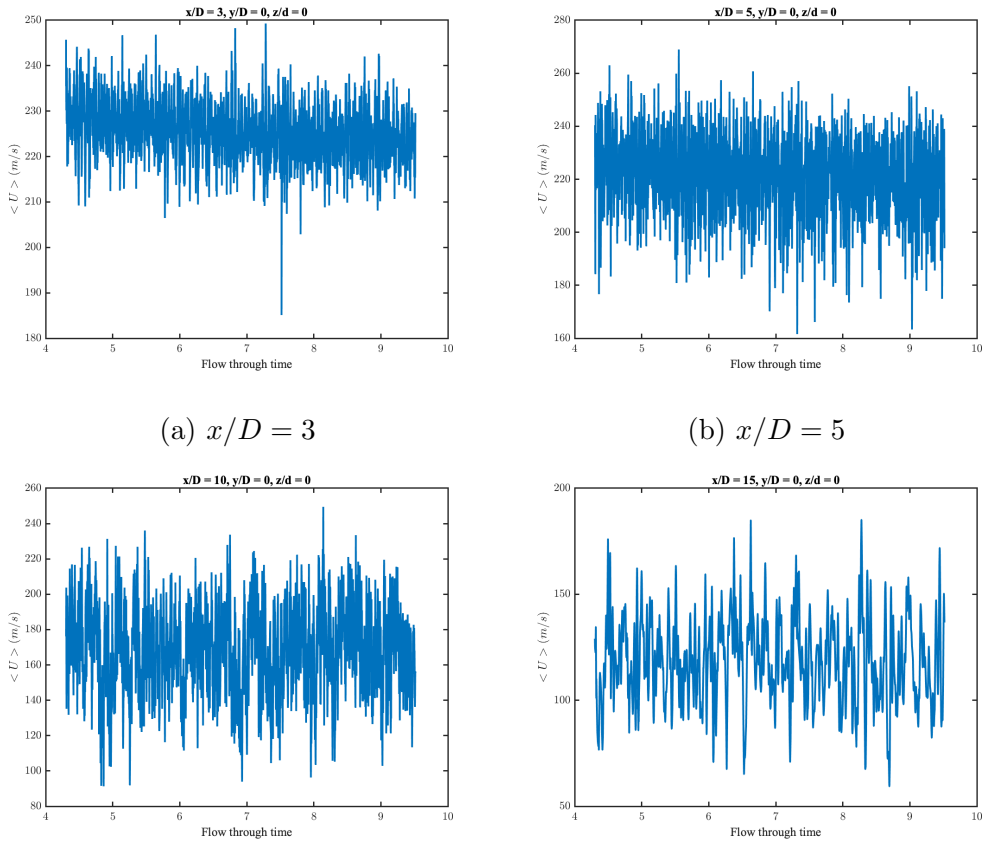

(a) $x/D = 3$ (b) $x/D = 5$

(c) $x/D = 10$ (d) $x/D = 20$

Figure 4.43: Mean Velocity at Various Streamwise Locations As a Function of FTT

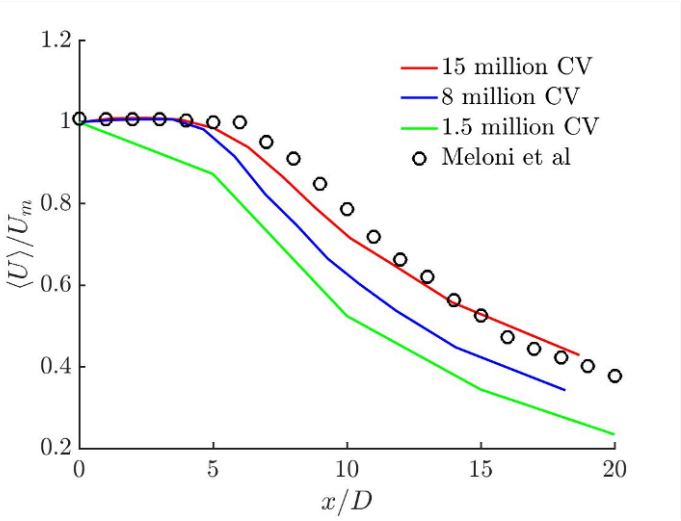

Figure 4.44: Comparison of Normalized Mean Centerline Velocity As a Function of Axial Distance From the Nozzle Exit (at 3 Mesh Refinement Levels)

A snapshot of the flow field at a flow through time of $\sim$ 10 along z = 0 plane is shown in figures 4.45, 4.46, 4.47 the contour plots depict the instantaneous mach number, mean velocity and temperature respectively. We can observe a mach number of 0.65 at the nozzle exit, corresponding to a mean velocity of 220 m/s, as compared to a experiment mach number of 0.7 (mean velocity of 228 m/s). The temperature field shows a similar behaviour to the one described in section 4.1, where the jet cools down at the nozzle exit due to a conversion of thermal energy to kinetic energy, and heats up to the ambient temperature value of 300 K as it mixes with the quiescent air. Figure 4.48 shows the contour plot of mean velocity at $x/D = 10$ plane (D is the nozzle exit diameter) measured from the nozzle exit, showing the attachment of the jet along the plate surface and the exact location at which the jet attaches to the plate will be shown in subsequent sections.

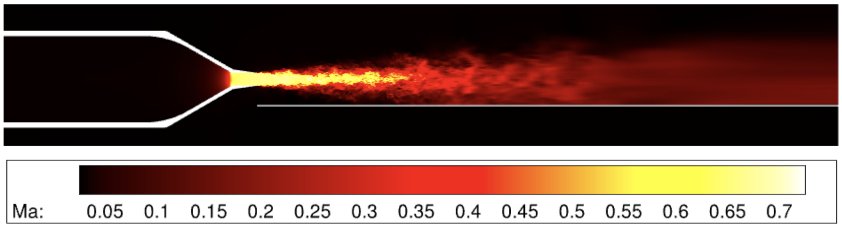

Figure 4.45: Contour Plot of Mach Number at $z = 0$ Plane

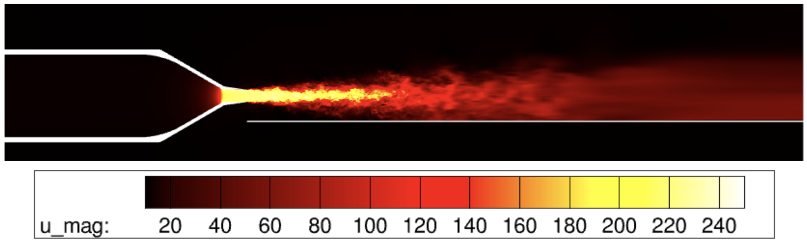

Figure 4.46: Contour Plot of Mean Velocity (in m/s) at $z = 0$ Plane

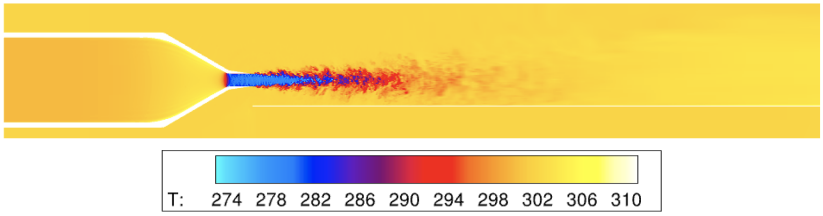

Figure 4.47: Contour Plot of Temperature (in K) at $z = 0$ Plane

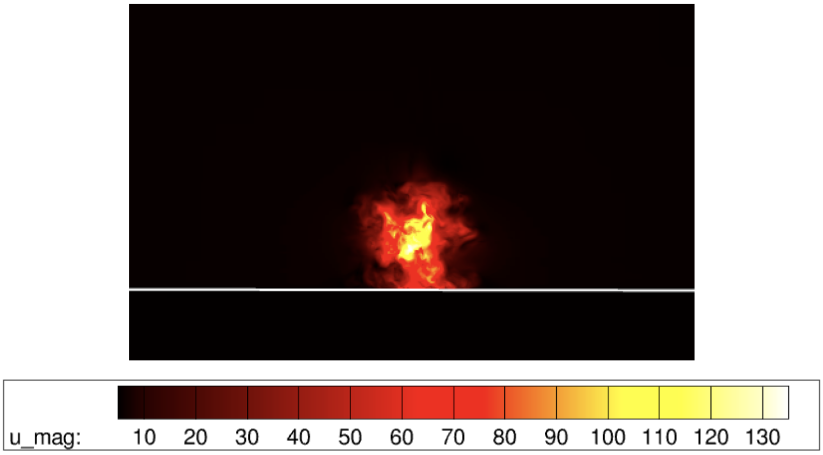

Figure 4.48: Contour Plot of Mean Velocity (in m/s) at $x/D = 10$ Plane

4.3.1 Single Point Statistics

The streamwise evolution of mean velocity was measured by placing 200 probe points along the nozzle axis (y = 0, z = 0) and a time average of the probe signals was computed. The mean velocity, normalized by the nozzle exit velocity (here, it is defined as U_m) is plotted in figure 4.49, where $x/D = 0$ corresponds to the nozzle exit, the solid line indicates the simulation results and the dotted line indicates the experiment results (Meloni *et al.* (2019)). We can observe that the simulation slightly under-predicts the decay in the mean velocity, as the potential core length predicted by the simulation is $x/D \sim 6$, as opposed to $x/D \sim 7$ found in the experiment. This behaviour is expected, as the grid resolution used in this simulation is still relatively coarse, and hence we expect a faster decay of statistics along the streamwise

direction. The wall pressure variation along the plate surface is measured using virtual probes placed along the plate surface which record the time varying static pressure, as calculated by the simulation. To validate the wall pressure values measured by the

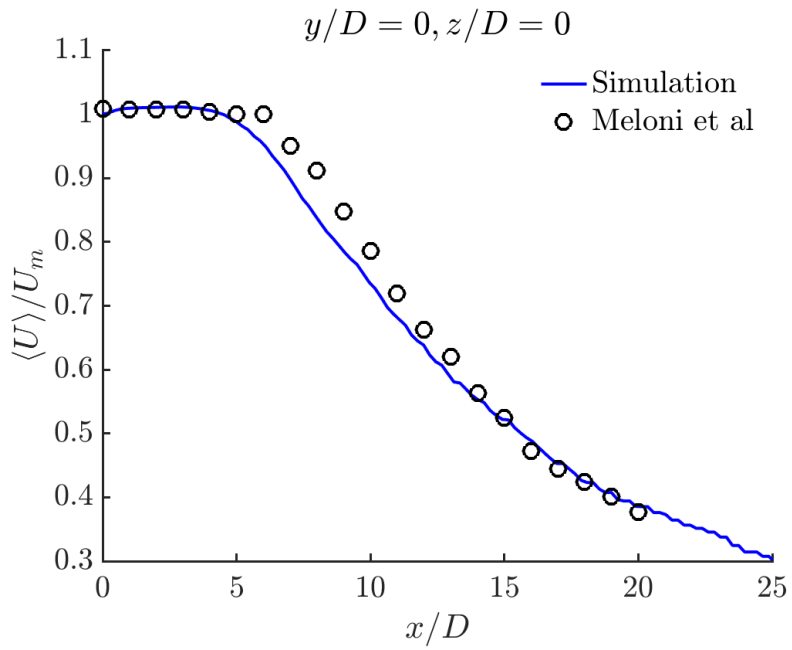

Figure 4.49: Variation of Mean Velocity Along the Nozzle Axis

simulation, 200 probe points are placed on the plate surface, along the line - $x/D = 0$ to $x/D = 25$, $y/D = -2$, $z/D = 0$, where $x/D = 0$ corresponds to the nozzle exit and $y/D = -2$ corresponds to the flat plate top surface. The coefficient of pressure (C_P) is calculated as defined by Meloni *et al.* (2019), and is given as follows -

$$C_P = \frac{\bar{P} - P_{amb}}{q} \tag{4.4}$$

where $\bar{P}$ if the time average of wall pressure signals, P_{amb} the ambient pressure in the domain, q is the dynamic pressure, calculated as follows -

$$q = \frac{1}{2} \cdot \gamma \cdot M_j^2 \cdot P_{amb} \tag{4.5}$$

where M_j is the Mach number at the nozzle exit and γ is the ratio of specific heats. Figure 4.50 shows the plot of variation of C_P along the plate surface at probe points as mentioned above. We can observe an encouraging correlation with the experiment up to $x/D = 15$, after which the fluctuation of C_P increases because of the coarse grid resolution downstream. A spike can be observed at the axial distance of $x/D = 10$ appears where the jet first comes into contact with the plate. A better result is expected with an increase in grid resolution in the boundary layer that develops along the plate surface, however, as the boundary layer formed is turbulent, the relationship is not so straightforward, and further analysis is required. Qualitatively speaking, from the wall pressure data, we can primarily observe three zones of the jet grazing over the plate surface (Meloni *et al.* (2019)) -

1) Free jet - from $x/D = 0$ to $x/D = 10$, where the jet is yet to come in contact with the plate, the pressure is equal to ambient pressure, and $C_P = 0$.

2) Impact zone - Jet impinges on the plate surface, from $x/D = 10$ to $x/D = 20$, causing an increase in the C_P values.

3) Turbulent Boundary Layer - After $x/D = 20$, the C_P starts to flatten, indicating the formation of a Turbulent Boundary Layer (TBL). However, as mentioned above, due to coarse grid resolution, it is not well resolved in the simulations and we can observe fluctuations in this region.

The contact point of the jet with plate can be confirmed with the plot of flatness (or kurtosis), as shown in figure 4.51 The kurtosis of the wall pressure signals (along $x/D = 0$ to 25, $y/D = -2$, $z/D = 0$) is calculated using the kurtosis() function of MATLAB, which calculates the kurtosis of a time signal using the following formula-

$$k = \frac{E(P - \mu)^4}{\sigma^4} \tag{4.6}$$

where k is the kurtosis/flatness, P is the wall Pressure data under consideration, μ

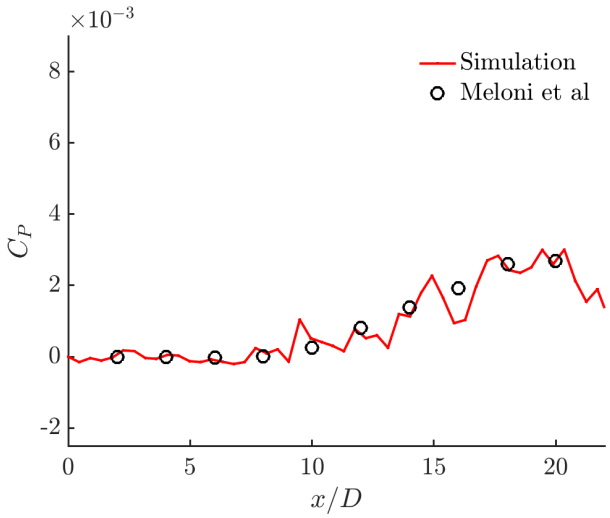

Figure 4.50: Variation of C_p Along the Plate Surface, At Probes Located Along the Line $y/D = -2$, $z/D = 0$

is the mean of the data, σ is the standard deviation of P, and $E()$ is the expected value of the quantity in the parenthesis. The flatness has a value of 3 till $x/D = 10$, indicating a Gaussian distribution in that region, which is typical of a 'freejet', before it hits the surface. The flatness value jumps to 5 at $x/D \sim 10$, at which point the jet strikes the plate, and a boundary layer starts to develop along the surface. This value starts fluctuating after $x/D = 15$, because the grid is stretched in the streamwise direction, and the resolution in the boundary layer becomes coarse, which causes larger gradients in Pressure. The value further increases beyond $x/D = 20$, because the grid is stretched, and it needs to be further refined to better resolve the turbulent boundary layer. The skewness of wall pressure signals is also calculated using the same probe points as mentioned above, and the skewness() function available on MATLAB is used for calculating this. It calculates the skewness of data using the following formula -

$$s = \frac{E(P - \mu)^3}{\sigma^3} \tag{4.7}$$

where s is the skewness, P is the wall pressure data, μ is the mean of the data,

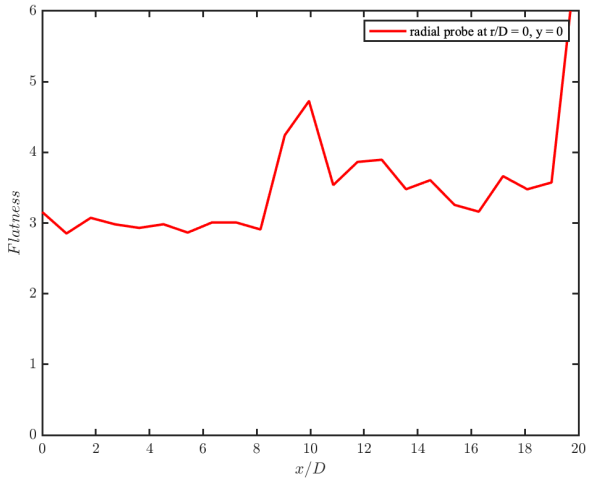

Figure 4.51: Variation of Flatness Along the Plate Surface, At Probes Located Along the Line $y/D = -2$, $z/D = 0$

σ is the standard deviation of P, and $E()$ is the expected value of the quantity in the parenthesis. The value drops to -0.4 at $x/D = 10$, further confirming the point where the jet strikes the plate. It increases to 0.4 immediately after, indicating the large-scale pressure fluctuations induced by the flow structures impacting the plate surface, which are intermittent in nature (Meloni *et al.* (2019)). However, the skewness decreases to -0.3 again, indicating asymmetry in the jet flow caused by the stretching/coarsening of the grid in that direction.

The spectral analysis of the wall pressure signals was performed by performing fast Fourier transform (FFT) of the same. FFTs of the wall pressure signals are computed at probe points located along the line $y/D = -2, z/D = 0$ at $x/D = 5$, $x/D = 15$, $x/D = 25$, where the axial distance x/D is measured from the nozzle exit. FFTs are computed using Welch's method, as detailed in section 4.1. The Power Spectral Density is calculated at the probe points as mentioned above and plotted against the Strouhal number St_D, which is calculated as follows -

$$St_D = \frac{(f * D)}{U_j} \tag{4.8}$$

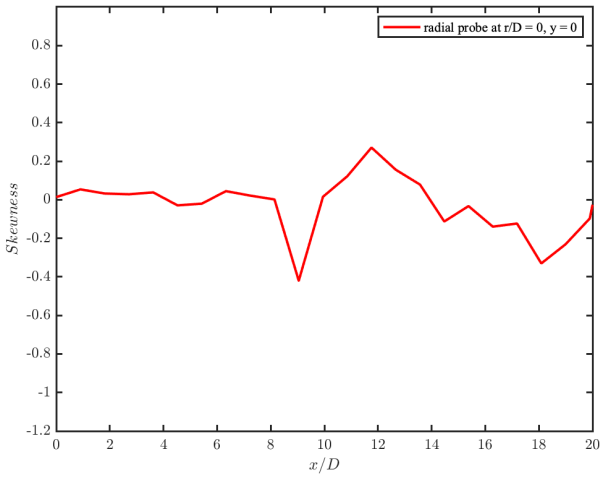

Figure 4.52: Variation of Skewness Along the Plate Surface, At Probes Located Along the Line $y/D = -2$, $z/D = 0$

where f is the frequency obtained by Welch's method, D is the nozzle exit diameter and U_j is the nozzle exit velocity, which is found as 220 m/s. The wall pressure is sampled at a Strouhal number of 400, for a sampling time of ~ 5 flow through times. The measured data is compared with experimental data (Meloni *et al.* (2019)) for validation, and the results are shown in figures 4.53 to 4.55.

We observe a poor correlation with the experiment in all three cases, primarily because the coarse grid causes large pressure fluctuations in the wall pressure signals, and we can observe the presence of high frequency components at all probe points. However, qualitatively speaking, certain trends are similar to that of the experiment - at $x/D = 5$, we observe a similar trend to that of the experiment, till $St_D = 1$ because the jet is yet to come into contact with the plate and only the variation of ambient pressure is measured by the probe. A bump in the energy spectrum can be seen at $St_D = 6$, possibly due to the instability in the shear layer, caused by a coarse grid resolution in the boundary layer at the nozzle exit, and an under-prediction of flow quantities in the jet shear layer. At $x/D = 15$, the jet is fully in contact with the plate, and it can be seen that the wall pressure PSD follows a similar trend to that of the experiment

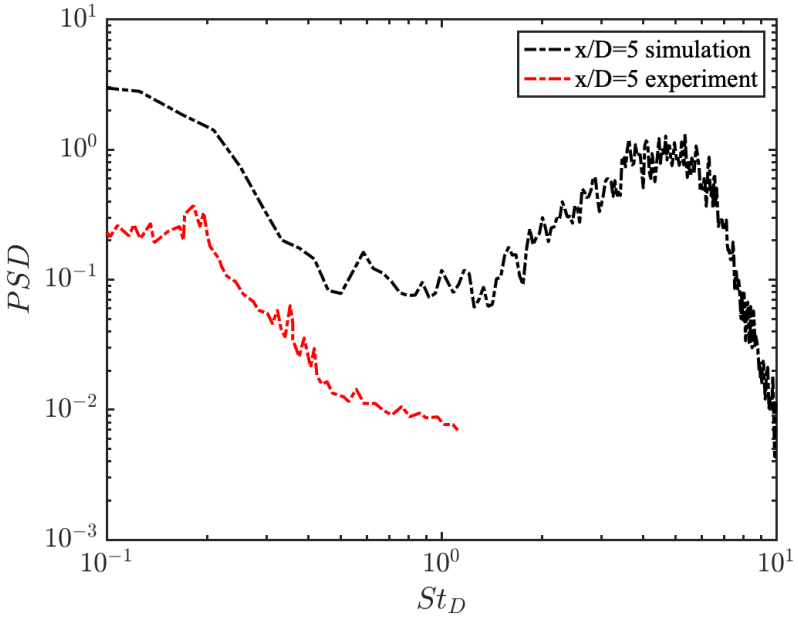

Figure 4.53: Wall Pressure PSD at $x/D = 5$

till $St_D = 1$, but dissipates sharply afterwards. In this region, the grid is not fine enough to resolve the boundary layer forming on the surface and the formation of small scale structures which eventually dissipate the energy. Thus the cascade of energy from the large scale turbulent structures to small scale structures is not well predicted, and this could be responsible for the rapid dissipation of energy at Strouhal number greater than 2. At larger axial distances from the nozzle, i.e. at $x/D = 25$, the Turbulent Boundary Layer is fully formed, which can observe this in the PSD, wherein the spectrum is parallel to the power decay law $f^{-7/3}$, typical of a TBL. However, a bump in the energy spectrum can be seen at $St_D \sim 0.5$, indicating the presence of a low frequency component at this axial distance. The exact cause of this bump cannot be qualitatively determined, but can be an artifact caused by the coarse grid resolution in this region. Thus, qualitatively speaking, an encouraging correlation with the experiment can be observed for certain quantities, however with further grid refinement, a better correlation is expected.

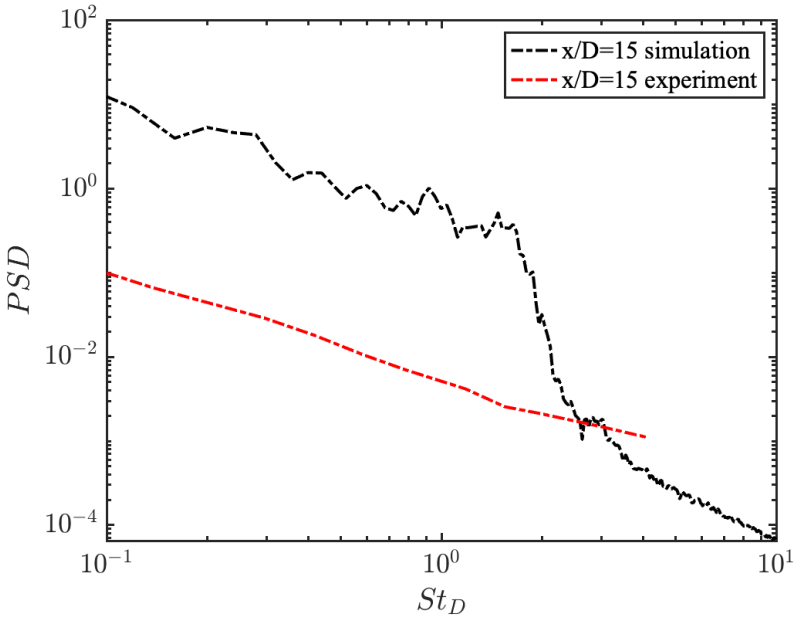

Figure 4.54: Wall Pressure PSD at $x/D = 15$

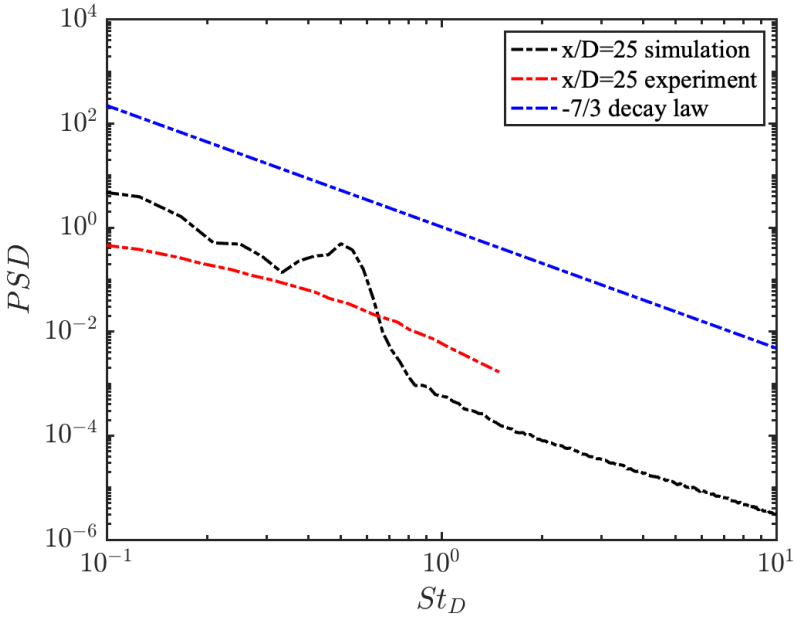

Figure 4.55: Wall Pressure PSD at $x/D = 25$

4.3.2 Two Point Statistics

The two point correlations are computed at two consecutive probe points located along the plate surface to verify the results with the experiment. The cross correlation function is calculated using equation 4.3 defined in section 4.1.1. The signal was split into 15 windows with 50% overlap and the cross correlation function 'xcorr' of MATLAB (using normalization parameter) was applied on the overlapping windows. The normalized cross correlations were then averaged over these 15 windows, and compared against experiment results. The probes are placed at $x/D = 5$, 15, 20, 25 and $y/D = -2$, $z/D = 0$. The plots of the correlation coefficient at these probe points is given in figures 4.56 to 4.59.

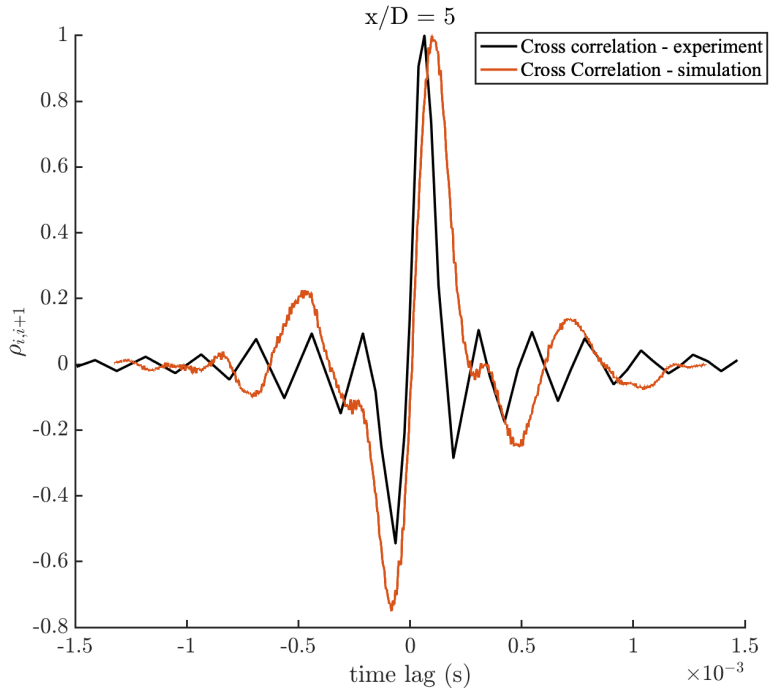

Figure 4.56: Cross Correlation Coefficient at $x/D = 5$

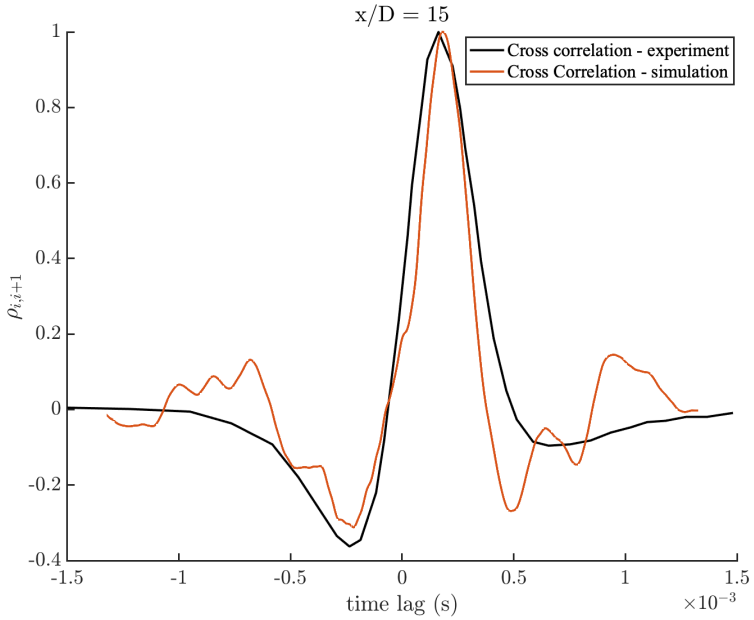

Figure 4.57: Cross Correlation Coefficient at $x/D = 15$

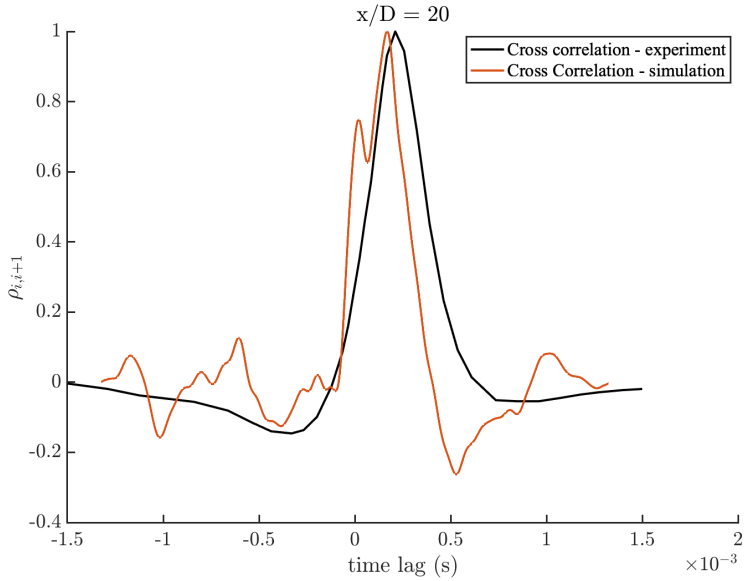

Figure 4.58: Cross Correlation Coefficient at $x/D = 20$

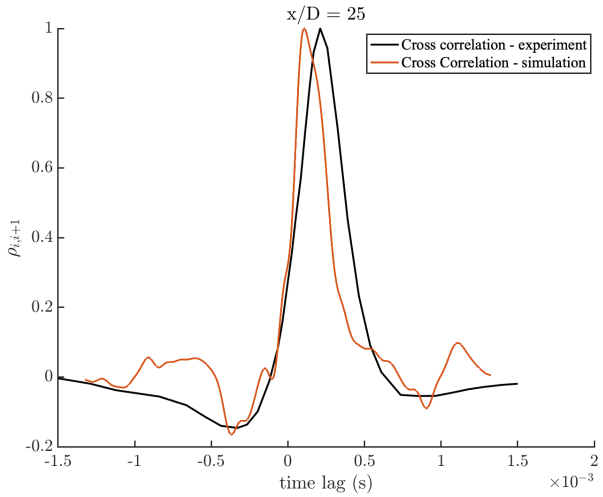

Figure 4.59: Cross Correlation Coefficient at $x/D = 25$

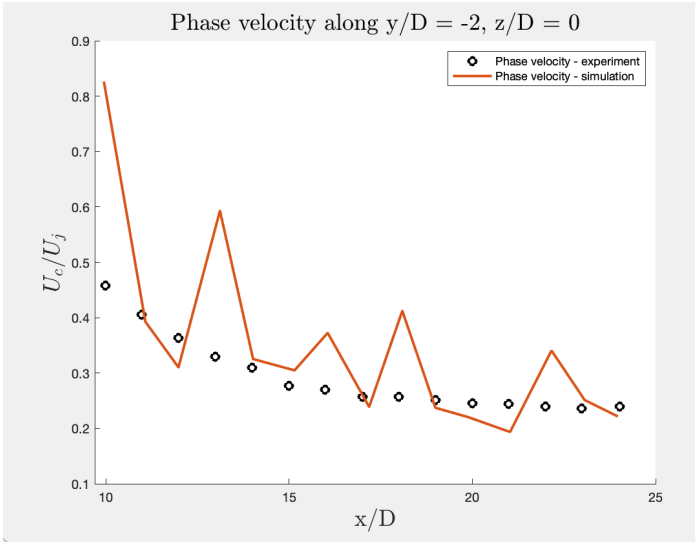

Figure 4.60: Convection Velocity U_c at Various Axial Distances Along the Plate Surface

The above plots show an encouraging correlation with the experiment, with the simulation accurately predicting the time lag at which the pressure signals of two consecutive probe signals are perfectly correlated, at the axial distances shown. At small axial distances, i.e. at $x/D = 5$, an oscillatory behaviour of the cross correlation function can be observed, which can be attributed to the Kelvin-Helmholtz instability within the potential core. At locations downstream of the potential core,

the oscillations dampen and a negative - positive bump appears. This is caused by the development of large-scale turbulent structures after the jet hits the plate surface, and it is confirmed by the increasing time scale of the cross correlation function as we go from $x/D = 15$ to $x/D = 25$. The cross correlation function is further used for calculating the convection velocity U_c at streamwise points along the plate surface after the jet comes in contact with it. The convection velocity is measured at the same probe locations as the cross correlations detailed above, and is calculated by finding the time lag at which the cross correlations attain the maximum value. The separation distance between two consecutive probes (i.e., $x/D = 1$) is then divided by this time lag to obtain the convection velocity. Figure 4.60 shows the convection velocity (normalized by the jet exhaust velocity) comparison between the simulation and experiment. A large fluctuation can be observed in the simulation results, however, with increased grid refinement, more encouraging results are expected. The convection velocity shows the speed of convection of turbulent structures along the plate surface, and certain characteristic features of acoustic and hydrodynamic components of jet flow can be distinguished from the trend of this convection velocity. However, separation of these components requires further analysis and decomposition of the signal using wavelet techniques, which will be discussed in future works. A brief overview of how a combination of the wavelet decomposition technique, cross correlation function and convection velocity can be used to analyze the acoustic and hydrodynamic components of the flow is given in the next section.

4.3.3 Wavelet Decomposition

As detailed in chapter 1, the noise generated by a high speed jet flow is primarily composed of two components - hydrodynamic and acoustic. These two components have different frequencies, propagation speeds and intermittencies. The hydrody-

namic component is intermittent in nature and the acoustic component is continuous, therefore in order to determine this intermittency, spectral analysis in the Fourier space is not sufficient, as it can only determine the frequencies present in a particular signal, but not the time at which it occurs. So, in order to segregate the two components in terms of the frequencies and time of occurrence (i.e., intermittency), a wavelet decompostion technique is more useful. Wavelet decomposition is carried out by the use of continuous wavelet transform (cwt) technique, and is performed by using the 'cwt()' function available in MATLAB (see MATLAB documentation for the definition of cwt() (The MathWorks (2022a)). In short, cwt() works in the same way as a wavelet transform, which takes the projection of a time signal (in this case, wall pressure) over a basis of functions, all derived from a 'mother wavelet', by stretching/ scaling and translation of this mother wavelet in time. The basis of subsequent wavelets, given by $\psi_{a,b}(t)$ is calculated from the mother wavelet as follows -

$$\psi_{a,b}(t) = \frac{1}{\sqrt{a}}\psi\left(\frac{t-b}{a}\right) \tag{4.9}$$

where b is a coefficient which translates the wavelets along the length of the signal, and a is a coefficient which stretches/scales the wavelet. The wavelet transform is then calculated by taking a projection of this basis of wavelets over the required time series, given as follows -

$$\omega_\psi(f)(a,b) = \langle f(t), \psi_{a,b}(t)\rangle \tag{4.10}$$

where $\omega_\psi(f)(a,b)$ represents the wavelet transform coefficients of the time signal $f(t)$ and $\langle\rangle$ represents the dot product of the two series. Thus, using this technique, a scalogram is plotted of the wall pressure signal at a location of $x/D = 10$, $y/D = -2$, $z/D = 0$, i.e. the point at which the jet hits the plate surface, and is given in figure 4.61. The Morse wavelet is chosen as the mother wavelet for performing a continuous

wavelet transform of the input signal. The scalogram is plotted as a function of the

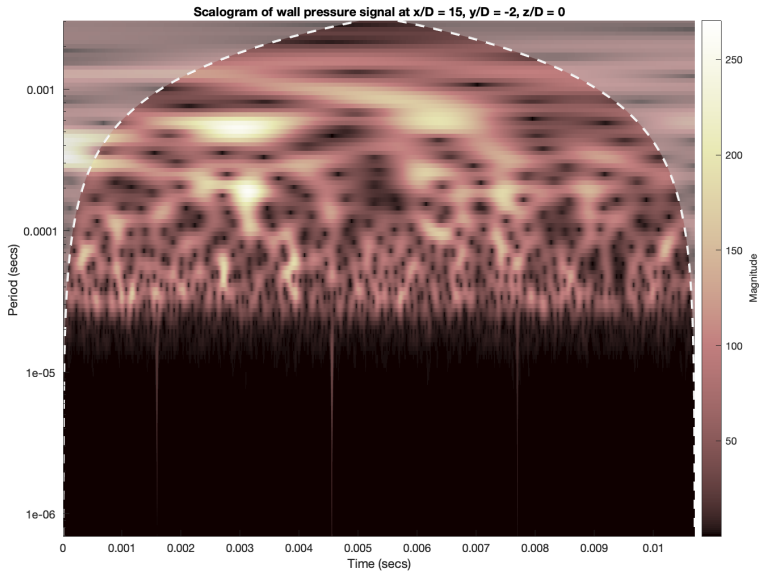

Figure 4.61: Scalogram of Wall Pressure Signal at $x/D = 10$, $y/D = -2$, $z/D = 10$

period of the time signal. Thus, a period less than 0.0001 seconds corresponds to high frequency components in the signal, and a period greater than 0.0001 seconds corresponds to low frequency components of the signal. A high frequency component can be seen at a period of $\sim 10^{-4}$ throughout the time at which the signal is measured. Also, bright spots can be seen at intervals 0.002 - 0.003 seconds and 0.005-0.007 seconds, which can be caused by the intermittent events of jet flow interacting with the pressure probe.

Thus, by using the wavelet transform, the different components of jet flow and the approximate time intervals at which they appear can be identified, and a filtering procedure can be developed, which separates out the wavelet transform coefficients based on a particular threshold. This procedure was developed by Grizzi and Camussi (Grizzi and Camussi (2012)), and the pertinence of this approach to LES data can be tested. It states that the intermittent events in wall pressure data can be

filtered based on a threshold value that is determined iteratively. Briefly, the process states that -

1) The intermittent and continuous components can be extracted based on these wavelet coefficients

2) Cross correlation is calculated between the respective components

3) Convergence criterion for the iterative scheme can be determined by certain other procedures laid down by Grizzi and Cammussi (Grizzi and Camussi (2012)).

The two signals extracted from this process can be further analyzed using more conventional techniques, such as spectral analysis (in Fourier space) to qualitatively interpret the various characteristics of the two components. For further exploiting the advantages of this technique, the time varying flow quantities can be measured along a plane (drawn at the plate surface, instead of extracting wall pressure along a line), and wavelet decomposition can be applied for analyzing the spatial and temporal characteristics of wall pressure. However, a good spatial grid resolution is required for obtaining accurate results from this technique, and it will be used in future studies due to a constraint of time. Also, the wavelet decomposition technique described above has been used and validated by the authors to extract the two components of sound from the signal, but due to a lack of time, it's applicability to the current LES study could not be checked, and will be used for further analysis in the future.

4.4 Installed Jet Case - 37 million Cells

As mentioned in chapter 3, the 15 million cells grid is refined to 37 million cells, and the same physics conditions are applied to this case. However due to the fine mesh size used, the time step to be used for this simulation was estimated as $2 * 10^{-9}$ seconds to obtain a stable CFL number of ~ 0.4, using 280 cores. Using this time step size, it is estimated that 1 flow through time of the simulation would require $\sim$

658 CPU hours, corresponding to 27 days of simulation time. Thus, to simulate 10 flow through times, it would require almost 10 months of pure CPU time and hence due to the time constraints involved with the study, it will be left for investigation in the future.

Chapter 5

CONCLUSION

The compressible jet flow through a converging nozzle is simulated at two conditions - freejet and installed jet to check the applicability of using Large Eddy Simulations in accurately predicting the flow field of a complex jet-plate interaction. The simulation results are compared with the corresponding experiments performed by Mancinelli and Camussi (2018) (in the case of the freejet), and Meloni *et al.* (2019) (in the case of the installed jet) to check the accuracy of simulations and whether a high fidelity LES code can be used for analysing the jet-flow characteristics which cannot be obtained from an experiment. Four cases are considered based on the refinement of the grid - freejet (8 million cells), freejet (22 million cells), installed jet (15 million cells) and installed jet (32 million cells). An unstructured hexahedral mesh is created for each of the cases and LES calculations (with Dynamic Smagorinsky Model) were performed using the code CharLESx.

The freejet case was chosen to develop a basic understanding of compressible jet flow and to validate the simulation set up with experiment results. The freejet case with 8 million cells was simulated for a flow through time of 10, whereas the one with 22 million cells was simulated for a flow through time of 5, due to the time constraints on the work. The flow field was then analyzed in both time and frequency domains to validate the simulation results with the experiment. Hundreds of virtual probes were placed in the flow domain to measure various quantities and develop a quantitative dataset, which can be used for validation and later for more in-depth analysis. Specifically, to validate the results, the mean axial velocity and turbulence intensity were analyzed in the streamwise direction and spanwise directions. Both cases show an en-

couraging correlation with the experiment in the aforementioned quantities, however, as the 22 million cells case was not run for the same duration as the 8 million cells case, it is expected to show better correlation with the experiment due to a higher mesh resolution and consequently lower turbulence intensity, once the simulations are complete. A spectral analysis of the axial velocity was carried out in the Fourier space using Fast Fourier Transforms (FFTs) to estimate the Power Spectral Density at various axial locations, and we observe that the 8 million cells case performs better than the 22 million cells case, primarily because it has been simulated for a longer time and the turbulent flow quantities have been allowed to 'settle'. Qualitatively, from these energy density plots, we observe canonical features that are observed in freejets, and hence with further grid refinement and longer simulation run times, better correlation with the experiment are expected.

In addition to this, the flow characteristics along the nozzle lipline ($r/D = 0.5$) are also calculated to check whether the freejet demonstrates canonical freejet features. The mean velocity, temperature and pressure along the nozzle lipline are calculated to check the mixing performance and development of the shear layer of the jet. A Fast Fourier Transform of the velocity cross correlation at various streamwise points along the nozzle axis are also calculated to check whether the jet follows Kolmogorov's universal $-5/3$ decay law for turbulent energy dissipation at far downstream locations. Both the freejet cases demonstrate this behaviour to a certain degree, further enforcing the point that as the simulations follow canonical jet flow features, with further grid refinement, these LES calculations can be used to substitute experimental analysis in certain situations.

Once the freejet simulations were complete, the installed jet case with 15 million cells was simulated for ~ 10 flow through times, however due to time constraints, the installed jet case with 40 million cells could not be simulated, and will be investigated

in the future. Just like in the freejet, virtual probes were placed at key positions in the flow domain of the installed jet to develop a comprehensive database, which was used to validate simulation results and can be used for further analysis. The flow statistics were analyzed in the time and frequency domains, and a wavelet decomposition based analysis method is also explored. The mean flow velocity along the nozzle axis and the wall pressure on the plate surface (along a line parallel to the nozzle axis) was checked to validate the simulation code with the experiment. It was observed that the mean velocity is slightly under-predicted, whereas the wall pressure was correctly predicted, although it is fluctuating in nature. This is expected because of the coarse resolution of grid used for the simulations, and the wall pressure is expected to show fluctuations because of the way the Dynamic Smagorinsky Model treats near-wall quantities (models them instead of directly calculating them). The jet impact point was correctly estimated by calculating the flatness of wall pressure signals, and development of a turbulent boundary layer is observed from the plot of Coefficient of Pressure (C_P). Spectral analysis of the wall pressure is carried by calculating the Power Spectral Density at various streamwise locations, and we can observe an encouraging correlation with the experiment, and the development of a turbulent boundary layer is also confirmed from these plots at far downstream locations. Further, a wavelet decomposition technique is briefly touched upon, to show the potential of using it as a more comprehensive analysis tool than Fourier analysis, in isolating the sources of sound in the jet flow.

As future investigations, the jet-plate simulation data can be further exploited to study the development of the TBL along the plate surface, and the wavelet decomposition technique can also be explored as mentioned before. However, any such investigations will require very fine grid resolution because of the nature of Large Eddy Simulations, and a significant computing time. Therefore, more refined grid

calculations and further analysis is beyond the scope of the current work, and will be left for future investigations.

To conclude, through these validation studies, it can be ascertained that LES can be used as a tool to complement experimental studies. LES calculations have better spatial resolution as compared to the experiment calculations, but due to the poor temporal resolution, it can take a very long time for a LES calculation to produce accurate, time resolved solutions. Also, the shear amount of time and effort required to create computational grids, run high fidelity 3-dimensional simulations and analyze results is immense, and can defeat the purpose of providing faster, real-world like data. Thus, as is the case with all computer simulations, for now, LES calculations can only be used to complement experimental studies, but not as a substitute.

Chen, T.-J. and S.-S. Chen, "Effects of aircraft noise on hearing and auditory pathway function of school-age children", International Archives of Occupational and Environmental Health **65**, 2, 107–111, URL https://doi.org/10.1007/BF00405728 (1993).

Cohen, S., G. W. Evans, D. S. Krantz and D. Stokols, "Physiological, motivational, and cognitive effects of aircraft noise on children: Moving from the laboratory to the field.", (1980).

Di Marco, A., M. Mancinelli and R. Camussi, "Pressure and velocity measurements of an incompressible moderate Reynolds number jet interacting with a tangential flat plate", Journal of Fluid Mechanics **770**, 247–272 (2015).

Doychak, J., "Department of navy jet noise reduction project overview", "https://apps.dtic.mil/sti/citations/ADA553981" (2010).

Farge, M., "WAVELET TRANSFORMS AND THEIR APPLICATIONS TO TURBULENCE", Annual Review of Fluid Mechanics **24**, 1, 395–458, URL https://doi.org/10.1146/annurev.fl.24.010192.002143 (1992).

Germano, M., U. Piomelli, P. Moin and W. H. Cabot, "A dynamic subgrid-scale eddy viscosity model", Physics of Fluids A: Fluid Dynamics **3**, 7, 1760–1765, URL https://doi.org/10.1063/1.857955 (1991).

Grizzi, S. and R. Camussi, "Wavelet analysis of near-field pressure fluctuations generated by a subsonic jet", Journal of Fluid Mechanics **698**, 93–124 (2012).

Guitton, A., P. Jordan, E. Laurendeau and J. Delville, "Velocity dependence of the near pressure field of subsonic jets: understanding the associated source mechanisms.", in "13th AIAA/CEAS Aeroacoustics Conference (28th AIAA Aeroacoustics Conference)", Aeroacoustics Conferences (American Institute of Aeronautics and Astronautics, 2007), URL https://doi.org/10.2514/6.2007-3661.

Kerhervé, F., A. Guitton, P. Jordan, J. Delville, V. Fortuné, Y. Gervais and C. Tinney, "Identifying the dynamics underlying the large-scale and fine-scale jetnoise similarity spectra", in "14th AIAA/CEAS Aeroacoustics Conference (29th AIAA Aeroacoustics Conference)", Aeroacoustics Conferences (American Institute of Aeronautics and Astronautics, 2008), URL https://doi.org/10.2514/6.2008-3027.

Khalighi, Y., F. Ham, J. Nichols, S. Lele and P. Moin, "Unstructured Large Eddy Simulation for Prediction of Noise Issued from Turbulent Jets in Various Configurations", in "17th AIAA/CEAS Aeroacoustics Conference (32nd AIAA Aeroacoustics Conference)", Aeroacoustics Conferences (American Institute of Aeronautics and Astronautics, 2011), URL https://doi.org/10.2514/6.2011-2886.

Lilly, D. K., "A proposed modification of the Germano subgrid-scale closure method", Physics of Fluids A: Fluid Dynamics **4**, 3, 633–635, URL https://doi.org/10.1063/1.858280 (1992).

Lyrintzis, A. S. and M. Coderoni, "Overview of the use of large-eddy simulations in jet aeroacoustics", AIAA Journal **58**, 4, 1620–1638, URL https://doi.org/10.2514/1.J058498 (2020a).

Lyrintzis, A. S. and M. Coderoni, "Overview of the Use of Large-Eddy Simulations in Jet Aeroacoustics", AIAA Journal **58**, 4, 1620–1638, URL https://doi.org/10.2514/1.J058498 (2020b).

Mancinelli, M. and R. Camussi, "An experimental investigation of the wall pressure field induced by a low and moderate Mach numbers jet on a tangential flat plate", in "2018 AIAA/CEAS Aeroacoustics Conference", AIAA AVIATION Forum (American Institute of Aeronautics and Astronautics, 2018), URL https://doi.org/10.2514/6.2018-3616.

Meloni, S., A. Di Marco, M. Mancinelli and R. Camussi, "Wall-pressure fluctuations induced by a compressible jet flow over a flat plate at different Mach numbers", Experiments in Fluids **60**, 3, 48, URL https://doi.org/10.1007/s00348-019-2696-3 (2019).

Moin, P., K. Squires, W. Cabot and S. Lee, "A dynamic subgrid-scale model for compressible turbulence and scalar transport", Physics of Fluids A: Fluid Dynamics **3**, 11, 2746–2757, URL https://doi.org/10.1063/1.858164 (1991).

Muzet, A., "Environmental noise, sleep and health", Sleep Medicine Reviews **11**, 2, 135–142, URL https://www.sciencedirect.com/science/article/pii/S1087079206001055 (2007).

Park, G. I. and P. Moin, "Numerical aspects and implementation of a two-layer zonal wall model for LES of compressible turbulent flows on unstructured meshes", Journal of Computational Physics **305**, 589–603, URL https://www.sciencedirect.com/science/article/pii/S0021999115007500 (2016).

Pino Martín, M., U. Piomelli and G. V. Candler, "Subgrid-Scale Models for Compressible Large-Eddy Simulations", Theoretical and Computational Fluid Dynamics **13**, 5, 361–376, URL https://doi.org/10.1007/PL00020896 (2000).

RUPPERT-FELSOT, J., M. FARGE and P. PETITJEANS, "Wavelet tools to study intermittency: application to vortex bursting", Journal of Fluid Mechanics **636**, 427–453 (2009).

The MathWorks, I., "Continuous wavelet transform (cwt)", "https://www.mathworks.com/help/wavelet/ref/cwt.html" (2022a).

The MathWorks, I., "Cross correlation (xcorr)", "https://www.mathworks.com/help/wavelet/ref/cwt.html" (2022b).

TINNEY, C. E. and P. JORDAN, "The near pressure field of co-axial subsonic jets", Journal of Fluid Mechanics **611**, 175–204, URL https://www.cambridge.org/core/article/near-pressure-field-of-coaxial-subsonic-jets/A59AA7318312F48A4AC2282E29335D6C (2008).

Toro, E. F., M. Spruce and W. Speares, "Restoration of the contact surface in the HLL-Riemann solver", Shock Waves **4**, 1, 25–34, URL https://doi.org/10.1007/BF01414629 (1994).

Wall, A. T., K. L. Gee, P. J. Morris, T. Colonius and K. T. Lowe, "Introduction to the special issue on supersonic jet noise", The Journal of the Acoustical Society of America **151**, 2, 806–816, URL https://doi.org/10.1121/10.0009321 (2022).